PHYSICAL MODELING OF FILAMENT GROWTH AND RESISTIVE SWITCHING IN METAL OXIDE-BASED RRAM

By

Kena Zhang

DISSERTATION

Submitted in partial fulfillment of the requirements
for the Degree of Doctor of Philosophy
in Materials Science and Engineering at
The University of Texas at Arlington
December 2022

Arlington, Texas

Committee Chair: Dr. Choong-Un Kim

Committee Members:

Dr. Ye Cao, Supervising Professor

Dr. Yaowu Hao

Dr. Erika La Plante

Dr. Panchapakesan Ganesh

ACKNOWLEDGEMENT

For the past four years at UTA, I have greatly enjoyed my time as a graduate student, and I could go through the challenges and enjoy my work thanks to many smart and nice people who helped me to finish this program possible.

First and foremost, I wish to express my sincere gratitude to my supervisor Prof. Ye Cao for his utmost support, comments, and prompt responses to any queries that I made. I have learned so much from his guidance. I sincerely thank him for providing plentiful resources and a lot of freedom for my research. In such an optimal environment, I am able to work and learn without barriers.

I would also like to Dr. P. Ganesh, group leader of Nanomaterials Theory Institute at the Center for Nanophase Materials Sciences Division at Oak Ridge National Laboratory, for his professional guidance during my research. We had extensive discussions and I have learned a lot of knowledge and skills about Molecular Dynamics Modeling. I also want to thank Dr. Jianjun Wang at the Pennsylvania State University, Dr. Yuhui Huang at Zhejiang University, and Mr. Abhijeet Dhakane from Dr. Ganesh's group for their help with the model building.

I would also like to thank my group seniors, Dr. Yao Ren and Mr. Ryan Hart. They taught me a lot of technical skills and coding skills. I also want to thank my current groupmates, Mr. Bharat Pant and Dr. Yi-de Liou. I enjoy working and discussing with them and thanks for being around.

I also thank my thesis committee members, Dr. Choong-Un Kim, Dr. Yaowu Hao, Dr. Erika La Plante for being very encouraging throughout this journey. Their comments and advice were extremely helpful to proceed with my study.

Finally, thanks to my family and friends for their unconditional support and love. I love You.

ABSTRACT

Metal oxide-based resistive random-access memories (RRAM) exhibit several excellent performances, such as nanosecond switching speed, large write-erase endurance, and long retention time, and can potentially replace the traditional circuit elements for use as the fundamental units in next-generation hardware deep-learning or neuromorphic systems. The functionality of a metal oxide-based RRAM is attributed to an oxygen vacancy ($V_{\ddot{O}}$)-rich conductive filament (CF), which initially forms, and later dissolves or regrows inside the oxide layer during the resistive switching process. However, the complicated interplays among the coexisting chemical, electrical, mechanical, and thermal effects during the formation, growth, and rupture of the CFs make the dynamic of the resistive switching behavior extremely complicated and unpredictable, and its underlying mechanisms are not fully understood. Here, we developed a phase-field model based on defect chemistry, charge transport dynamics, and micro elasticity theory to investigate the electroforming process and subsequent resistive switching behavior, using HfO_{2-x} as a prototypical model system. It is revealed that the CF formation is assisted by the supply of oxygen vacancies $V_{\ddot{O}}$ at the anode/oxide interface and the $V_{\ddot{O}}$ transport in the bulk during the electroforming process. The CFs with more uniform morphology can be obtained by employing active electrodes with low vacancy formation barrier E_b and metal oxide with large electrical conductivity and lower thermal conductivity.

We also explored the role of the elastic effect on resistive switching behavior. It is found that the local oxygen vacancy distribution induces a local Vegard strain and a strain gradient, which acts as an additional driving force that inhibits the oxygen vacancy

migration during switching and reduces the current on/off ratios. In addition, high-throughput phase-field simulations and a machine learning approach are performed to derive interpretable analytical correlations between the material properties (electrical and thermal conductivities, Vegard strain coefficients of the metal oxides) and the device performances (current on/off ratio and switching time). It is revealed that optimal resistive performance can be achieved in materials with a small Lorenz number and Vegard strain coefficient.

Furthermore, we also found that the switching performances can be enhanced by microstructure design. Due to the electric field concentration effect, embedding metal NIs leads to a more deterministic formation of the CF from their vicinity, in contrast to the random growth of CFs without embedded NIs. This deterministic vacancy nucleation further reduces the forming, reset, and set voltages, and enhances the uniformity of these operation voltages and current ON/OFF ratios. We further demonstrate that increasing the height of NIs, modifying the metal NIs to a triangle shape, and choosing active NI metals with high oxygen affinity can further optimize the switching performance. Our work provides a deep understanding of the underlying mechanism of CF growth and rupture, as well as the designing strategy for materials selection and microstructure design for further improved RRAM performances.

TABLE OF CONTENTS

LIST OF FIGURES

LIST OF TABLES

Chapter 1. Introduction

1.1. Motivation

The rapid growth of information technology, especially the Artificial Intelligence (AI) requires huge data storage and fast processing units. Computing efficiency depends on increasing the number of transistors in a dense integrated circuit (IC) microchip which almost doubles about every two years [1,2], based on Moore's law. This is typically realized by shrinking the transistor size to nanoscale. However, the reduction in device size is accompanied by high-power consumption, increasing power cost and other physical constraints, which limits the further miniaturization of transistors. On the other hand, the current computation system is based on von Neumann computing architecture, in which the storage and computation units are separated. During the computing process, the data is transferred from the memory unit to the process unit. The existing wall between the memory unit and the processing unit limits the efficiency of computation, known as the "memory wall" [2]. These two limitations impede the improvement of the performance of the current memories and processors. Thus, it is urgent to develop new devices to meet the requirements for data and information storage and processing.

In-memory computing (IMC) is a novel approach to overcome these limitations by computing *in situ* where the data is stored[2]. The working principle of IMC is similar to the synapses in the human brain, where there exists no physical gap between memory and computation. Memristor (i.e., memory + resistor) provides an opportunity to integrate the memory and processor units together, therefore can void the memory wall, and go beyond

the von Neumann architecture to realize the calculation *in situ*. Typically, the memristor has a simple two-terminal structure with three layers - an insulating layer acting as a storage layer, sandwiched by a top (TE) and a bottom electrode (BE). Initially, a conduction channel is created by soft breakdown or formed by the active electrode oxidation during one-time electroforming process[3-5]. Then, the electrically conductive filaments (CFs) can be formed inside the oxide layer to connect top and bottom electrodes resulting in a low resistance state (LRS) and ruptured to switch the device to a high resistance state (HRS), under the applied voltages. Therefore, the insulating layer can be dynamically reconfigured when stimulated by electrical inputs and shows different resistance states[6,7]. Unlike conventional memories, memristors (in the term of resistive switching random access memory, RRAM) with fast switching speed, small programming current[8], controllable resistance states[9,10], *etc*. are considered as promising candidates for next generation nonvolatile memory [11,12], in-memory computing, and neural networks[13-18].

Although memristors show potential applications in the next generation nonvolatile memory and in-memory computing systems, there still exist challenges to be solved. One of the key challenges is the large variations in the set and reset voltages, HRS, LRS, *etc*. from cycle-to-cycle or device-to-device or both, which is determined by the microstructure, composition, shape, and position, *etc*. of the CF in the switching layer during the switching processes. Recently, the physical reconfigurations of the CFs have been experimentally captured by direct imaging methods such as TEM[19-22] and conductive AFM (c-AFM)[23-25], however, the key factors that influence the CF formation and rupture and eventually determine the performance of RRAMs are still not well understood. The coupling effect among the chemical, thermal, electrical, and mechanical effects makes the electroforming

and resistive switching (RS) process extremely complicated and unpredictable. Experimentally it is extremely difficult to untangle these coupling effects, which limits the design of RS devices of predictable behaviors. Secondly, various material systems have been investigated to be potentially used as the switching layer in memristors in the past few decades. However, there still lacks a clear consensus on what are the ideal materials that lead to a better performance of metal oxide-based RRAM. Finally, the microstructure of the switching layer also has a significant impact on the kinetics of the formation/dissolution/reconnection of the CFs during resistive switching, which should be studied comprehensively for a better understanding of the device performances. Compared to experimental studies, theoretical models and computational simulations provide a unique capability to investigate multi-physics and identify the key factors that influence RS behavior. The preciseness and efficiency of theoretical prediction and numerical modeling enables a fundamental understanding of the mechanism of resistive switching, and is able to generate a high-throughput database and rules for materials selection and microstructure design for better RS performances.

1.2. Research objectives and plans

The primary goal of this research is to investigate the conductive filament growth and resistive switching behavior in metal oxide-based RRAM by developing a comprehensive physical model integrating the electrochemical reaction, mass diffusion, thermal transport, electrical conduction, and mechanical stress relaxation dynamics. This investigation could offer tactics to address the challenges as mentioned in Section 1.1, and further improve the performance of RRAM. Based on the above objectives, we will carry out the following studies,

1. Develop a model to simulate the conductive filament growth behavior during the electroforming process in the metal oxide-based RRAM.
    a. Explore the mechanism of conductive filament growth behavior.
    b. Study the effects of electrode and oxide switching layer properties on the filament growth behavior including the current-voltage characteristic, conductive filament morphology, and conductive filament growth direction.
2. Simulate the resistive switching behavior in the metal oxide-based RRAM.
    a. Study the mechanism of resistive switching.
    b. Incorporate the impact of mechanical strain induced by oxygen vacancy on resistive switching behavior and its interaction with mass diffusion, thermal transport, and electrical conduction dynamics in metal oxide-based RRAM.
    c. Perform high throughput calculations and employ machine learning to identify key materials parameters and their correlations to the RS switching characteristics and performance of RRAM.

3. Elucidate the effect of inhomogeneous metal oxide microstructure on the performance of RRAM device.
    a. Investigate the conductive filament formation and resistive switching behavior in HfO_2 films embedded with ordered metal nano-island arrays.
    b. Explore the effects height, geometry, and materials type of embedded nano-island on the resistive switching performance.

Chapter 2. Background

2.1. The Fundamentals of memristor

It's well known that capacitor (C), resistor (R), and inductor (L) are three basic passive circuit elements. However, Prof. Leon Chua[26] has predicted that there should be a fourth fundamental element based on the symmetry arguments of the four circuit variables: charge (q), voltage (V), current (i), and magnetic flux (φ), which is called memristor (memory + resistor). As Fig. 2.1 shows, Chua indicated that there exist six different mathematic relations between these four variables where $dq = idt$ is the definition of current, $d\varphi = vdt$ is based on Faraday's law for inductance, and the remaining four relations correspond to four basic circuit elements. The relationship between the magnetic flux (φ) and the electric charge (q) can be described as the fourth basic circuit element memristor M, $d\varphi = Mdq$, of which the dimension is identical to resistor[27]. This equation reveals that the resistance of the memristor is dependent on the charge changes under voltage.

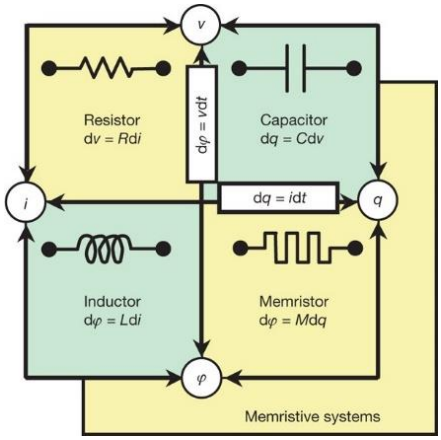

Fig. 2.1 Four basic two terminal circuit elements[27].

However, in the past few decades, since the concept was introduced, the memristor had not been realized due to the limitation of materials and technology at that time. Both industry and academia have been working on this unique electronic element. Until 2008, the Hewlett-Packard group first obtained a realistic and visible memristor device by using a Pt/TiO_2/Pt sandwich structure and realize the resistive switching behavior, as shown in Fig. 2.2. The TiO_2 film consists of a doped region with a high concentration of positive ions showing low resistance R_{on} and undoped region having high resistance R_{off}. The memristor function can be achieved by the movement of the boundary between two regions causing resistance change continuously when an external voltage is applied on the electrode, as shown in Fig. 2.3. This remarkable result inspires a new research wave.

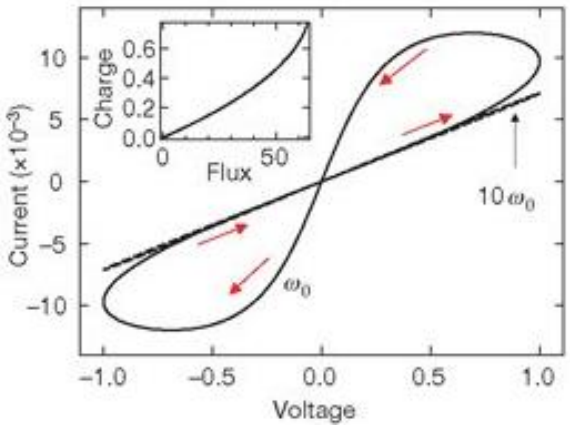

Fig. 2.2 The I-V characteristic of Pt/TiO_2/Pt structure[27].

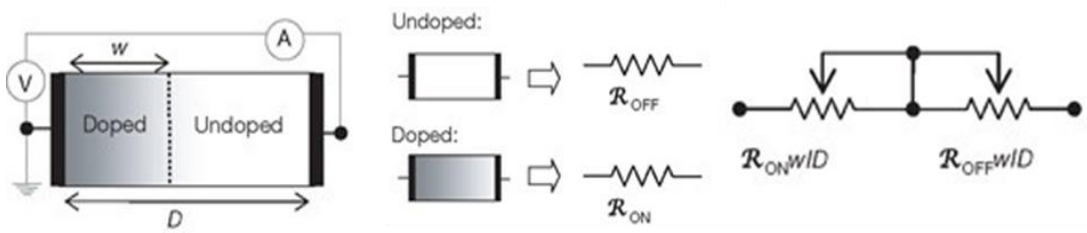

Fig. 2.3 The equivalent circuit diagram, V, voltmeter; A, ammeter[27].

2.1.1. Resistive switching materials

The resistive switching behavior has been observed both in inorganic and organic systems. Organic materials such as polymers (PVP[28], PMMA[29], *etc*.), and biological materials like egg albumen[30], polysaccharide[31], ploypeptide[32], *etc*. can display resistive switching behavior. The uniformity and stability of the device fabricated with organic materials are far from the inorganic device due to the thermal instability of organic materials. It is still a long way to employ organic materials as the switching layer for the next generation memory. Several inorganic materials have demonstrated the resistive switching phenomenon including metal oxides, nitrides, and chalcogenides. Among these materials, metal oxide-based RRAMs, including HfO_x[33], TiO_x[34], ZrO_x[35], TaO_x[36], NiO_x[37], VO_x[38], Cu_xO[39], NbO_x[40], and perovskites $SrTiO_3$[41] *etc*., have been extensively studied. However, a key question is what type of metal oxide is the ideal candidate as a switching layer for RS devices. While various metal oxide material systems have been investigated, there still lacks a general design principle for materials selection.

In addition to the switching layer, the electrode material properties also have a great influence on the switching behavior in RRAM. A wide range of materials has been used as electrodes including metal, metal oxides, and some nitrides. The most common electrode materials are metals such as Ag[42-44], W[45], Pt[34,46], Ti[39], *etc*., and nitride-based compounds TiN[47] and TaN[48] are usually used as the electrode. Some oxide-based electrodes are also reported rarely including AZO[49], FTO[50], and ITO[51]. Different electrode materials may lead to different electrical behaviors. Therefore, investigating the effect of electrode properties on RS behavior and selecting a suitable material system are key to the highly useful and stable memristor devices.

2.1.2. Resistive switching type

The memristor usually has a very simple structure with electrode-insulator-electrode stacking, as shown in Fig. 2.4. Most as-prepared RRAM must undergo an initial process called “electroforming” before first switching operation since RRAM is usually fabricated with insulator[52-55]. Generally, a higher-than-usual voltage is employed on the device to enable the formation of a conductive filament as a controlled soft breakdown and the voltage at this process is called forming voltage V_f. After the electroforming process, the RRAM cell is subject to reversible switching between HRS and LRS repeatedly by reset (LRS to HRS) and set (HRS to LRS) operations under voltage. Two main coexisting electric field and temperature based on Joule heating are induced by the external electric bias. Their relative importance varies depending on the material systems leading to two classic resistive switching modes with different I-V curves: unipolar and bipolar switching[9,56]. In the unipolar resistance, the resistive switching is independent of the polarity of the voltage stimulus, i.e., the set and reset voltages have the same polarity, as shown in Fig. 2.5. A voltage with opposite polarity is used to set and reset the device which is well known as the bipolar RRAM. These different switching types depend on the contribution of the electrical field and Joule heating which almost appears simultaneously in all RRAM. Generally, if the device is mainly dominated by the role of thermal effect based on the Joule heating, it shows nonpolar switching where the CF formation and rupture are mainly caused by thermal diffusion whether on positive or negative voltage. The device tends to be bipolar switching if the electrical field plays a significant role where the growth and rupture of CF are controlled by the electric field[8].

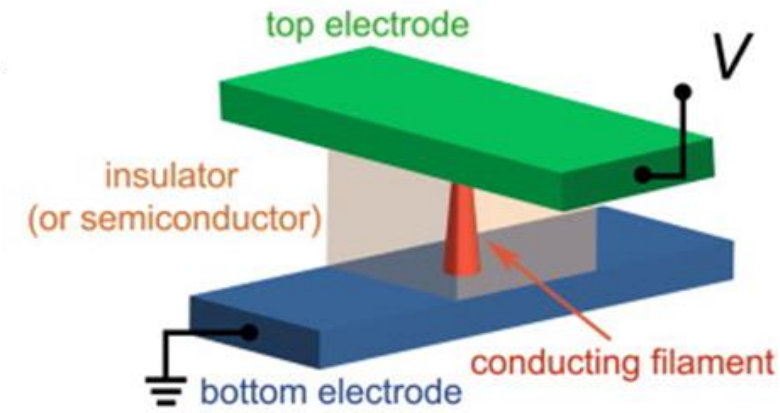

Fig. 2.4 Schematic of conductor/insulator /conductor sandwich structure[56].

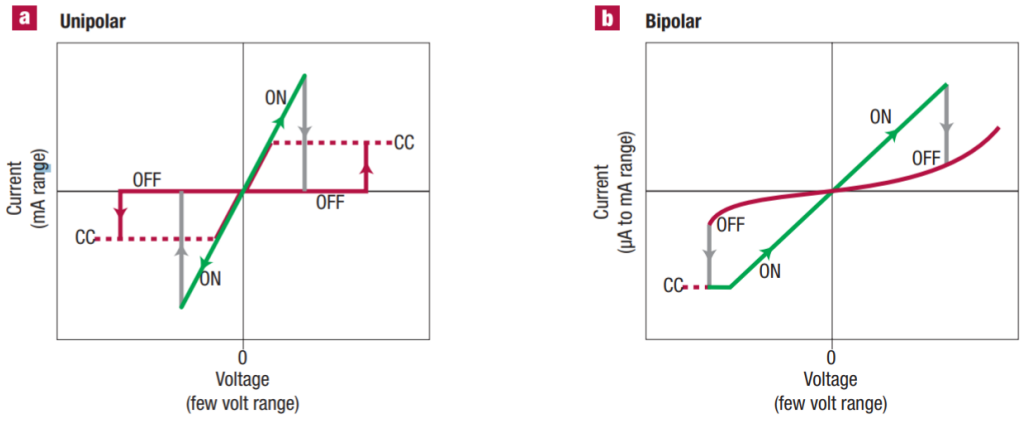

Fig. 2.5 Schematic *I–V* characteristics of (a) unipolar and (b) bipolar switching. The compliance current I_{cc} is employed during the electroforming or set process to prevent permanent breakdown[9].

2.1.3. Resistive switching mechanism

Due to the wide variety of material systems corresponding to the different switching mechanisms, studying the mechanisms helps to develop a reliable memristor and optimize the performance of device. Generally, the mechanism can be divided into CF controlled or electron trapping/de-trapping controlled. The CF is referred to as a conduction channel

with tens or hundreds of nanometers in diameter. The CF controlled RRAMs can be classified into (a) electrochemical metallization devices (ECM) where the metal ions formed in CF are from the electrochemical active electrode such as Ag[57,58], (b) valance change memory devices (VCM) where the CF is composed of intrinsic defects such as oxygen vacancies[59-63].

The ECM device is also referred to as metal ion-based RRAM consists of an active top electrode such as Ag and a relatively inert bottom electrode like W and Pt[43]. The mechanism is usually explained by the migration of metal ions and subsequent redox reaction of the active metal at the top electrode, which leads to the formation and breakage of metal conductive filaments and ultimately regulates the resistive switching behavior. The switching mechanism can be well understood in some systems by TEM observation, such as the Ag/a-Si/W device reported by Yang *et al*.[43] as shown in Fig. 2.6. During the set process, a positive voltage is applied on the active top electrode Ag which forces the oxidation of Ag atoms to Ag^+ cations ($Ag \rightarrow Ag^+ + e^-$). The Ag^+ migrates across the Si layer to the bottom inert W electrode under a high electrical field. Then a reduction reaction ($Ag^+ + e^- \rightarrow Ag$) occurs at the W electrode which allows the Ag atoms to accumulate at the cathode and extend to the Ag electrode until the CF is formed. The device switches to LRS (ON) state. The Ag CF dissolves and the device switches to HRS (OFF) state by the application of voltage with opposite polarity. This mechanism is observed in many ECM devices[42,43,57,58].

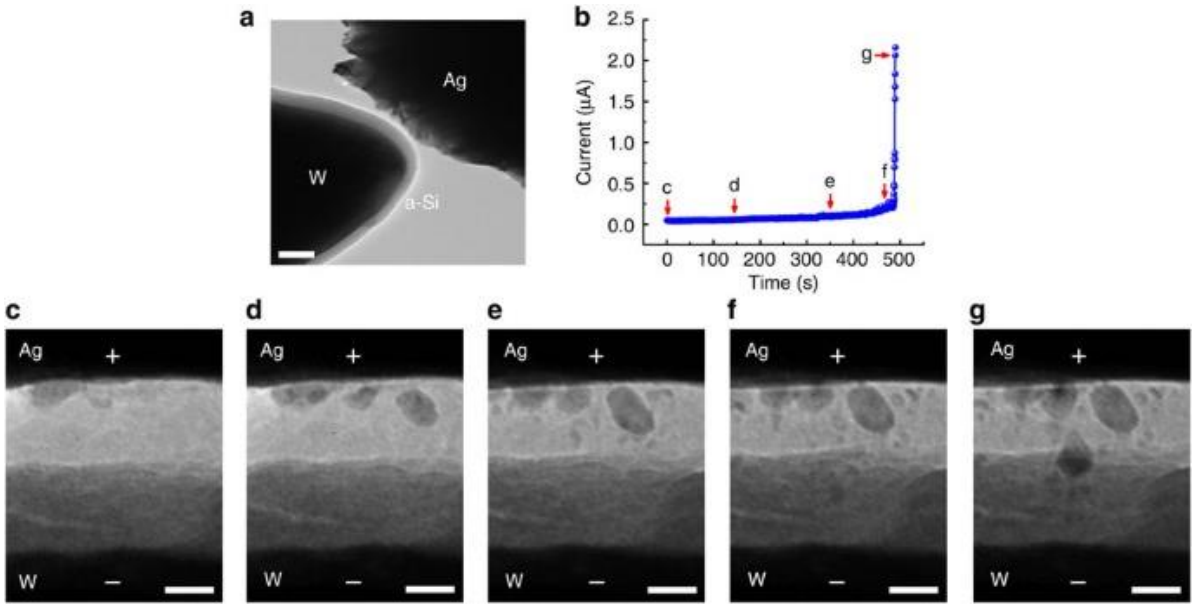

Fig. 2.6 *In-situ* TEM observation of conducting filament growth in vertical Ag/a-Si/W memories[43].

For VCM devices, resistive switching depends on the generation of oxygen vacancy ($V_{\ddot{O}}$) and the redistribution of the $V_{\ddot{O}}$. This mechanism generally displays in the metal oxide (e.g., TiO_2, Ta_2O_5, HfO_2) switching layer. Initially, the oxygen is distracted out of the lattice to the anode and left $V_{\ddot{O}}$ in the oxide layer under the high electrical field. The accumulation of the $V_{\ddot{O}}$ in the oxide layer forms the CF connected between electrodes enabling the resistance switches to a low state. Afterward, when a voltage with the same or opposite polarity is applied, the CF is disconnected with a gap between electrodes based on the $V_{\ddot{O}}$ migration under voltage and Joule heating. As the CF connected and disconnected, the resistance of the device can switch back and forth between HRS and LRS. Li *et al.*[64] directly traced the oxygen vacancies generation and the formed CF under voltage in HfO_2 based RRAM cell based on low-loss energy-filtered images by using *in situ* TEM

and then proposed that the switching behavior stems from the formation and rupture of CF consisted of $V_{\ddot{O}}$, as shown in Fig. 2.7.

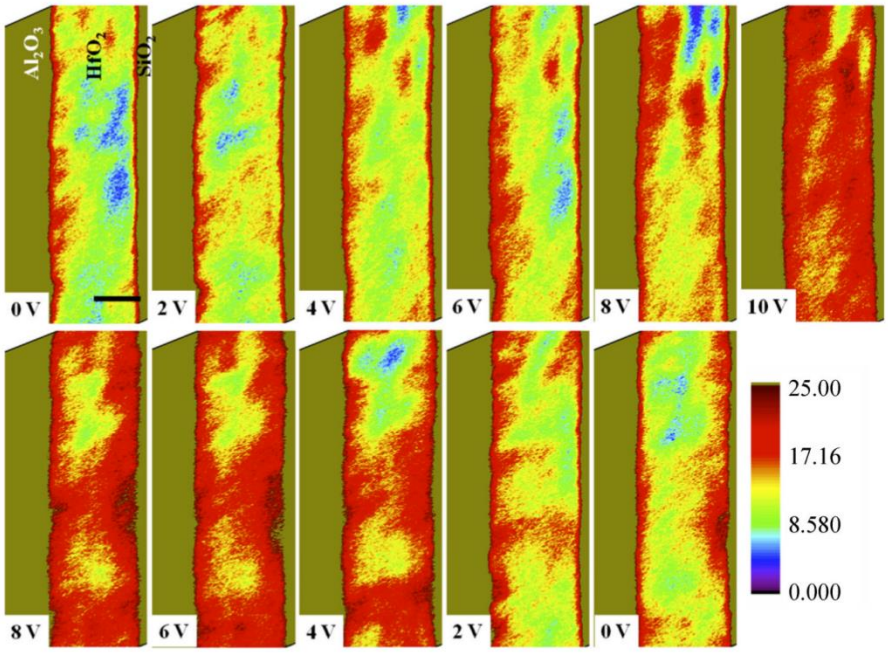

Fig. 2.7 Low-loss energy-filtered images illustrating the concentration of the oxygen vacancies increases with the increasing positive bias. Red encodes higher concentration of the oxygen vacancies[64].

Both ECM and VCM devices are chemical switches because the chemical reaction is involved to form the CF. There is also a resistive switching depending on the physical changes where the resistance change is contributed from the electrons trapping and de-trapping. This mechanism is explained by the fact that the electrons injected from the electrode can be trapped/de-trapped in the charge traps near the electrode/insulator interface[65] or inside a disordered thin film[66], thereby modulating the resistance of the device. Ding *et al.*[67] verified the formation and breakage of the conduction path in Al/PVP:Ti_3C_2/ITO device based on the electron trapping/de-trapping by using conductive

atomic force microscopy (C-AFM) and Kelvin probe force microscopy (KPFM), as shown in Fig. 2.8. They found that the surface potential is enhanced after applying a positive voltage. It is demonstrated that the electrons are trapped under an electrical field that crosses the film and forms the conduction path. The trapped electrons are released with the negative bias that allows the rupture of the conduction path. Compared with ECM and VCM, the performance of the device based on the electrons trapping assisted conduction mechanism is more controllable and uniform since the chemical reaction and ion migration progress are not involved. However, the trapped electrons can easily escape leading to problems in terms of the stability and durability of the device.

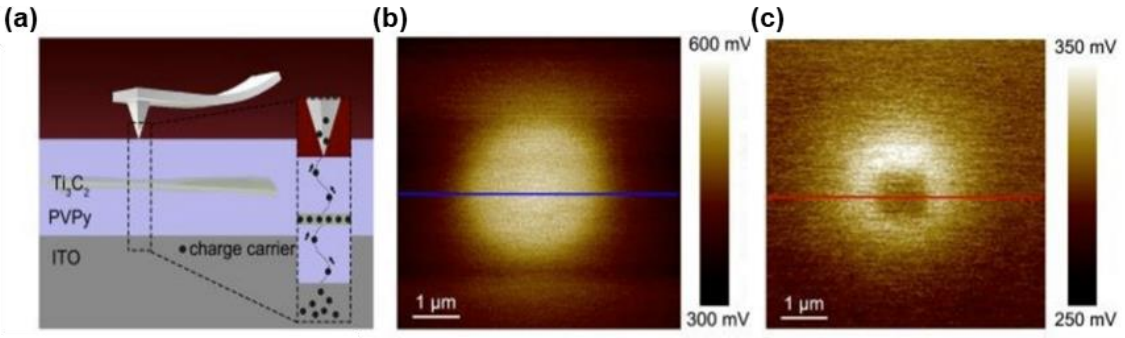

Fig. 2.8 a. The illustration of charge trapped, and conductive path formed between AFM tip and BE. b. KPFM surface potential under a bias of +5 V c. KPFM surface potential under a bias of + 5 V followed by a negative voltage -8V[67].

2.2. Direct visualization of the resistive switching behavior

Since the memristor device has been successfully fabricated in 2008 by HP, there has been an explosion of systems displaying the resistive switching effect. Researchers have extensively studied the performance of memristors. Some groups use high-resolution transmission electron microscopy (HRTEM) to directly observe the conductive filament nature during resistive switching[21,42,43,68,69]. Kwon *et al*.[69] fabricated a pristine TiO_2 thin film with a brookite structure connected with a platinum electrode. After the set process, a CF shows a conical pillar with almost 10 nm width with a non-stoichiometric Ti_nO_{2n-1} phase that can be identified by the TEM diffraction pattern. Then the CF disappears after the RESET transition. Their work not only provides strong experimental evidence that the CF forms and ruptures during switching, but also indicates the difficulty in imaging the nature of conductive filament such as the TEM image can be only identified in a very thin lamella and then causes the low probability of capturing the nano conductive filaments. As shown in Fig. 2.9, Chen *et al*.[21] also used HRTEM to identify the conductive filament growth. Another dedicated tomography technique by using conductive atomic force microscopy (C-AFM) has been also developed to characterize the CF[24,25,70]. Umberto *et al*.[70] used C-AFM with a conductive probe attached to a cantilever to remove materials layer by layer and then measure the local current to obtain the shape and size of the CF, as shown in Fig. 2.10. Although many high-tech analytical instruments and approaches have been employed by research groups, the progress in the characterization of CF properties is slow due to the dimensions, the stochastic nature, and the complex dynamic evolution of the CF during the resistive switching.

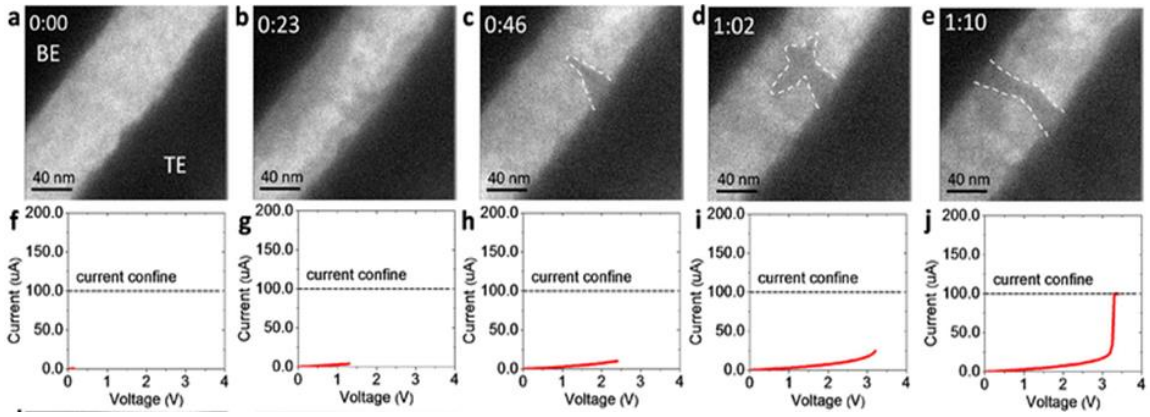

Fig. 2.9 *In situ* TEM images and the corresponding *I–V* curves with applied voltage, CF produced near the top electrode[21].

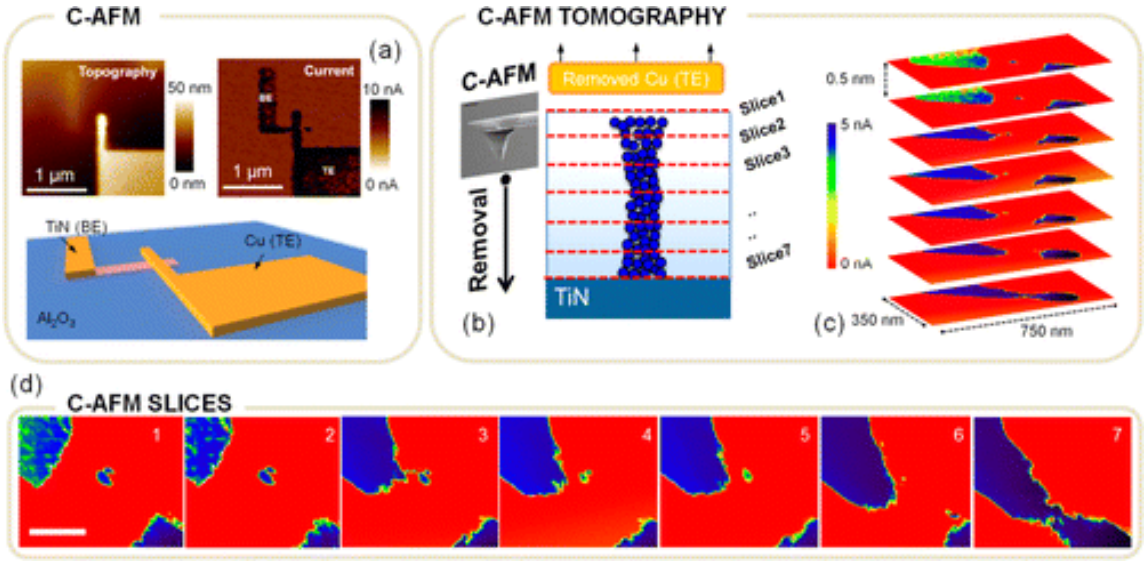

Fig. 2.10 a. Planar 2D C-AFM performed memory cell in SET-state. b. Schematic of the C-AFM tomography procedure, the diamond tip is exploited to collect several slices at different heights of the CF. c. the collected 2D C-AFM slices. d. Collection of 2D slices constituting the data set for the 3D interpolation. The highly conductive features on the top-left and bottom-right corners means CF appears in the middle of the active area[70].

2.3. Modeling of the resistive switching behavior

As mentioned, the complex dynamic during resistive switching is difficult to explore by direct imaging. Modeling approaches are emerging as powerful tools to investigate the physical dynamics during resistive switching, which play critical roles in fully understanding the mechanism and contribute to advancing the performance of RRAM. For example, many researches focuses on calculating the formation and migration energy barriers in various oxide switching layers such as Al_2O_3[71], TiO_2[72], HfO_2[73], and Ta_2O_5[74,75], and the formation/broken of metallic CFs in Cu/SiO_2 cells[76,77] by using atomic-scale simulations including density functional theory (DFT) and molecular dynamics (MD). However, the spatial and temporal scales of atomistic modeling limit the deep understanding the physic phenomenon which are not typically accessible in experiments. Compared with atomic-scale modeling, mesoscale modeling has been developed to quantitatively describe the CF dynamic and resistive switching behaviors in memory devices[78-82]. There are several standing mesoscale models for the dynamic of filament evolution as follows:

Filament gap model

This model is developed to identify the filament gap characteristic. One of the most popular models based on filament gap is proposed by Guan *et al*.[83,84]. They selected the filament gap size between the tip of the filament and the opposite electrode as the state variable to describe the resistive switching, as shown in Fig. 2.11. The filament growth and rupture inside the insulator are dependent on the movement of oxygen vacancies.

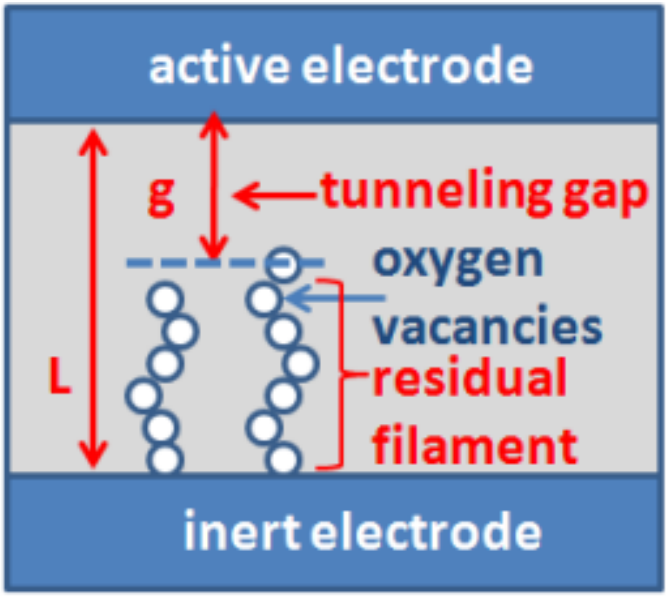

Fig. 2.11 Schematic of conductive filament with gap distance g[84].

The change of filament gap rate is determined by[83],

$$\frac{dg}{dt} = V_0 \cdot exp(\frac{-E_{a(m)}}{k_b T}) \cdot sinh(\frac{q a_h \gamma V}{L k_b T}) \quad (2\text{-}1)$$

where V_0 is attempt-to-escape frequency, $E_{a(m)}$is the activation energy barrier for oxygen vacancy generation in the set process or migration energy barrier in the reset process, k_b is the Boltzmann constant, T is the temperature, q is the elementary unit charge, a_h is the hopping distance, γ is the electrical field enhancement factor, V is the applied voltage, L is the thickness of the switching cell. The change of filament gap is strongly dependent on the temperature, they also consider the temperature T effect by the following equation[83],

$$c_p \frac{dT}{dt} = V(t)I(t) - k(T - T_{bath}) \quad (2\text{-}2)$$

where c_p is the heat capacitance, $V(t)I(t)$ is the Joule heating, T is the effective temperature in the conductive filament domain, T_{bath} is the ambient temperature, k is the thermal conductivity. Then the current flowing through the switch cell based on the gap distance and the field strength is defined as[83],

$$I(g, v) = I_0 \cdot exp(\frac{-g}{g_0}) \cdot sinh(\frac{V}{V_0}) \tag{2-3}$$

where I_0, g_0 and V_0 are the fitting parameters to match the experimental results. The significance of their model is they can simulate the variabilities of the RRAM by introducing a Gaussian random number δg which is a function of the temperature[83],

$$\delta g(T) = \frac{\delta_g^0}{\left\{1+exp\left[\frac{(T_{crit}-T)}{T_{smith}}\right]\right\}} \tag{2-4}$$

where δ_g^0 and T_{smith} are the fitting coefficients, T_{crit} is a threshold temperature where a significant variation occurs. This simulation model of the impact of RRAM variability can be employed to describe the accuracy of the neuromorphic visual system[84]. However, the main limitation of this model is oxygen vacancies diffusion is not considered.

Filament dissolution model

This model is proposed by Russo *et al.*[85-87] based on the thermally enhanced dissolution of CF in unipolar RRAM. When the CF is created, the memristor displays a low resistance state. Under a reset voltage, the temperature is enhanced inside the CF region and up to the critical value T_{crit}. Consequently, the CF dissolution occurs, and the device turns on a high resistance state, as shown in Fig. 2.12.

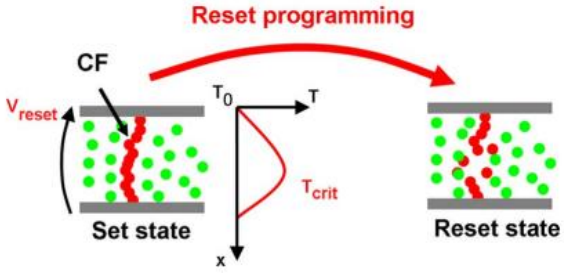

Fig. 2.12 Schematic representation of the reset operation. When the reset voltage is applied to the CF, the inner temperature is raised by Joule heating, and CF rupture occurs[85].

Two simple partial equations are employed to simulate the current and temperature. The electrical potential V is calculated by the following equation[85],

$$\nabla \cdot (\frac{1}{\rho} \nabla V) = 0 \tag{2-5}$$

where ρ is the resistivity of the materials where $\rho = \rho_{CF}$ inside the CF region and $\rho = \rho_{ox} \gg \rho_{CF}$ in the remaining oxide region. The generated heat based on Joule heating is described as[85],

$$-\nabla \cdot (k \nabla T) = \rho J^2 \tag{2-6}$$

where k is the thermal conductivity, T is the temperature, $J = \nabla V / \rho$ is the current density calculated by Ohm's law. The calculated temperature promotes the diffusions of defects outward CF or reaction with oxide region. As a result, the CF is broken. The dissolution of CF is simply described by the velocity of CF boundary v_D[85],

$$v_D = v_{D0} e^{-\frac{E_a}{k_B T}} \tag{2-7}$$

where E_a is the activation energy, k_B is the Boltzmann constant. This theoretical model is very simple but can be only used to simulate the unipolar RRAM which is controlled by the Joule heating effect.

Electrons tunneling model

This physical model is developed by Abbaspour *et al*.[88] and is usually employed to simulate the electroforming and resistive switching process in metal oxide-based RRAM[53,89]. In their model, the current through the device is associated with electron tunneling. The current through the electrode is determined by the electrons tunneling probabilities $TP(E)$ which are given by the Wentzel-Kramers-Brillouin (WKB) approximation[88],

$$TP(E) = e^{-2\int_{x0}^{x1} dx \frac{1}{\hbar}\sqrt{2m^*(V-E)}} \tag{2-8}$$

where $x0, x1$ are the initial and final tunneling positions, m^* is the effective electron mass of metal oxide, V and E are the tunneling barrier and particle energy, respectively.

In most metal oxide-based RRAM, the oxygen vacancies inside the CF are referred to as traps where the electrons jump through them. The electron traps result in a leakage current through the switching layer, and then the device turns to the low resistance state. The hopping rate of the electrons from mth trap to nth trap is determined by using Miller-Abraham's formula[88],

$$h_{nm} = \begin{cases} v_{0n} exp\left[-\frac{d_{nm}}{a_0} + \frac{q(V_n^H - V_m^H)}{k_B T}\right] & V_n^H \le V_m^H \\ v_{0n} exp\left[-\frac{d_{nm}}{a_0}\right] & V_n^H > V_m^H \end{cases} \tag{2-9}$$

here, h_{nm} is the hopping rate of electrons from the mth trap to nth, d_{nm} is the hopping distance between trap n and m, V_n^H and V_m^H are the potentials at the trap n and m, v_{0n} is the vibrational frequency of the electrons, a_0 is the attenuation length of the wave function of the electrons. The trap-assisted tunneling (TAT) current is then calculated by[88],

$$I_{TAT} = e\sum_{n=1}^{N}[p_n H_{na} - (1-p_n)H_{an}] \tag{2-10}$$

where e is the electron charge, N is the total number of the traps, $p_n \in [0,1]$ is the occupation probability of the nth trap, H_{na} and H_{an} are the hopping rates from the nth trap to the electrode and vice versa, which are given by[88],

$$\begin{cases} H_{na} = H_0 N^{T,B}(E_n^+) F_{in}^{T,B}(E_n^+) TP(E) \\ H_{an} = H_0 N^{T,B}(E_n^-) F_{out}^{T,B}(E_n^-) TP(E) \end{cases} \tag{2-11}$$

where $H_0 N^{T,B}(E_n^{+,-})$ is the coupling factor between metal oxide and electrode, H_0 is the fitting parameter, $N^{T,B}(E_n^{+,-})$ is the number of states within the electrodes at a given energy, $F_{in,out}^{T,B}(E_n^{+,-})$ is the Fermi integral. The occupation probability p_n can be calculated by the current continuity equation[88],

$$(1-p_n)\sum_{m=1,m\neq n}^{N} p_m h_{mn} - p_n \sum_{m=1,m\neq n}^{N} (1-p_{m)} h_{nm}$$

$$+(H_{ca}+H_{na})(1-p_n) - (H_{ca}+H_{na})p_n = 0 \tag{2-12}$$

This model has been validated in HfO_2 based RRAM. It can catch the electrons dynamic in the metal oxide-based system.

Electro-thermal model

Ielmini *et al.*[78] developed an electro-thermal model to investigate the *I-V* switching characteristic of an HfO_2-based device. The CF in the HfO_2 oxide layer is identified as a region with oxygen vacancies. An energy landscape of a potential well is used to explain the ion migration, as shown in Fig. 2.13. Without the application of an electrical field, the ions diffuse randomly to all directions due to the non-direction energy barrier E_A, the diffusion direction depends on the ion concentration gradient (from high concentration to low). When a voltage is applied, ion migration would enhance along the electrical field which is due to the lowering barrier αqV in the direction of the electrical field, thus resulting in a directional drift. The ion migration including diffusion and drift is described as[78],

$$\frac{dn_D}{dt} = \nabla \cdot (D\nabla n_D - \mu E n_D) \tag{2-13}$$

where $D = D_0 e^{-\frac{E_A}{k_B T}}$ is temperature activated ion diffusivity based on Arrhenius law, μ gives the drift mobility of vacancies. The current density $J(\vec{r})$ and electrical potential are calculated based on the continuity equation[78],

$$\nabla \cdot J(\vec{r}) = \nabla \cdot (\sigma(\vec{r})\nabla\varphi(\vec{r})) = 0 \tag{2-14}$$

The corresponding generated heat based on Joule heating is described as[78],

$$-\nabla \cdot k_{th}(\vec{r})\nabla T = \sigma(\vec{r})|\nabla\varphi(\vec{r})| \tag{2-15}$$

here, $\sigma(r)$ and $k_{th}(\vec{r})$ are the electronic conductivity and thermal conductivity which are spatially dependent with oxygen vacancies concentration n_D distribution. This model

provides an important feature that it can simulate the electrothermal physics nature of the RRAM during the switching process. A significant importance of this simulation model is that it can provide a microscopic interpretation of intermediate reset or set states including the CF morphology and physical field distribution.

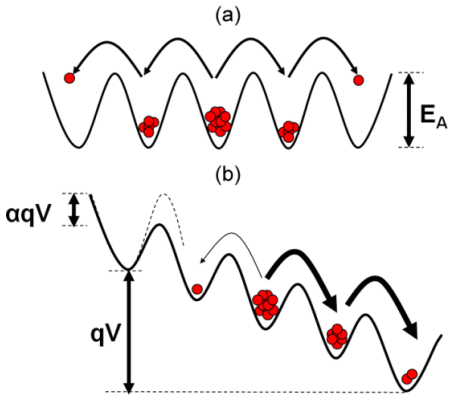

Fig. 2.13 Potential energy landscape for ion hopping at (a) zero or (b) positive applied voltage. Uniform energy barrier E_A under zero voltage makes random isotropic diffusion. The application of a voltage *V* lowering energy barrier by αqV along the field direction leads directional drift of ions[78].

The characteristics of these theoretical models are summarized in the following table.

Table 2.1 Comparison of RRAM models

	Filament gap model	Filament dissolution model	Electrons tunneling model	Electro-thermal model
Application type	Bipolar	Unipolar	Bipolar	Bipolar
State variable	Filament gap	CF boundary movement velocity (v_D)	Electrons occupation probability (p_n) and hopping rate (H_{na})	Ion concentration (n_D)
Platform	SPICE	COMSOL	KMC code	COMSOL

2.4. Prospective applications of memristor

As a passive electronic component, the memristor has potential applications in many fields based on its compatibility with conventional integrated circuits. In terms of the resistance change behavior, the memristor displays two different types: discrete resistance changes and continuous resistance change. The memristors displaying discrete resistance states are widely used in non-volatile memory and in-memory computing, while continuous resistance change provide a potential application in neuromorphic computing and artificial neural networks hardware.

Non-volatile memory

The random-access memory can be either volatile or non-volatile. Volatile memory needs a constant power to retain the stored information, when the power is removed, the data is quickly lost. Static random-access memory (SRAM) and dynamic random-access memory (DRAM) are two typical volatile memories. Although the volatile memory exhibits several advantages, e.g. high density of DDRM and fast speed of SRAM, they are volatile and a high frequency refresh is needed[90]. For non-volatile memory, it can store the data for years even after the power is removed. Currently, the mainstream non-volatile memory is Flash memory owing to its low cost and large capacity, which uses a floating-gate charge storage technology to store data. However, the Flash memory is facing a challenge to scale down which is attributed to the enhanced probability of electron tunneling caused by the size reduction, the resulting increase of leakage current affects the reliability and stability of the device[56]. Therefore, there is an urgent need to develop new non-volatile memory. Various emerging memories such as Phase Change Memory (PCM),

Magnetic Random-Access Memory (MRAM), Resistive Random-Access Memory (RRAM), and Ferroelectric Random-Access Memory (FRAM) are investigated to meet the ideal memory features, i.e., small operating voltage, long data retention time, and large cycling endurance. Table 2.2 summarizes the key features of these emerging non-volatile memories[91]. Compared to the details of characteristics, the RRAM has significant advantages for the next generation of non-volatile memory such as ultra-high speed, long data retention, large endurance, and excellent scalability.

Table 2.2 Comparison of key features of emerging non-volatile memories

Memory type	Conventional Flash		Novel Non-volatile Memories			
	NOR	NAND	FRAM	MRAM	PCM	RRAM
Cell size	45 nm	16 nm	180 nm	65 nm	45 nm	<10 nm
Cell area	10 F^2	4 F^2	22 F^2	20 F^2	4 F^2	4 F^2
Read time	15 ns	0.1 ms	40 ns	30 ns	12 ns	~ 1 ns
Write time	1 us	0.1 ms	65 ns	35 ns	100 ns	~ 1 ns
Read voltage	4.5 V	4.5 V	1.3-3.3 V	< 2 V	< 3 V	< 1 V
Write voltage	8-10 V	15-20 V	1.3-3.3 V	1.8 V	3 V	< 1 V
Retention	> 10 yr	> 10 yr	> 10 yr	> 10 yr	> 10 yr	> 10 yr
Endurance	10^5	10^5	10^{14}	10^{12}	10^9	> 10^{12}

The function of data storage for RRAM is based on the resistance states switching between HRS and LRS under the applied voltage which corresponds to the “0” and “1” states in binary, thus it can store the binary data. To increase the storage density, a lot of researches is being conducted to achieve multiple resistance states in the RRAM. For example, Wang *et al*.[39] obtain at least five stable resistive states on the Ti/Cu_xO/Pt RRAM cell by controlling the compliance current and changing the reset voltage, as shown in Fig. 2.14. Until today, multiple resistance states have been demonstrated in various metal oxide-

based RRAM systems, which is mainly attributed to the CF properties, i.e., composition, position, size, and shape of CF inside the insulator layer[45,92-94]. Therefore, there is a scope to further increase the number of resistance states by varying the properties of CF.

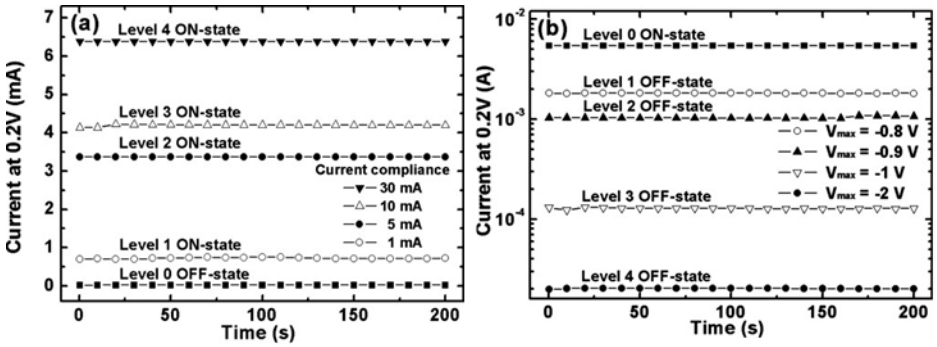

Fig. 2.14 Nondestructive readout test results of (a) the multilevel ON-states and (b) the multilevel OFF-states at a read voltage of 0.2 V[39].

In-memory computing

The conventional process cell is based on the von Neumann architecture in which the computing unit and memory unit are separated, as shown in Fig. 2.15. The data transferring between memory and computing enhances high energy consumption and lowers computing efficiency, which comes to be known as the "von Neumann architecture." The emerging RRAM crossbar array with high density and fast speed switching is designed to achieve memory and computing in the same core[95]. For example, Borghetti *et al.*[1] fabricated a Pt/TiO_2/Pt crossbar array and realized the basic Boolean logic operation IMP and NAND, the corresponding logic circuits are illustrated in Fig. 2.16. Based on their design, the memristive switching characteristic performs as the 'stateful' logic operations

for which the same device combines the logic computing and memory simultaneously which overcomes the von Neumann bottleneck and achieves in-memory computing. However, there is still a distance left before RRAM based in-memory computing unit becomes a replacement for the current CPU or GPU due to the crosstalk problem represented in the crosspoint array, the limited stability, and relatively high variability.

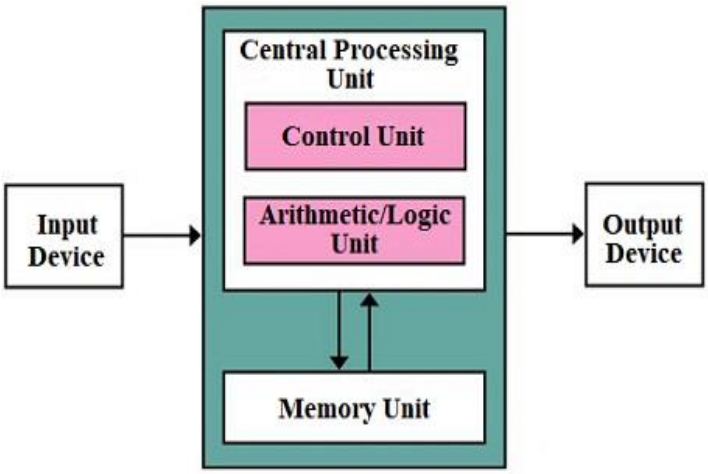

Fig. 2.15 Process cell is based on the von Neumann architecture

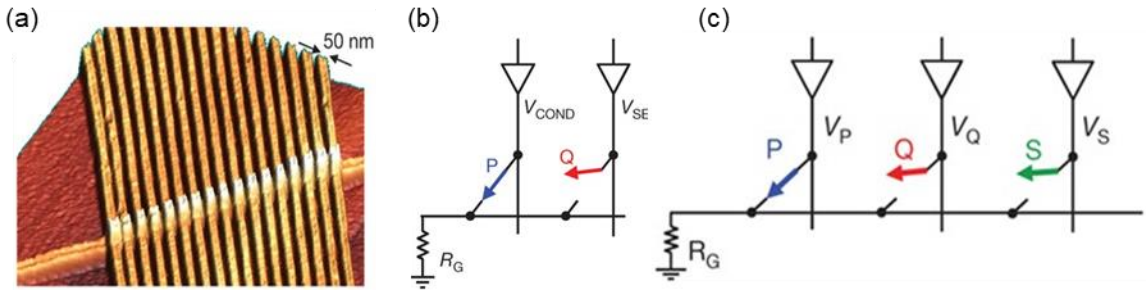

Fig. 2.16 a. AFM micrograph of a nano crossbar. b. IMP operation c. NAND operation where with P, Q and S are RRAM cell[1].

Neuromorphic computing

In 2010, Jo *et al*.[96] reported that the resistance states can change continuously in response to continuous voltage pulses in silicon-based memristors, as shown in Fig. 2.17. In addition, they did the spike-time dependent plasticity (STDP) testing which is widely known as the fundamental of neuronal circuits in the brain. They found that the testing result is similar to the STDP properties measured in the biological synaptic systems and verified the memristor can indeed be used as an artificial electronic synapse in the neuromorphic system (Fig. 2.17b and c). In a memristor-based neuromorphic computing system, the memristor crossbar corresponds to the neural network and each crosspoint in the memristor array provides the information. The input and output of the artificial neural network correspond to the input voltage signals in the memristor crossbar and the output current signals as shown in Fig. 2-18[2]. These input and output signals from memristors can be used to acquire information regarding weights through certain learning rules like STDP which is an essential parameter for ANN. Using these parameters including input, output, and weights, some advanced tasks have been realized such as pattern recognition. For example, Prezioso *et al*.[18] classified and recognized a three 3×3-pixel black/white image by using the memristor-based neuromorphic networks in 2015. In 2017, a much larger and more complex memristive neuromorphic network is developed to achieve face classification and recognition by Yao *et al*.[97] Although the memristor based synapse (i.e. memristor crossbar array) is a very promising candidate to design the ANN, it is still far from being the application of more precise and complex task as the issues like materials optimization for improving the properties of memristor cell, reduction variation for

enhancing the accuracy of AI tasks, circuit and algorithms design for extending analog computing.

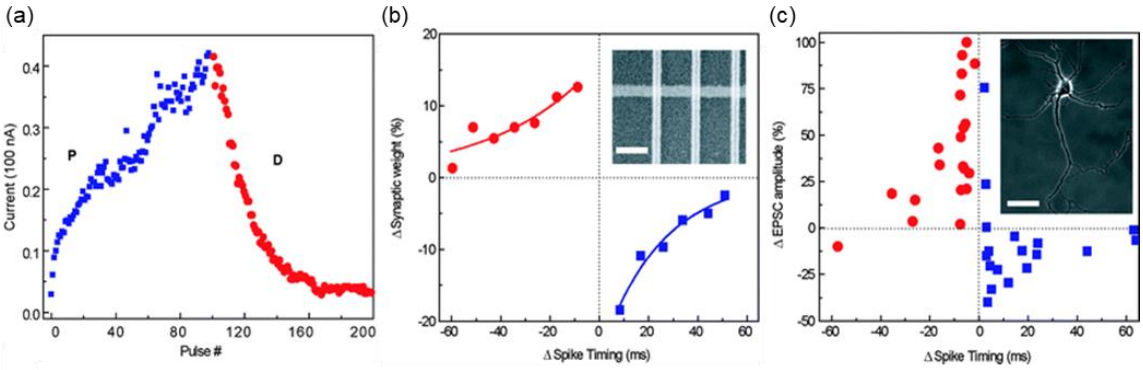

Fig. 2.17 a. Memristor response to programming pulses, the device conductance can be incrementally increased or decreased by consecutive potentiating or depressing pulses. Spike-time dependent plasticity (STDP) testing, b. the measured change of the memristor synaptic weight vs the relative timing Δt of the neuron spikes and c the measured change in excitatory postsynaptic current (EPSC) of rat hippocampal neurons[96].

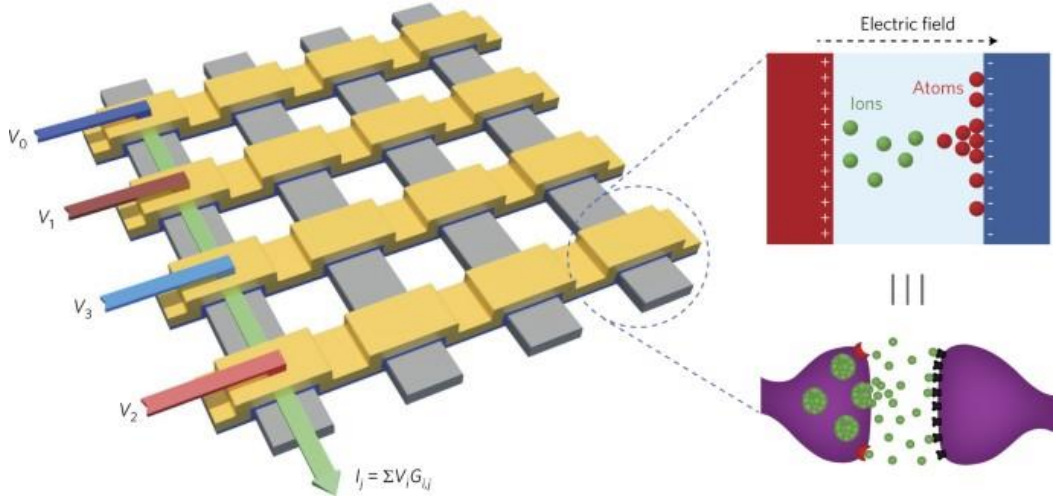

Fig. 2.18 Hardware implementation of artificial neural networks in a memristor crossbar where a memristor is formed at each crosspoint[2].

2.5. Challenges of current memristor

During the past few decades, research in the memristor field has increased remarkably and a lot of RRAM systems have been fabricated and shown encouraging properties for the application of non-volatile memory with ultra-high density in-memory computing over von Neumann bottleneck, and neuromorphic computing. However, there still exist critical challenges that limit the application of memristors, among which device reliability and variability are the main two limitations.

Device reliability

The switching between HRS and LRS in the use of resistive random-access memory is frequently. Permanent damage may be introduced at large switch cycles and causes the degradation of device performance. Generally, endurance is referred to as the number of cycles a device can switch while remaining a reliability performance is employed to assess the performance of the device. The endurance properties have been investigated in many metal oxide-based RRAM, such as the HfO_2 based resistive cell shows endurance with 10^6 cycles[98] and the TaO_x-based RRAM exhibits endurance higher than 10^{12} cycles[45]. Although the endurance of RRAM has been reported as high as 10^{12}, it is still not enough to replace the current DRAM which shows excellent endurance with 10^{16} cycles[91]. The endurance characteristics are influenced by many factors. For example, Fantini *et al.*[99] reported the endurance of an HfO_2 based device strongly influence by the size of the switch cell, wherein a larger endurance can be found in a device with a large switch cell. They proposed that the degradation in the endurance characteristic is caused by the reduction of several ions in the HfO_2 layer with the downscaling of the device to 5

nm. But an inconsistent discovery is obtained from the other TaO_x based RRAM. Goux *et al.*[100] found that endurance can be enhanced by reducing the switch layer to 3 nm. Whereas the increasing of applied pulse width and amplitude can lead to the degradation of endurance performance in $Ta/Ta_2O_5/TiN$ structure[95]. It is also found that the electrode properties also influence the endurance characteristic in which selecting Ru as the bottom electrode instead of TiN in the $Ta/Ta_2O_5/TiN$ stacking structure could enhance the endurance of the device that is because it has a reaction between the TiN and metal oxide. Therefore, it is crucial to investigate the mechanism behind the failure that benefits us to further enhance the endurance performance of the RRAM.

Generally, the final failure is found either in LRS or HRS state, and unable to set or reset back. Failure at the LRS state is more frequently observed in metal oxide-based devices[101]. The previous investigation shows that the degradation at the switch from HRS to LRS state in metal oxide-based RRAM is attributed to the extra vacancies generated in the switching layer leading to the change of original CF structure and composition that causes permanent breakdown. And the failure occurs at the opposite switch (LRS to HRS) due to the enlarged oxygen depletion gap is induced by the extra recombination between ions and oxygen vacancies or the redistribution of oxygen vacancies in the CF region[102].

Device variability

In RRAM, the poor uniformity of various devices is one of the significant challenges that limit the application in a large-scale memory array. The variation of resistance and voltage in RRAM devices includes temporal fluctuations cycle-to-cycle and spatial fluctuations device-to-device. In most metal oxide-based RRAM, the main reason

for the variation is due to the formation and rupture of CF variation. For example, Fantini *et al*.[102] reported the change in the number of oxygen vacancies which defines the critical radius and geometry of CF causes the randomness of the device. Amborgio *et al*.[103] proposed that the variability for set and reset processes is attributed to the variation of oxygen vacancies generation barrier E_a of the amorphous structure of the oxide film which influences the CF growth behavior. In addition, Baeumer *et al*.[104] use the Spectro microscopic photoemission threshold analysis and operando XAS analysis to directly observe the variability due to the change of both shape and location of the CF from cycle to cycle.

The nonuniformity in RRAM device also displays between device-to-device or cell-to-cell (in memristor crossbar) which is mainly attributed to the fabrication process such as the surface roughness of the electrodes and the microstructure randomness of each switching cell in metal oxide-based RRAM[103]. The variation of oxygen vacancies generation energy barrier and diffusion barrier may be different for the different positions like defect cluster, grain boundary and dislocation.

In summary, the reviews show that the state of the CF such as size, composition, position, and shape during the switch is the critical factor for stable reliability and sufficient cycling endurance. The engineering of filament control by electrode optimization, dielectric materials modulation, microstructure design, and fabrication process enhancement become the key techniques to improve the performance of RRAM devices. To better control the CF properties, the deep physical dynamics controlled by comprehensive physical fields, i.e., chemical, thermal, electrical, mechanical, magnetic, and sometimes quantum effects need to be fully understood.

Chapter 3. The conductive filament formation and growth behavior in metal oxide-based RRAM

Resistive switching behavior in many reported metal oxide-based RRAM devices depends on the formation/fracture of CF inside a switching layer for metal oxide-based RRAM. Many as-fabricated metal oxide-based devices are at a very high resistance state which needs a one-time step electroforming operation to establish a local CF. In this section, we developed a physical model to fundamentally understand the physical kinetics of CF formation and growth behavior and investigate how the electrode and metal oxide layer influence the CF growth behavior during the electroforming process.

3.1. Introduction

In most metal oxide-based RRAM, the electroforming operation is typically realized by applying a sufficiently high voltage or current on the film to form a CF of high $V_O^{\cdot\cdot}$ density inside the insulating layer to connect the top and bottom electrodes[34,37,38,61,63,105-107]. As a voltage is applied on the thin film for filament growth, this is commonly attributed to a high electrical field electrolytic process in which the $V_O^{\cdot\cdot}$ are generated from both the Frenkel pair inside of oxide and the oxide/electrode interface due to the chemical reactions between the oxide and the metal electrodes, and migrate to create a conduction path between electrodes driven by the electric field and thermal effect in most metal oxide-based RRAM[5,89]. Therefore, the types and properties of metal electrodes play a key role in determining CF formation and growth behaviors.

Several experimental and simulation studies have been made to understand the electrode effect on the electroforming process[4,36,53,108-111]. Chen *et al*.[5] studied the effect of electrode materials on the endurance/retention performance of HfO_2 based RRAMs. It is found that long pulse endurance can be obtained by using active metals as electrodes. Nandi *et al*.[52] reported that the electrode roughness induced a local electrical field enhancement that reduced the forming voltage. Xu *et al*.[3] developed a Kinetic Monte Carlo (KMC) model to simulate the morphology of a CF in HfO_2-based RRAM and revealed that most vacancies are generated at the metal/oxide interface due to a lower vacancy formation energy than that in the bulk. However, up to now, the role of electrode materials on the CF kinetics, such as the growth direction, composition, and uniformity of the CF, which plays a critical role in determining the stability and functionality of the subsequent switching cycles[112-115], is still less known. Furthermore, a number of metal oxides have been used as the insulating layer in metal oxide-based RRAMs, such as Al_2O_3[73], TiO_2[72], HfO_2[73], TiO_2[108], NbO[40] and, *etc*. Unfortunately, a general question arises as to what the ideal properties in metal oxides that potentially reduce the energy consumption and improve CF uniformity during the electroforming and how this knowledge could transform into a general design principle for materials selection of metal oxides for generating uniform CF. To qualitatively understand the effects of the electrode and metal oxide layer properties on the CF growth behavior and address these limitations, we develop a physical model by choosing HfO_2 as a prototype to study the dynamic of the electroforming process in metal oxide-based RRAM.

In this section, firstly, we investigate the interplays among the chemical, electrical, and thermal effects during the electroforming process. Then, the effects of the electrode

properties (the energy barrier of extracting oxygen from the oxide: E_b) and the physical properties of the oxide layer (the electrical and thermal conductivity: σ , k_{th}) on the CF morphology evolution, current-voltage characteristic, local temperature, and electrical potential distribution have been systematically explored.

3.2. Model

We chose HfO_2 as an example and study the electroforming process during which the CF is created and eventually connects one electrode to the other. In the phase-field simulation, we choose the oxygen vacancy density ($N_{V_O^{\cdot\cdot}}$) as the field variable to calculate the total free energy of the system which will be calculated as a function of $N_{V_O^{\cdot\cdot}}$. The total free energy density f_{total} concerning oxygen vacancies can be expressed as,

$$f_{total} = f_{chem} + f_{electric} \tag{3-1}$$

we only consider the chemical f_{chem} and electrical $f_{electric}$ energy contributions to the total free energy. In this model, the metal oxide with oxygen vacancies is assumed as a dilute solution, such that the chemical energy density depends on the configuration entropy of oxygen vacancy and is described as:

$$\begin{aligned} f_{chem} &= f_{perfect-crystal} - T\Delta S_{V_O^{\cdot\cdot}} \\ &= f_{perfect-crystal} - k_B T[N_O ln \frac{N_O}{N_O - N_{V_O^{\cdot\cdot}}} + N_{V_O^{\cdot\cdot}} ln \frac{N_O - N_{V_O^{\cdot\cdot}}}{N_{V_O^{\cdot\cdot}}}] \end{aligned} \tag{3-2}$$

in which $f_{perfect-crystal}$ is the energy density of perfect lattice without $V_O^{\cdot\cdot}$, $\Delta S_{V_O^{\cdot\cdot}}$ is the configuration entropy of oxygen vacancies, k_B is the Boltzmann constant, T is the

temperature, $N_O, N_{V_O^{\cdot\cdot}}$ are the total number of lattice sites of oxygen atoms and the number of oxygen vacancies. The electrostatic energy density is given by,

$$f_{electric} = 2e_0 N_{V_O^{\cdot\cdot}} \varphi - \frac{1}{2}\varepsilon_0 \varepsilon_r (\nabla\varphi)^2 \tag{3-3}$$

where φ is the electrical potential, ε_0 and ε_r are the vacuum permittivity and relative permittivity, respectively.

Based on the chemical energy density and the electrostatic energy density calculated from Eqs. (3-2) and (3-1), the total free energy density f_{total} is obtained. The chemical potential of the system ($\mu_{V_O^{\cdot\cdot}}$) can be calculated by taking the variational derivative of f_{total} over $N_{V_O^{\cdot\cdot}}$,

$$\mu_{V_O^{\cdot\cdot}} = \frac{\delta f_{total}}{\delta N_{V_O^{\cdot\cdot}}} = k_B T ln \frac{N_{V_O^{\cdot\cdot}}}{N_O - N_{V_O^{\cdot\cdot}}} + 2e\varphi \tag{3-4}$$

And the flux of the oxygen vacancy migration ($J_{V_O^{\cdot\cdot}}$) is defined to be linearly proportional to the chemical potential gradient ($\nabla\mu_{V_O^{\cdot\cdot}}$):

$$J_{V_O^{\cdot\cdot}} = -\frac{D}{k_B T} N_{V_O^{\cdot\cdot}} \nabla\mu_{V_O^{\cdot\cdot}} \tag{3-5}$$

where D is the diffusivity of $V_O^{\cdot\cdot}$, which is assumed as to be temperature dependent through the Arrhenius relation $D = D_0 e^{-\frac{E_A}{kT}}$. Here D_0 is the pre-exponential factor of diffusivity and E_A is the diffusion energy barrier. In HfO_2 system, we use $D_0 = 2\times10^{-3}$ cm^2/s and $E_A = 1$ eV based on literature[116]. Thus, the $V_O^{\cdot\cdot}$ transport can thus be described by the continuum equation, which also is known as Nernst-Planck equation,

$$\frac{\partial N_{V_O^{\cdot\cdot}}}{\partial t} = -\nabla \cdot J_{V_O^{\cdot\cdot}} = \nabla \cdot \left(D\nabla N_{V_O^{\cdot\cdot}} + \frac{eD}{k_B T} N_{V_O^{\cdot\cdot}} \nabla\varphi \right) + G \tag{3-6}$$

Here, G is the generation term during electroforming and set processes. The kinetics of electroforming and set processes can be interpreted as a soft breakdown associated with $V_O^{\cdot\cdot}$ generation. Generally, there has two main sources of $V_O^{\cdot\cdot}$ generation. First, the $V_O^{\cdot\cdot}$ are likely to be created from Frenkel pair inside the bulk of the oxide layer, when the electrodes are inert metals or compounds, such as TiN and Pt [34,108,117]. The formation reaction is expressed in the Kröger-Vink notation as follows,

$$O_O^{\times} \rightarrow V_O^{\cdot\cdot} + 2e' + \frac{1}{2}O_{2(g)}$$

Second, the $V_O^{\cdot\cdot}$ can be induced at the anode/oxide interface by extracting the oxygen atoms from oxide based on the following chemical reaction, which is usually observed in the systems using an active metal with high oxygen affinity as the anode electrode, such as Ti, Ta, Hf [4,33,36,110,118,119].

$$M_{electrode} + HfO_2 \rightarrow MO_\delta + HfO_{2-\delta} + \delta V_O^{\cdot\cdot} + 2\delta e'$$

where $O_O^{\times}$ denotes the lattice oxygen, $M_{electrode}$ stands for the electrode metal. The bulk generation rate of $V_O^{\cdot\cdot}$ at the interior of the oxide is determined by [120],

$$G_{bulk} = G_1 \cdot \left[\exp\left(\frac{-(E_f - \gamma E)}{k_B T}\right)\right] \quad (3\text{-}7)$$

The interface generation rate has a similar form [121],

$$G_{inter} = G_2 \cdot \left[\exp\left(\frac{-(E_b - \gamma E)}{k_B T}\right)\right] \quad (3\text{-}8)$$

where G_1 and G_2 are the pre-exponential factors for bulk and interface generation rates, respectively, γ is the bond polarization factor, E is the local electrical field. The bulk

vacancy formation barrier E_f represents the capacity of Frenkel pair generation inside the oxide. The interface vacancy formation barrier E_b indicates the ability of a metal to extract oxygen atoms from the HfO_2, which is determined by the properties of elelctrode materials. In this section, to focus on investigating the electrode properties of the CF growth behavior, we ignore the bulk generation of $V_{\ddot{O}}$ and assume that the $V_{\ddot{O}}$ generation only occurs at the active anode/oxide interface. Therefore, we select both chemically active metals (Ti and Ta) and inert metals (W and Pt) as anodes with different values of E_b, to understand the effect of anode materials on the CF growth behavior during the electroforming process.

To calculate the potential in device, the current continuity equation $\nabla \cdot J(\vec{r}) = 0$ is solved. The current density $J(\vec{r}) = \sigma(\vec{r})E(\vec{r})$ calculated by Ohm's law depending on local electrical conductivity $\sigma(\vec{r})$ and local electrical field $E(\vec{r}) = -\nabla\, \varphi(\vec{r})$. Thus, the current continuity equation can be rewritten with electrical potential and electrical conductivity,

$$\nabla \cdot \sigma \nabla \varphi = 0 \tag{3-9}$$

The current is given by a cross-section integral

$$I = \int \sigma \nabla \varphi \, ds \tag{3-10}$$

Finally, the Fourier heat-flow equation is solved to calculate the local temperature profile,

$$-\nabla \cdot k_{th} \nabla T = \sigma |\nabla \varphi|^2 \tag{3-11}$$

where σ and k_{th} are the electrical and thermal conductivity.

The model reduces the 3D problem to a 2D axisymmetric representation with a radial coordinate *x* and axial coordinate *z*, as illustrated in Fig. 3.1a. The total simulation

size is 20×80 nm^2 and the mesh size is selected as 0.5 nm. The 10 nm metal oxide layer is sandwiched between the 50 nm Pt bottom electrode and the 20 nm top electrode (Ti, Ta, W, Pt) where an external voltage is applied on the top electrode and the bottom electrode is grounded. Initially, the oxide layer is at a high resistance state with relatively low oxygen vacancy density, which is assumed to be uniformly distributed in the oxide layer, at a concentration of $N_{V_O^{\cdot\cdot}} = 6\times10^{19}\ 1/\mathrm{m}^3$. We assume the oxygen exchange takes place at the interface between anode and oxide in a confined region ($x = 0\sim5, z = 10$ nm), as shown in Fig. 3.1a. The $V_O^{\cdot\cdot}$ generation rate is controlled by Eq. 3-8 which is employed as the boundary condition for the $V_{\dot{O}}$ transport equation Eq. 3-6 at the anode/oxide interface. The grounded Pt cathode is chemically inert, so that there is no oxygen exchange flux at the oxide/cathode interface. The temperature at the surfaces of the two electrodes is fixed at 300 K. The boundary condition is summarized by,

$$J_{V_O^{\cdot\cdot}}\Big|_{\mathrm{z\,=\,0}} = J_{V_O^{\cdot\cdot}}\Big|_{\mathrm{z\,=\,10nm}} = G_{inter}\ \frac{1}{\mathrm{m^2 s}}$$

$$T\Big|_{\text{all boundaries}} = 300\ \mathrm{K}$$

$$\varphi\Big|_{\mathrm{z\,=\,-50}} = 0\ \mathrm{V},\ \varphi\Big|_{\mathrm{z\,=\,30nm}} = V_{\mathrm{app}}\ \mathrm{V}$$

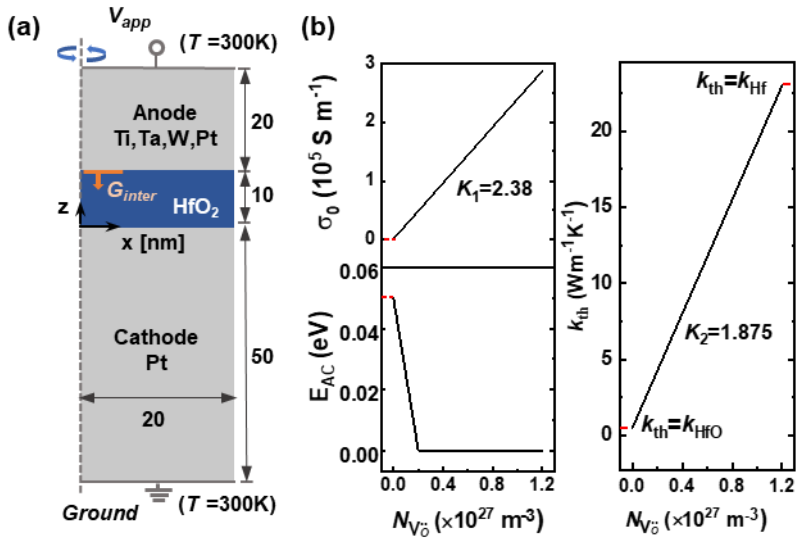

Fig. 3.1. Model geometry and simulation parameters. a. Model size and geometry. Voltage is applied at the top electrode (anode) and the bottom electrode is grounded (cathode). Oxygen exchange is assumed to take place at the interface between anode and oxide in a confined region (x = 0~5, z = 10 nm). b. Electrical conductivity preexponential factor σ_0, activation energy for conduction E_{AC}, thermal conductivity k_{th} as a function of local oxygen vacancy density $N_{V_O^{\cdot\cdot}}$.

For metal oxide-based RRAM, the CF is assumed to be in metallic phase consisting of high oxygen vacancy density. Therefore, the electroforming process can be considered a self-doping process, in which each oxygen vacancy acts as a donor that introduces two extra electrons. Thus, the local electrical conductivity of the oxide is strongly dependent on the oxygen vacancy density $N_{V_O^{\cdot\cdot}}$. The electrical conductivity is described by the Arrhenius equation[78-80], $\sigma = \sigma_0 e^{-\frac{E_{AC}}{kT}}$, where σ_0 is a pre-exponential factor and E_{AC} is the activation energy for conduction. Thus, both E_{AC} and σ_0 should depend on $N_{V_O^{\cdot\cdot}}$.

As shown in Fig. 3.1b, we assume that σ_0 is linearly proportional to $N_{V_O^{\cdot\cdot}}$ with a slope of $K_1 = 2.38$ for HfO_{2-x}. This assumption is based on the previous experimental[7] and theoretical results[78]. The E_{AC} is assumed to be 0.05 eV at $N_{V_O^{\cdot\cdot}} = 0$, which is in agreement

with the activation energy in pure HfO_2[78]. When $N_{V_O^{\cdot\cdot}}$ is lower than 0.2×10^{27} 1/m^3, E_{AC} is assumed to decrease linearly with increasing $N_{V_O^{\cdot\cdot}}$. E_{AC} is to be zero when $N_{V_O^{\cdot\cdot}}$ is greater than 0.2×10^{27} 1/m^3, which corresponds to the metallic CF nature. On the other hand, a linear relationship between k_{th} and $N_{V_O^{\cdot\cdot}}$ with a slope of $K_2 = 1.875$ for HfO_{2-x} materials is assumed due to the Joule heating, which is related with the ratio of electrical and thermal conductivity based on the Wiedemann-Franz Law[78,79], as shown on Fig. 3.1b. The minimum $k_{th} = 0.5$ W/(m·K) for $N_{V_O^{\cdot\cdot}} = 0$ is selected that corresponds to the thermal conductivity of the insulating HfO_2 material[122]. The maximum k_{th} value at high $N_{V_O^{\cdot\cdot}}$ corresponds to the metallic CF, which is equal to the thermal conductivity of metal hafnium (57.5 W/(m·K))[123]. Based on the assumptions that σ and k_{th} are linearly proportional to the oxygen vacancy density $N_{V_O^{\cdot\cdot}}$, the electrical/thermal conductivity of different metal oxides can simply be represented by tuning the magnitudes of K_1 and K_2. This enables us to easily investigate the effects of the electrical and thermal conductivity of different metal oxides on the CF growth behavior.

The simulation involves the self-consistent solutions of the Nernst-Planck equation (Eq. 3-6) for $V_O^{\cdot\cdot}$ migration with a flux boundary condition defined by Eq. 3-8 at anode/oxide interface, the current continuity equation (Eq. 3-9) for electronic conduction, and the thermal transport equation (Eq. 3-11) for Joule heating. These equations are solved using the finite element method based on the platform of COMSOL Multi-physics.

3.3. Results and discussion

3.3.1. Conductive filament growth

In this simulation, we choose HfO_2 as the metal oxide layer for the simulation. The Tantalum (Ta) is employed as the anode electrode with a vacancy formation barrier of 2.5 eV[5], and a voltage sweep rate (dV/dt) of 1 V/s is applied on the Ta electrode. In actual experimental process, a compliance current I_{cc} is always employed to be the stop condition to avoid permanent breakdown[124]. In the simulation work, we also set up the stop conditions, the electroforming will stop when the current reaches 100 μA, which is consistent with most experimental cases. Fig. 3.2a shows the current evolution characteristic. It is clearly seen that the current increases exponentially during the electroforming process. Initially, the current of the device increases gradually until the forming voltage ($V_f = 2.49$V), where an abrupt increase of current is seen. This indicates that the electroforming process occurs at a critical threshold voltage, instead of a cumulative phenomenon in the filament growth. The increasing $V_{\ddot{O}}$ concentration is controlled by the $V_{\ddot{O}}$ generation rate at the anodic interface. To further understand this behavior, we plot the evolutions of the $V_{\ddot{O}}$ generation rate, the electrical field, and the temperature at the anodic interface under applied voltage sweep, as shown in Fig. 3.2b. It should be noted that the initial generation rate is small and gradually increases with the increasing voltage due to the lower electrical field and temperature. When the forming voltage reaches V_f, the sudden increases of the electrical field and temperature at the anodic interface give rise to a self-acceleration of the $V_{\ddot{O}}$ generation flux at a very short time as shown in Fig. 3.2b, which results in an abrupt electroforming transition. Fig. 3.2c illustrates

the 2D maps of the oxygen vacancy distribution ($N_{V_O^{\cdot\cdot}}$) at different stages, corresponding to the points A to D as marked in Fig. 3.2a. It is seen that $V_O^{\cdot\cdot}$ are generated at the anode interface and start to accumulate to the cathode when the voltage is up to 2 V, as shown in snapshot A in Fig. 3.2c. At this stage, the total concentration of $V_O^{\cdot\cdot}$ is small due to the small generation rate. Along with the applied voltage, more $V_O^{\cdot\cdot}$ are generated at the anode and gradually accumulate near the cathode resulting in local segregation, as shown in snapshot B in Fig. 3.2c. As the applied voltage further increases to V_{f}, massive $V_O^{\cdot\cdot}$ are generated and migrate towards the cathode immediately, and the CF length increases suddenly resulting in a small $V_O^{\cdot\cdot}$ depletion gap near the anode, as shown in Fig. 3.2c (C) and (D). We also analyze the 1D profiles of the oxygen vacancy density $N_{V_O^{\cdot\cdot}}$, temperature T, and electrical potential φ along the cylindrical symmetry axis ($r = 0, z = 0\sim10$ nm) at the final electroforming state D (Fig. 3.2c). Here, we only plot T and φ inside the oxide layer ($z =$ 0~10 nm), as their variations inside the top and bottom electrodes are negligible. Compared to the initial oxygen vacancy density ($N_{V_O^{\cdot\cdot}} = 6\times10^{19}$ 1/m^3), the final $N_{V_O^{\cdot\cdot}}$ near the cathode increases by almost 10^7, indicating the occurrence of a metal-insulator (Mott) transition. Based on the previous literature[55], the critical $V_O^{\cdot\cdot}$ concentration (N_c) at Mott transition for metal oxide is ~10^{25} 1/m^3. As the $V_O^{\cdot\cdot}$ accumulation near the cathode and a depletion gap near the anode, the electrical potential dramatically drops near the anode, and remains almost constant in the highly conductive CF region near the cathode, which results in a local enhancement of electrical field and temperature near the anode region. The local enhancements of temperature and electrical field further increase the $V_O^{\cdot\cdot}$ mobility and promote the $V_O^{\cdot\cdot}$ migration from the gap region to the cathode. In this case, the $V_O^{\cdot\cdot}$ generation rate is slightly limited and cannot fully compensate the $V_O^{\cdot\cdot}$ migration rate from

anode to cathode. Therefore, a small $V_O^{\cdot\cdot}$ depletion region ($N_{V_O^{\cdot\cdot}} < N_c$) inside the CF is observed near the anode ($z = 10$ nm), while the $N_{V_O^{\cdot\cdot}}$ in the remaining part of CF is higher than N_c. Based on these studies, it can be inferred that the generation rate of $V_O^{\cdot\cdot}$ at the interface and the migration of $V_O^{\cdot\cdot}$ in the bulk influence the CF morphology and growth behavior.

The CF growth behavior and *I-V* characteristic simulated from the current model agree well with previous experimental reports on HfO_2-based devices[5,7,52]. For example, Chen *et al*.[5] found that the forming voltage for HfO_2 based RRAM with Ta anode is about 3 V, which is slightly higher than our simulation result ($V_f = 2.49$ V). This is probably because the area of the switching cell in their experiment is larger than our simulation. Other experimental results of metal oxide-based RRAMs[55,117,124-126] also show that the soft breakdown of the insulating layer occurs when the voltage sweep is applied, followed by a dramatic current increase at a critical threshold voltage (V_f) during the electroforming process, which agrees with our simulation results. Therefore, in the following sections, we will employ this model to investigate the effects of the electrode materials and the metal oxide properties on the CF growth behavior during the electroforming process and derive a general principle for materials selection of both metal electrodes and oxide layer in RRAMs.

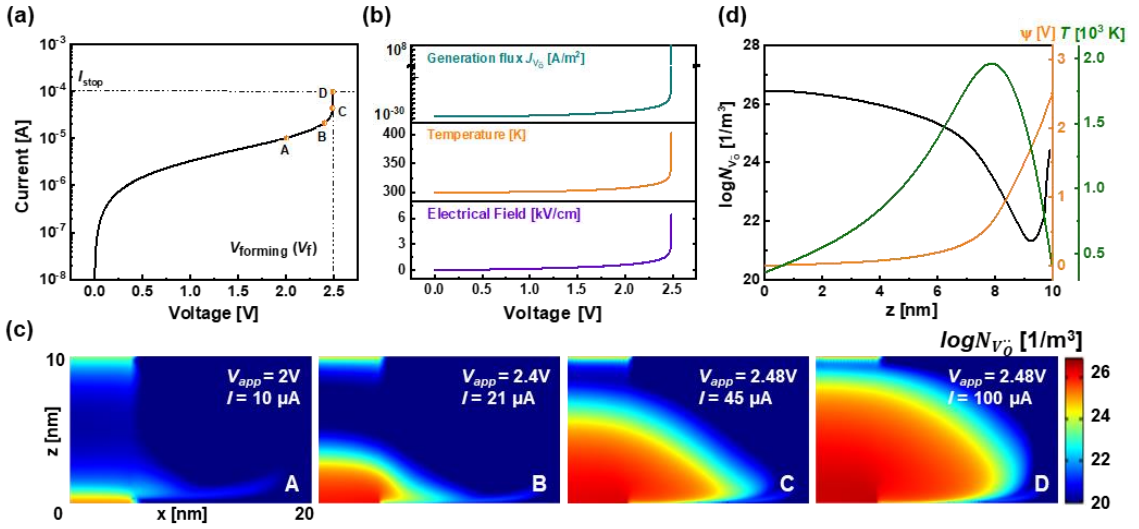

Fig. 3.2. Modeling electroforming process in HfO_2 metal oxide. a. Current evolution characteristics by applied voltage sweep with rate dV/dt=1 V/s and stop at $I_{stop} = 100$ μA. b. The evolution of generation flux, temperature T and electrical field E at the anodic interface ($z = 10$). c. Calculated 2D $N_{V_O^{\cdot\cdot}}$ map with increasing voltage, corresponding to state A-D in a. d. 1D profiles of $N_{V_O^{\cdot\cdot}}$, T and φ at state D ($V_f = 2.49$ V) along the center of CF ($x = 0, z = 0$~10 nm).

3.3.2. The effect of electrode properties on the CF growth behavior

As the oxygen vacancy generation rate is determined by the chemical reaction, and the generation rate at the anodic interface is highly associated with the electrode properties that is the ability to extract the oxygen atoms from HfO_2. It is much easier for the active electrode to extract oxygen from oxide which shows a lower vacancy formation barrier than inert electrodes. In this section, we investigate the effect of different electrodes on the CF growth behavior by choosing Ti, Ta, W, and Pt as the anode electrode with an increasing vacancy formation barrier E_b of 0.6 eV, 2.5 eV, 5.5 eV, and 8.5 eV, respectively[5]. With the same simulation conditions as section 3.3.1, a voltage sweep with the rate of dV/dt=1 V/s is applied on the anode, and the simulation is stopped at $I_{stop} = 100$ μA or $V_{app} = 5$ V, whichever comes first. The temporal evolutions of the overall

current with different anode materials (Ti, Ta, W, Pt) are illustrated in Fig. 3.3a. The currents in all cases increase exponentially with increasing voltage, followed by an abrupt increase at different forming voltages except for Pt. Based on our calculations, the required forming voltage V_{f} for the CF formation in growing with increasing E_b. The Ti electrode with the smallest E_b is found to be able to form CF at the smallest forming voltage $V_{\mathrm{f}} =$ 1.19 V. In contrast, the device with an inert Pt electrode doesn't show an abrupt increase in current even after the applied voltage reaches 5V.

We also study the effect of electrode properties on the CF morphology. The 2D maps of final $V_O^{\cdot\cdot}$ profiles (snapshots A-D in Fig. 3.3b) and the temperature distributions (snapshots E-H in Fig. 3.3b) with different metal anodes, as well as the corresponding 1D profiles of $N_{V_O^{\cdot\cdot}}$ along the center of CF ($x = 0, z =$ 0~10 nm) (Fig. 3.3c), are conducted to describe the effect of electrode properties on the CF growth. These results indicate that the interfacial properties significantly affect the final morphology of the CF. More uniform CF with homogeneous $V_O^{\cdot\cdot}$ distribution can be obtained by employing active anode metal where E_b is small (Ti/HfO_2 interface). As E_b increases, the width of the depletion gap increases and $N_{V_O^{\cdot\cdot}}$ in the CF becomes highly inhomogeneous as the shadows shown in Fig. 3.3c. In addition to the increasing gap, the $V_O^{\cdot\cdot}$ also diffuse along the radial (x) direction and broaden the CF width with increasing E_b, as observed from Fig. 3.3b (A-C). The inhomogeneous morphology of CF can be explained as the enhanced required forming voltage (V_{f}) for increasing E_b provides a larger driving force and further forces the $V_O^{\cdot\cdot}$ generation at anodic interface and migration to the cathode, resulting in a wider depletion gap. In the meantime, the corresponding increasing electrical field induced by high forming voltage leads to a temperature increase at the gap region (Fig. 3.3b (E-F)) based on the Joule heating effect,

which further increases the diffusivity of $V_O^{\cdot\cdot}$ and eventually causes the lateral broadening of the CF. Moreover, the CF is not able to form with the inert Pt electrode ($E_b = 8.5$ eV) even when the applied voltage reaches 5 V and the corresponding temperature becomes extremely high, which means, to create CFs in HfO_2 with Pt electrode, a much higher voltage is needed, under which the $V_O^{\cdot\cdot}$ tend to generate from the interior of the oxide[52] rather than the interface controlled CF growth.

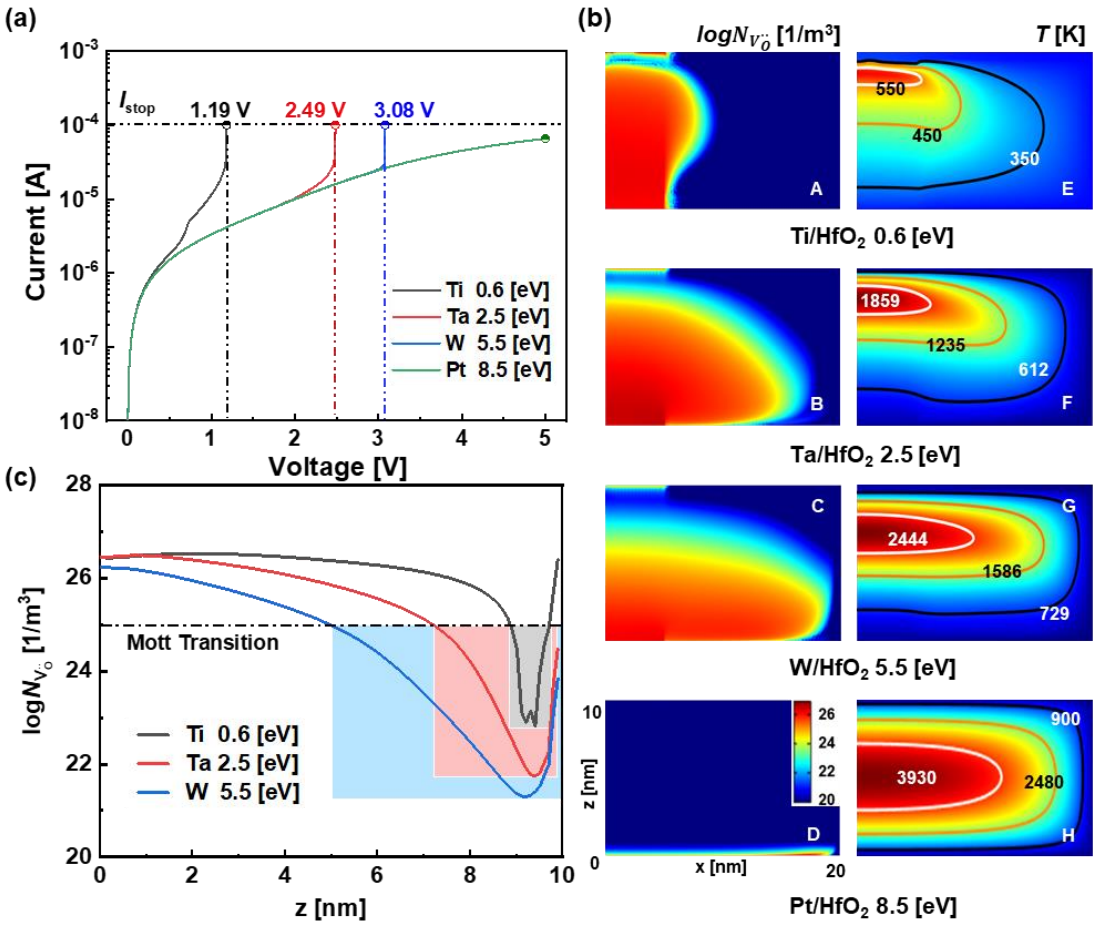

Fig. 3.3. Effect of electrode properties on the CF growth. a. Current evolution characteristics with different electrode materials under an applied voltage sweep with rate dV/dt=1 V/s and stop at $I_{stop} = 100$ μA or $V_{stop} = 5$ V. b. 2D $N_{V_O^{\cdot\cdot}}$ maps of distributions of $N_{V_O^{\cdot\cdot}}$ and temperature T along the center of CF ($x = 0, z =$ 0~10 nm) at final state. c. 1D profiles of $N_{V_O^{\cdot\cdot}}$ along the center of CF ($x = 0, z =$ 0~10 nm) at the final state (The blue, red, and grey shades indicate the position and width of the oxygen vacancy depletion gap).

To further understand the dynamic during the electroforming process, in particularly the CF growth direction, we investigate the interplays between the $V_O^{\cdot\cdot}$ generation at the anodic interface and the $V_O^{\cdot\cdot}$ migration in the bulk of HfO_2 with different metal electrodes. The 1D temporal evolutions of $N_{V_O^{\cdot\cdot}}$ along the center axis ($r = 0, z =$ 0~10 nm) with active anode Ti ($E_b = 0.6$) and inert anode W ($E_b = 2.5$ eV) are plotted in Fig. 3.4a and 3.4b. We also compared the $V_O^{\cdot\cdot}$ generation flux at the anodic interface ($x =$ 0, $z = 10$ nm) and the $V_O^{\cdot\cdot}$ drift and diffusion flux near the anodic interface ($x = 0, z =$ 8.5 nm) under the applied voltage sweep, as shown in Fig. 3.4c and d, respectively. From Fig. 3.4a, it is seen that $N_{V_O^{\cdot\cdot}}$ near the anode quickly increases above N_C and reaches ~10^{27} 1/m^3. This is due to the low vacancy formation barrier E_b allows the generation flux can reaches above 10^{-1} A/m^2 at the beginning, which is much higher than the initial migration flux (diffusion and drift), as shown in Fig. 3.4c. As the applied voltage increases from 0.1 to 0.7, the created $V_O^{\cdot\cdot}$ near the anode (z = 10 nm) gradually migrates to the cathode. As a result, the filament consisting of relatively high $N_{V_O^{\cdot\cdot}}$ starts to grow from the anode toward the cathode (indicated by the arrow in Fig. 3.4a). In this period, the $V_O^{\cdot\cdot}$ migration to the cathode is driven by the diffusion and drift flux, while the contribution of diffusion is larger than drift due to a large positive concentration gradient caused by the higher generation rate at the anodic interface. When the voltage increases to ~1 V, $V_O^{\cdot\cdot}$ can easily be removed from the anode and migrate to the cathode which results in an increasing drift flux (green curve in Fig. 3.4c). Consequently, the $N_{V_O^{\cdot\cdot}}$ near the cathode eventually increases above N_C, and a $V_O^{\cdot\cdot}$ depletion gap is created near the anode region (blue curve in Fig. 3.4a). The $V_O^{\cdot\cdot}$ continue to accumulate to the cathode side as the V_{app} further increases to 1.19 V, and the $N_{V_O^{\cdot\cdot}}$ near cathode reaches ~10^{27} 1/m^3. We can also observe the width of the

depletion gap decreases, and the location of this gap moves towards the anode. This behavior can be explained as follows. As the generated $V_O^{\cdot\cdot}$ migration to the cathode region under the application of voltage, once the depletion gap near the anode is created, a negative $V_O^{\cdot\cdot}$ concentration gradient (from cathode to anode) is induced which provides a negative diffusion flux as indicated by the orange dotted curve in Fig. 3.4c. Meanwhile, the positive drift flux (solid green curve in Fig. 3.4c) is always consistent with the direction of the electrical field. Consequently, the gap induced negative diffusion flux partially offsets the positive drift flux and drives the $V_O^{\cdot\cdot}$ diffusion towards the anode to reduce the width of the depletion gap. It is demonstrated that for the active anode, the CF growth direction is from anode to cathode and a relatively uniform CF is eventually formed, as the arrow shown in Fig. 3.4a.

The calculated CF growth dynamic under a relatively inert electrode (W) with a higher $E_b = 5.5$ eV is plotted in Fig. 3.4b and d. The initial $V_O^{\cdot\cdot}$ is uniform in the oxide layer at $V_{\text{app}} = 0$ V. Due to the large vacancy formation barrier, the generation rate of $V_O^{\cdot\cdot}$ is negligible at the beginning, as shown in Fig. 3.4d. As the applied voltage increase to 2.5 V, the $V_O^{\cdot\cdot}$ are forced to be depleted from the anode and piled up to the cathode side, accompanied by the creation of a wide $V_O^{\cdot\cdot}$ depletion gap near the anode (blue curve in Fig. 3.4b) due to the positive drift flux (solid green curve in Fig. 3.4d) is much larger than the $V_O^{\cdot\cdot}$ generation flux at the anodic interface (solid blue curve in Fig. 3.4d), while the negative diffusion flux (dotted orange curve in Fig. 3.4d) only partially offsets the drift flux. The $V_O^{\cdot\cdot}$ generation flux is gradually enhanced as the applied voltage increase, and $N_{V_O^{\cdot\cdot}}$ start to increase at the anode side (2.7 V state in Fig. 3.4b) and further migrate towards the cathode as the increasing drift and diffusion flux both contribute to the migration flux from anode

to cathode. Consequently, a CF with a higher concentration $N_{V_O^{\cdot\cdot}} > N_C$ first appears at the cathode side (3.0 V state in Fig. 3.4b) and continues to grow towards the anode when voltage is above 3.0 V, as indicated by the arrow in Fig. 3.4b.

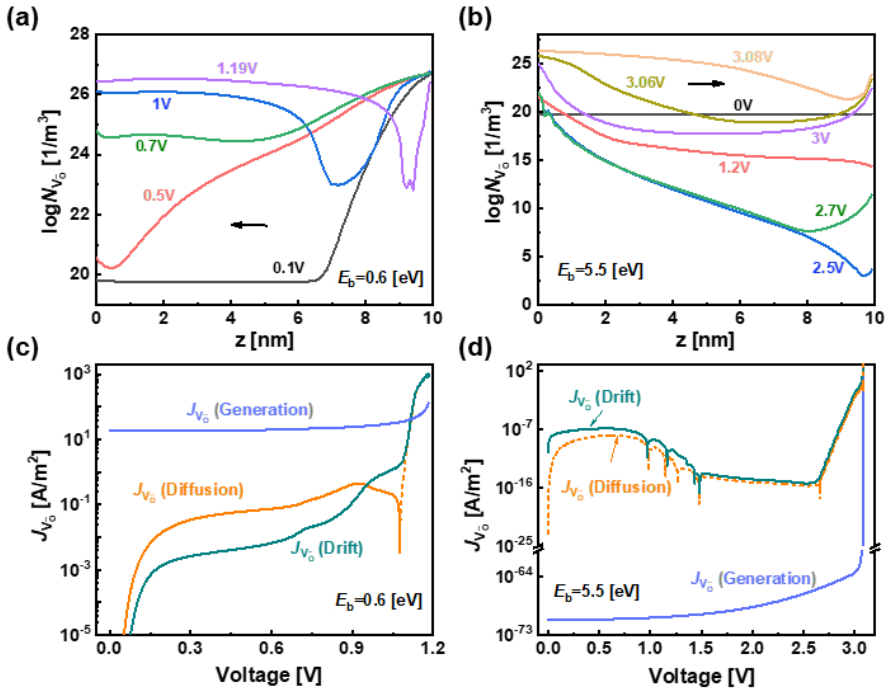

Fig. 3.4. The competition between the generation rate and migration rate. a, b. The evolution of distributions of $N_{V_O^{\cdot\cdot}}$ along the center of CF ($x = 0, z = 0$~10 nm) with an active electrode Ti and an inner electrode W under a voltage sweep rate dV/dt=1 V/s. c, d The generation flux at the point in interface ($x = 0, z = 10$ nm), the drift and diffusion flux at the point near the anode ($x = 0, z = 8.5$ nm) with Ti and W electrodes, respectively. Flux direction from anode to cathode is marked as solid line, while flux direction from cathode to anode is marked as dotted line.

3.3.3. The effects of metal oxides properties on the CF growth behavior

In this section, we study the effect of metal oxide properties on CF growth behavior. Based Eqs. 3-9 and 3-11, we can deduce that the local electrical field and temperature strongly affect the oxygen vacancy transport and thus influence the CF growth. The electrical and thermal transports are highly dependent on the oxide properties, such as the

electrical (σ) and thermal conductivity (k_{th}) of the host metal oxides. Since σ and k_{th} in the metal oxides are much smaller than their corresponding metallic states, for simplicity, we assume that σ and k_{th} are the same for different pristine oxides (such as TiO_2, HfO_2, *etc*.), and are linearly extrapolated to their values in the corresponding metallic states as a function of increasing $N_{V_O^{\cdot\cdot}}$. Based on this assumption, we can easily represent the σ and k_{th} for different metal oxides by tunning the slopes of the linear curve, i.e., K_1 and K_2, as mentioned in section 3.2.

To investigate the effect of electrical conductivity on CF growth, we assume the vacancy formation barrier is a constant ($E_b = 2.5$ eV). Fig. 3.5 illustrates the effect of electrical conductivity on CF growth. The total current evolution with different electrical conductivities (represented as $K_1 = 0.5$, 2.38 and 10.5) is shown in Fig. 3.5a. While the initial current evolutions are almost the same for different K_1, the forming voltage (V_f), as indicated by a sudden increase in total current, decreases monotonously with the increasing of electrical conductivity (K_1). Fig. 3.5c illustrates the 2D maps of the final $V_O^{\cdot\cdot}$ distribution with different electrical conductivities, and the corresponding 1D $N_{V_O^{\cdot\cdot}}$ profiles along vertical ($x = 0, z = 0$~10 nm) are shown in Fig. 3.5b. Under lower electrical conductivity ($K_1 = 0.5$), we can find a larger depletion gap, and the width of the gap diminishes in size with the increasing of electrical conductivity of the oxide. As K_1 reaches 10.5, the $N_{V_O^{\cdot\cdot}}$ becomes homogenous and the CF becomes uniform in morphology. To understand the effect of electrical conductivity, we compare the 1D electrical potential and the local temperature distributions along the vertical direction ($x = 0, z = 0$~10 nm) at the final forming states with different electrical conductivities, as shown in Fig. 3.5d and e. The heat generation by Joule heating effect is reduced when σ is low (K_1 =0.5) (black curve in Fig.

3.5e). Consequently, the $V_O^{\cdot\cdot}$ generation rate becomes low under lower temperature, and a larger V_f is needed to create a CF (Fig. 3.5a). The higher applied voltage accelerates $V_O^{\cdot\cdot}$ migration from anode to cathode, creating a local segregation of $V_O^{\cdot\cdot}$ at the cathode. As a result, the electrical voltage remains constant from the cathode towards the inside bulk ($z = 0 \sim 7$ nm) and increases dramatically towards the anode (black curve in Fig. 3.5d). This results in a local enhancement of the electrical field, which further speeds up the $V_O^{\cdot\cdot}$ migration and accumulation near the cathode, and eventually induces a large depletion gap near $z = 7$ nm (Fig. 3.5b, c). More heat is generated (red curve in Fig. 3.5e) as σ increases ($K_1 = 2.38$), which prompts the $V_O^{\cdot\cdot}$ generation and reduces the forming voltage. Compared with the case $K_1 = 0.5$, the smaller local electric field enhancement (red curve in Fig. 3.5d) reduces the driving force for $V_O^{\cdot\cdot}$ migration towards the cathode, resulting in a smaller depletion gap. When $K_1 = 10.5$A, a large amount of heat is produced (blue curve in Fig. 3.5e). This leads to a larger $V_O^{\cdot\cdot}$ generation flux and a reduction of forming voltage that reduces the local enhancement of the electrical field (blue curve in Fig. 3.5d) and slows down the $V_O^{\cdot\cdot}$ drift to the cathode. On the other hand, the enhanced temperature promotes the $V_O^{\cdot\cdot}$ diffusion from the cathode region of high $V_O^{\cdot\cdot}$ concentration towards the $V_O^{\cdot\cdot}$ depletion gap to reduce the concentration gradient, and eventually offsets the $V_O^{\cdot\cdot}$ drift by the local electric field. As a result, the $V_O^{\cdot\cdot}$ depletion gap near the anode and the $V_O^{\cdot\cdot}$ segregation near the cathode almost disappear (blue curve in Fig. 3.5b), and the uniformity of the $V_O^{\cdot\cdot}$ concentration inside the CF is significantly improved (snapshot C in Fig. 3.5c).

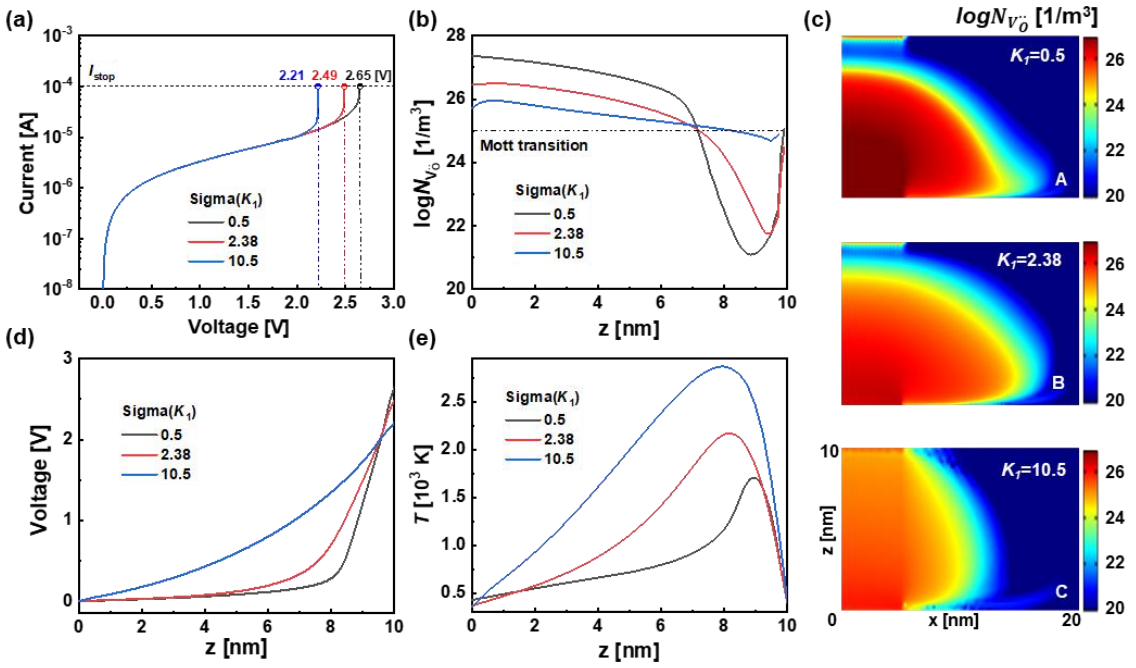

Fig. 3.5. Effect of electrical conductivity on the CF growth. a. Current characteristic with different electrical conductivity (by K_1) under a voltage sweep rate dV/dt=1 V/s. b. $N_{V_O^{\cdot\cdot}}$ ditributions along the center of CF ($r = 0, z = 0$~10 nm). c. Calculated 2D $N_{V_O^{\cdot\cdot}}$ map. d, e. Calculated 1D profiles of local electrical potential φ and temperature T along the center of CF ($r = 0, z = 0$~10 nm) at final state.

The effect of thermal conductivity k_{th} (by the slope K_2) on the CF growth is illustrated in Fig. 3.6. Fig. 3.6a shows the temporal evolution of total current with different k_{th} (represented as $K_2 = 0.1$, 1.875 and 10.5). The lower k_{th} ($K_2 = 0.1$) results in a higher temperature (black curve in Fig. 3.6e) which promotes the $V_O^{\cdot\cdot}$ generation at a reduced forming voltage of 2.2 V (Fig. 3.6a). In this case, the induced $V_O^{\cdot\cdot}$ migrates to the cathode and shows slight segregation in the cathode region, because the drift flux from the anode to the cathode is suppressed due to the decreasing local electrical field (black curve in Fig. 3.6d). On the other hand, high temperature enhances the diffusion flux from the cathode to the anode partially cancels the drift flux. Consequently, a CF with uniform $N_{V_O^{\cdot\cdot}}$ distribution and a much smaller $V_O^{\cdot\cdot}$ depletion gap is formed (snapshot A in Fig. 3.6c and black curve

in Fig. 3.6b). As the $k_{th}(K_2)$ increases, the heat generated by Joule heating effect can be easily dissipated and the local temperature decreases (red curve in Fig. 3.6e), which inhibits the $V_O^{\cdot\cdot}$ generation and increases the CF forming voltage up to 2.49 V (Fig. 3.6a). When k_{th} further increases ($K_2 = 10.5$), the induced $V_O^{\cdot\cdot}$ migration from anode to cathode becomes much easier under a higher local electrical field (blue curve in Fig. 3.6d). Thus, more $V_O^{\cdot\cdot}$ accumulation near the cathode and a larger $V_O^{\cdot\cdot}$ depletion gap near the anode is clearly seen (snapshot C in Fig. 3.6c and blue curve in Fig. 3.6b).

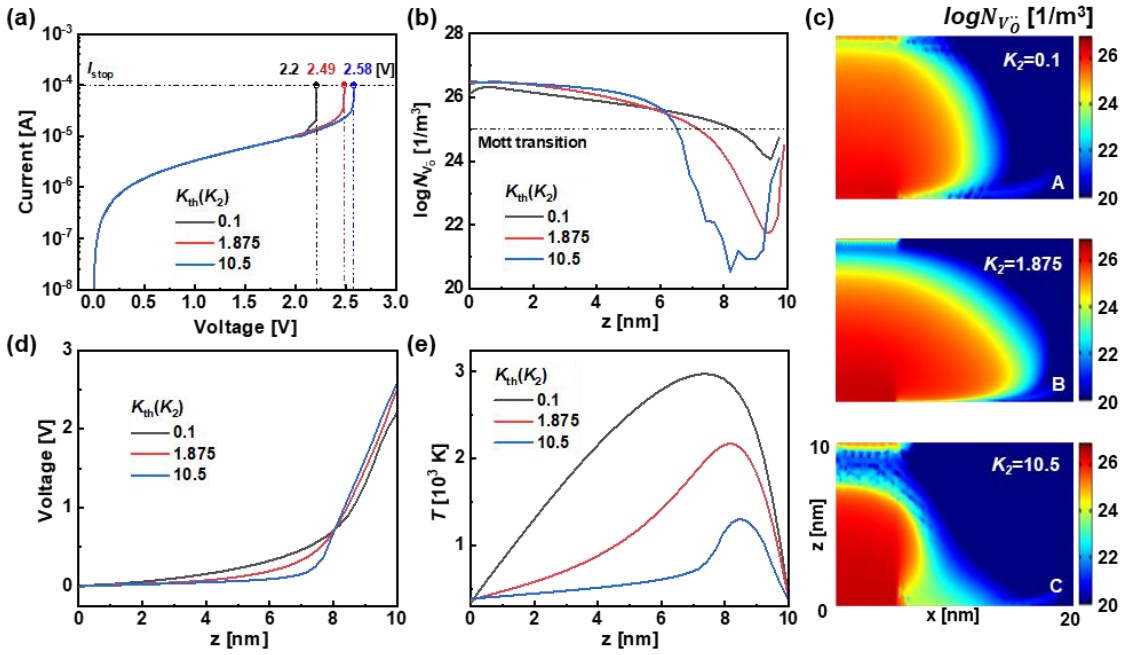

Fig. 3.6. Effect of thermal conductivity on the CF growth. a. Current characteristic with different electrical conductivity (by K_1) under a voltage sweep rate dV/dt=1 V/s. b. $N_{V_O^{\cdot\cdot}}$ ditributions along the center of CF ($x = 0, z =$ 0~10 nm). c. Calculated 2D $N_{V_O^{\cdot\cdot}}$ map. d, e. Calculated 1D profiles of local electrical potential φ and temperature T along the center of CF ($x = 0, z =$ 0~10 nm) at final state.

3.4. Summary

Based on the previous simulations, it is revealed that the CF growth behavior is determined by both the electrode properties (energy barrier of metals to oxidize from oxide E_b) and the physical properties of the oxides (the electrical and thermal conductivity). It is found that employing an active metal electrode accelerates the formation of a CF and improves the homogeneity of the CF concentration. That's why active metals such as Ti and Ta with small vacancy formation barrier (E_b) and large capability to extract oxygen atoms from oxides are widely used as electrode materials[33,117,127]. Lee *et al.* [33] reported a novel HfO_2 based resistive memory with TiN/Ti/HfO_2/TiN stacking layers. Due to the high activity of a Ti layer inserted between the HfO_2 and electrode TiN, a large amount of oxygen can be exchanged between Ti and HfO_2, resulting in the formation of HfO_x (x~1.4) of high oxygen deficiency. Yang *et al.*[128] demonstrated that Ta metal electrode could serve as a large reservoir of mobile oxygen vacancies in Pb/TaO_x/Ta system. In the case when the electrode is blocking for oxygen exchange at the metal/oxide interface, additional oxygen exchange layers (OEL) attached on the electrodes can also potentially improve the $V_O^{\cdot\cdot}$ generation rate[33,127]. Our simulation work manifests that controlling the electrode properties can be used to design and optimize the properties of metal oxide-based RRAMs.

On the other hand, our analysis shows that the interplay between the $V_O^{\cdot\cdot}$ generation rate at the anodic interface and the $V_O^{\cdot\cdot}$ migration rate in the bulk strongly influences the CF growth direction during the electroforming process. When the $V_O^{\cdot\cdot}$ generation rate is much smaller than the $V_O^{\cdot\cdot}$ migration rate in the bulk, a local conductive region is first formed near the cathode where $V_O^{\cdot\cdot}$ are segregated due to the fast migration. Then the CF

continues to grow towards the anode region, when $V_O^{\cdot\cdot}$ diffuse back from the cathode to the anode. When the $V_O^{\cdot\cdot}$ generation rate is larger than the $V_O^{\cdot\cdot}$ migration rate in the bulk, the generated $V_O^{\cdot\cdot}$ at the anode site diffuses and drifts gradually towards the cathode, such that the CF propagates from the anode towards the cathode. Specifically, the filament growth in different directions has been observed and our simulation results are consistent with experimental results[110].

Finally, it is revealed that the increase of electrical conductivity in oxide can generate more heat by Joule heating effect, and can thus enhance the $V_O^{\cdot\cdot}$ generation rate and decrease the forming voltage of the CF. Meanwhile, the increase of thermal conductivity promotes heat dissipation and reduces the $V_O^{\cdot\cdot}$ generation rate, resulting in a higher forming voltage. Higher forming voltage further promotes $V_O^{\cdot\cdot}$ generation at the anodic interface and accelerates the $V_O^{\cdot\cdot}$ drift to the cathode, creating a large $V_O^{\cdot\cdot}$ depletion gap. Based on these studies, we can conclude that choosing metal oxides with high electrical conductivity and lower thermal conductivity helps to improve the uniformity of the CF with homogeneous $V_O^{\cdot\cdot}$ concentration and reduce the electroforming voltage.

Chapter 4. Resistive switching behavior in metal oxide-based RRAM

In Chapter 3, the initial CF formation has been investigated, we know that using an active anode and selecting the metal oxide with higher electrical conductivity and lower thermal conductivity benefits achieve a uniform and homogenous CF. As we know, the resistive switch is attributed to the CF connected and disconnected between electrodes. Therefore, in this section, we would study the subsequent resistive switching behavior once CF formed inside the oxide layer.

4.1. Introduction

Several theoretical/physical models have been used to study the CF switching dynamics during resistance switching, as we summarized in section 2.3. However, most existing models do not take into consideration the impact of mechanical stress during CF evolution[129]. It is found that the internal point defect concentrations can alter the local mechanical strains and electrical potential[130-133]. Recently, chemo-mechanical coupling in nonstoichiometric metal oxides has been studied and is shown to have a strong influence on the properties of many electrical and energy devices such as solid-oxide fuel cells and catalysts[134,135]. Therefore, it is necessary to carefully assess the mechanical effect induced by the defect distribution and transport on the resistance switching behavior of RRAM.

The large current on/off ratio and fast switching speed are the two key characteristics of RRAM. As we summarized in section 2.1.1, many metal oxides can be

used as the switching layer, and plenty of works are reported to investigate the resistive switching behavior in each metal oxide-based RRAM cell. We also need to know how metal oxide properties influence the performance of RRAM and which kind of oxide is an ideal candidate to achieve optimal performance. Finding out general rules through conventional experimental trial-and-error approaches is highly inefficient. Here, we propose to employ a combination of high throughput computation and machine learning to guide the materials discovery and design for RRAM. Such an approach has recently been demonstrated for defective oxides and nanomaterials[136,137]. Shen *et. al.*[138] also employed such a methodology to screen and identify potential oxide nanofillers in polymer-based dielectrics for improved dielectric breakdown strength. Zhang *et. al*.[139] demonstrated an unsupervised approach for discovering new candidates of solid state Li-ion conductors with conductivities of $10^{-4} \sim 10^{-1}$ S cm^{-1} predicted in *ab initio* molecular dynamics simulations.

In this section, we first developed a phase-field model to incorporate the impact of mechanical stress on resistive switching behavior and its interaction with mass diffusion, thermal transport, and electrical conduction dynamics in metal oxide-based RRAM. By parameterizing the three key material constants of metal oxides, i.e., the Vegard strain coefficient (V_{ij}), the electrical conductivity (σ), and the thermal conductivity (k_{th}) to represent different insulating oxide layers in RRAM, we perform high-throughput phase-field simulations to independently and systematically explore each of these intrinsic material constants on the performance of metal oxide-based RRAM and generate a material-property database. Based on this we apply compressed-sensing based machine learning to derive analytical prediction models for the device performance including the current on/off ratio ($I_{\text{on}}/I_{\text{off}}$) and resistance switching time (t_{switch}) of RRAM as a function

of the aforementioned key material constants. These analytical models provide fundamental physical insights for accelerating the future discovery of RRAM materials.

4.2. Model

Phase field model

Compared with Eq. 3-1, the total free energy of the system (F_{total}) considered the synergistic contributions from the chemical, electrical, and mechanical effects, which is written as:

$$F_{total} = \int f_{total}\, dV$$

$$f_{total} = f_{chem} + f_{electric} + f_{elastic} \tag{4-1}$$

where $f_{elastic}$ represents the elastic energy density. The chemical energy density and electric energy density are same with that in Chapter 3,

$$f_{chem} = -k_B T[N_O ln\frac{N_O}{N_O - N_{V_O^{\cdot\cdot}}} + N_{V_O^{\cdot\cdot}} ln\frac{N_O - N_{V_O^{\cdot\cdot}}}{N_{V_O^{\cdot\cdot}}}] \tag{4-2}$$

$$f_{electric} = 2e_0 N_{V_O^{\cdot\cdot}}\varphi - \frac{1}{2}\varepsilon_0\varepsilon_r(\nabla\varphi)^2 \tag{4-3}$$

The elastic energy density is written as[140]:

$$f_{elastic} = \frac{1}{2}C_{ijkl}\left(\varepsilon_{ij} - \varepsilon_{ij}^0\right)\left(\varepsilon_{kl} - \varepsilon_{kl}^0\right) \tag{4-4}$$

where C_{ijkl} is the elastic constant tensor, ε_{ij} is the total strain, and ε_{ij}^0 is the local eigenstrain induced by the variation of oxygen vacancy density. In this model, we assume that $\varepsilon_{ij} = 0$. The local eigenstrain ε_{ij}^0 induced by the variation of oxygen vacancy density is determined based on the converse Vegard's law, which is written as:

$$\varepsilon_{ij}^0 = V_{ij}\Delta N_{V_O^{\cdot\cdot}}\delta_{ij} \tag{4-5}$$

where $V_{ij} = \frac{1}{a} \cdot \frac{da}{dN_{V_O^{\cdot\cdot}}}$ is the Vegard strain coefficient, which describes the lattice parameter (a) change with the oxygen vacancy density ($N_{V_O^{\cdot\cdot}}$), δ_{ij} is the Kronecker operator; $\Delta N_{V_O^{\cdot\cdot}} = (N_{V_O^{\cdot\cdot}} - N_{V_{Oi}^{\cdot\cdot}})$ is the variation of the oxygen vacancy density. The constant value of $N_{V_{Oi}^{\cdot\cdot}}$ is the oxygen vacancy density in the reference stress-free state.

The chemical, electrical and elastic potentials of the system are obtained by taking the variational derivative of the corresponding free energy densities with respect to $N_{V_O^{\cdot\cdot}}$, i.e.,

$$\mu_{V_O^{\cdot\cdot}}^{\text{chem}} = \frac{\delta f_{\text{chem}}}{\delta N_{V_O^{\cdot\cdot}}} = k_B T ln \frac{N_{V_O^{\cdot\cdot}}}{N_O - N_{V_O^{\cdot\cdot}}} \tag{4-6}$$

$$\mu_{V_O^{\cdot\cdot}}^{\text{electric}} = \frac{\delta f_{\text{electric}}}{\delta N_{V_O^{\cdot\cdot}}} = 2e\varphi \tag{4-7}$$

$$\mu_{V_O^{\cdot\cdot}}^{\text{elastic}} = \frac{\delta f_{\text{elastic}}}{\delta N_{V_O^{\cdot\cdot}}} = C_{ijkl}[V_{ij}]^2 \Delta N_{V_O^{\cdot\cdot}} \delta_{ij} \tag{4-8}$$

Thus, the total potential of the system is described as:

$$\mu_{V_O^{\cdot\cdot}} = \mu_{V_O^{\cdot\cdot}}^{\text{chem}} + \mu_{V_O^{\cdot\cdot}}^{\text{electric}} + \mu_{V_O^{\cdot\cdot}}^{\text{elastic}} \tag{4-9}$$

The flux of oxygen vacancy is proportional to the gradient of the potential:

$$J_{V_O^{\cdot\cdot}} = -\frac{D}{k_B T} N_{V_O^{\cdot\cdot}} \nabla \mu_{V_O^{\cdot\cdot}} \tag{4-10}$$

The oxygen vacancy transport process can be described by the Nernst-Planck equation. To investigate the defect-induced mechanical effect on the resistive switching process, we either include or exclude the elastic potential in the Nernst-Planck equation, as shown in Eqs. 4-11 and 4-12,

$$\frac{\partial N_{V_O^{\cdot\cdot}}}{\partial t} = -\nabla \cdot J_{V_O^{\cdot\cdot}} = \nabla \cdot (D \nabla N_{V_O^{\cdot\cdot}} + \frac{eD}{k_B T} N_{V_O^{\cdot\cdot}} \nabla \varphi - \frac{D}{k_B T} C_{ijkl}[V_{ij}]^2 N_{V_O^{\cdot\cdot}} \Delta N_{V_O^{\cdot\cdot}}) \tag{4-11}$$

$$\frac{\partial N_{V_O^{\cdot\cdot}}}{\partial t} = -\nabla \cdot J_{V_O^{\cdot\cdot}} = \nabla \cdot (D\nabla N_{V_O^{\cdot\cdot}} + \frac{eD}{k_B T} N_{V_O^{\cdot\cdot}} \nabla\varphi) \quad (4\text{-}12)$$

Eqs. 4-11 and 4-12 are coupled with the current continuity equation for electrical conduction (Eq. 4-13) and the thermal transport equation for Joule heating (Eq. 4-14),

$$\nabla \cdot \sigma\nabla\varphi = 0 \quad (4\text{-}13)$$

$$-\nabla \cdot k_{th}\nabla T = \sigma|\nabla\varphi|^2 \quad (4\text{-}14)$$

where σ and k_{th} are the electrical and thermal conductivity, respectively. We use same assumption in electroforming process to determine the σ and k_{th} for metal oxide layer, the details can be found in section 3.2.

Eqs. 4-11 to 4-14 are self-consistently solved to obtain the oxygen vacancies density $N_{V_O^{\cdot\cdot}}$, the electrical potential φ and the temperature T using finite element method based on the platform of COMSOL Multi-physics. Fig. 4.1 illustrates the 2D axisymmetric geometry. As the resistive switching depends on the rupture and reconstruction of CF which has been grown during the electroforming process. Therefore, we define a uniform region with a high concentration of $V_O^{\cdot\cdot}$ ($N_{V_O^{\cdot\cdot}} = 1.2\times10^{27}$ m^{-3}) as the pre-existing CF and the remaining insulating region is stoichiometric HfO_2, as shown in Fig. 4.1. Then, the simulation starts with a triangular voltage sweep with rate dV/dt=0.1 V/s applied on the top electrode while the bottom electrode is grounded. The total system size is 35×20 nm^2 and the mesh size is selected as 0.5 nm. In the resistive switching process, the two electrodes are assumed to act as heat sinks with fixed temperature T=300 K. We consider that both electrodes are blocking the oxygen transfer, i.e., there is no oxygen vacancy flux at the interfaces between the oxide layer and the electrodes. The boundary conditions are list as,

$$J_{V_O^{\cdot\cdot}}\Big|_{z=0} = J_{V_O^{\cdot\cdot}}\Big|_{z=20\text{nm}} = 0 \ \frac{1}{\text{m}^2\text{s}}$$

$$T\Big|_{\text{all boundaries}} = 300 \text{ K}$$

$$\varphi\Big|_{z=0} = 0 \text{ V}, \ \varphi\Big|_{z=20\text{nm}} = V_{\text{app}} \text{ V}$$

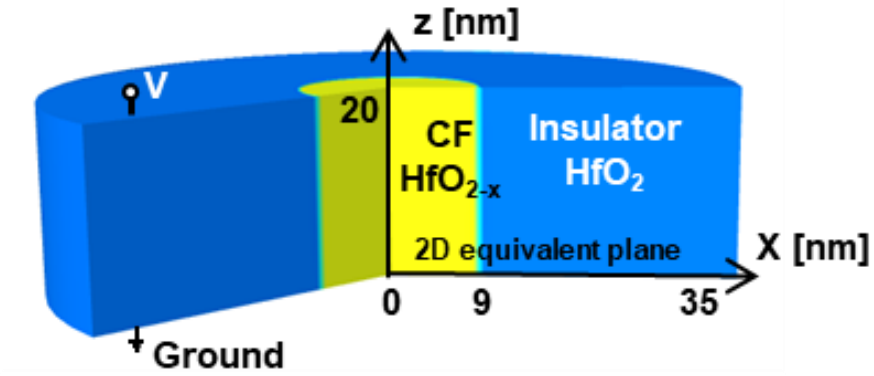

Fig. 4.1 Simulation size and geometry.

DFT calculations of Vegard strain coefficient

We employ the density functional theory calculations of monoclinic ($P2_1/c$) HfO_2 phase by using the Vienna Ab initio Simulation Package (VASP) with PAW atomic potentials[63,141] to calculate the Vegard strain coefficient. Based on the earlier electronic-structure calculations[142], it was determined to use the generalized gradient approximation (GGA) with the Perdew-Burke-Ernzerhof (PBE)[143] functional and an additional Hubbard 'U' potential of 2.2eV applied to the '*f*' orbitals of Hafnia flavor for treating the on-site Coulomb interaction, following the Dudarev's rotationally invariant approach[76].

To obtain the Vegard strain at high concentrations of ~8.3% (one oxygen-vacancy in a 12-atom unit cell), the DFT calculations were calculated with a 6×6×6 Gamma-

centered **k**-mesh to integrate the Brillion Zone with the atomic forces relaxed by using a conjugate-gradient algorithm till the forces on all atoms converged to at least 0.01 eV/Å. On the other hand, to obtain the Vegard strain at low concentrations, a 3×3×3 supercell was used to perform oxygen defect cluster calculations. A single **k**-point (the Gamma point) was used to integrate the Brillion Zone and the atomic forces converged down to 0.1 eV/Å with concomitant relaxation of lattice parameters. At the same time, the lattice parameters were simultaneously optimized to obtain the zero-pressure volume with and without oxygen vacancy.

Machine learning approach

Three material properties of metal oxides including Vegard strain coefficient V_{ij}, electrical conductivity σ, and thermal conductivity k_{th} are selected as the material fingerprints to identify the properties of metal oxides-based RRAM ($I_{\text{on}}/I_{\text{off}}$ as well as the t_{switch}). For building an interpretable machine learning features space, we start with a set of features Φ_0 (V_{ij}, σ, k_{th}) as the primary features where V_{ij} is dimensionless, σ is in units of 10^3 S cm^{-1} and k_{th} is in units of W m^{-1}K^{-1}. Then, additional features are constructed by using operators in the set $H^m \equiv (+, -, \times, /, \exp, \log, ^{\wedge}\text{-}1, ^{\wedge}2, ^{\wedge}3, \text{sqrt}, \text{cbrt}, |-|)$, where the superscript 'm' indicates that dimensional analysis is performed only for meaningful combinations (i.e., physically allowed combinations). Thus, the feature space has been extended by using a combination of H^m operators with a 3-rungs operation (i.e., $\Phi_0 \rightarrow \Phi_1 \rightarrow \Phi_2 \rightarrow \Phi_3$). The number of elements in Φ_1, Φ_2, Φ_3 is ~27, ~619 and ~448330, respectively. Since some of the properties could be correlated, such as the electrical conductivity (σ) and thermal conductivity (k_{th})) related via the Lorenz factor based on the

Wiedemann-Franz law, we use the recently developed by Sure Independence Screening and Sparsity Operator (SISSO) approach[144] to identify a descriptor that predicts the memristor properties. SIS allows dimensional reduction of the size of the feature space, while SO is used to pinpoint the optimal *n*-dimensional descriptor[145,146]. To obtain a more predictable machine learning model, we excluded very few discrete data points with $I_{\text{on}}/I_{\text{off}} > 10$. A total of 1835 sets of phase-field simulations with different combinations of (V_{ij}, σ, k_{th}) are performed to obtain the training dataset.

4.3. Results and discussion

4.3.1. Resistive switching behavior

The simulation results of resistive switching dynamics in HfO_2 metal oxide with a pre-existing CF is shown in Fig. 4.2. A hysteresis-like current-voltage behavior is clearly seen, indicating the bipolar resistive switching characteristics, as illustrated in Fig. 4.2a. The resistance starts to increase when the voltage increases to 0.4 V which is referred to as reset voltage, and the device switches from LRS to HRS. The resistance would be recovered as the application of negative voltage, which is known as set transition, and the switching of the device occurs at -0.57 V (set voltage) from HRS to LRS. As shown in Fig. 4.2b, the measured *I-V* curve also shows an abrupt transition at -0.55 V and a gradual change of resistance occurring from 0.4V. The simulation results agree well with experimental measurements[7] and theoretical calculations[78] of HfO_2 based memristor device[7], indicating that the current phase-field model is able to capture the resistive switching behavior in metal oxide-based RRAM.

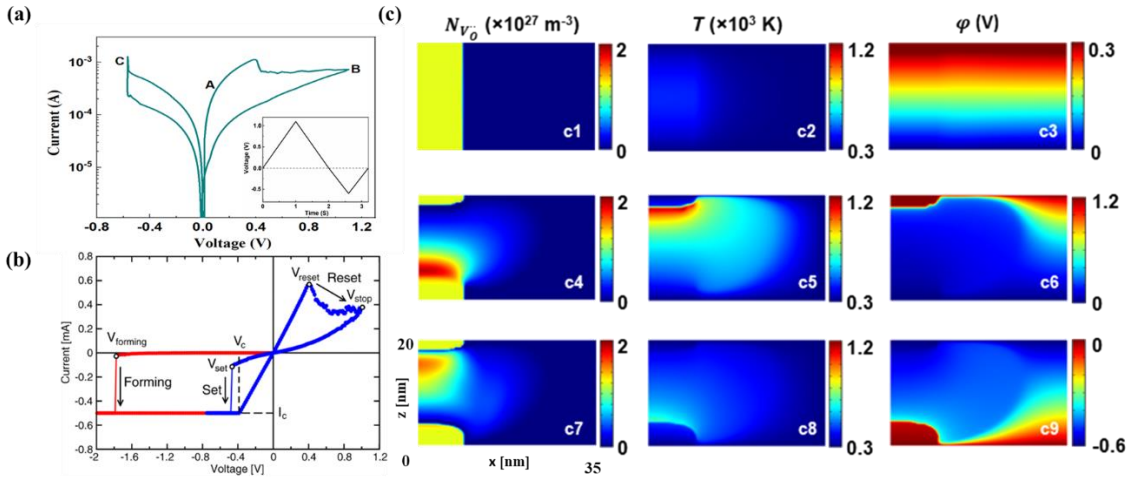

Fig. 4.2. Phase-field simulation of resistive switching dynamics in HfO_2 metal oxide. a. Current-voltage (I-V) hysteresis behavior. The inset in a show the applied triangular voltage sweep with rate dV/dt=0.1 V/s. b. The measured current-voltage for the bipolar RRAM device with TiN-HfO_x-TiN structure[7]. c. The simulated 2D spatial profiles of $N_{V_O^{\cdot\cdot}}$, T and φ at different applied voltages on top electrode: (c1-c3) V_{app} = 0.3 V initial state; (c4-c6) V_{app} = 1.1 V reset state; and (c7-c9) V_{app} = -0.57 V set state, corresponding to state A, B, C in (a) respectively. The scale bar in c7 applies to c1-c9.

To further understand the physical nature of the resistive switching between HRS and LRS under reset and set processes, the evolutions of the oxygen vacancies $N_{V_O^{\cdot\cdot}}$, temperature T and electric potential φ have been mapped, as shown in Fig. 4.2c. During the reset process, $V_O^{\cdot\cdot}$ migrates to the BE and forms a local $V_O^{\cdot\cdot}$ deficiency gap along the CF (Fig. 4.2c4), therefore, the resistance increases with the increasing applied voltage. Meanwhile, the local electric field is enhanced due to the low conductivity of the gap region (Fig. 4.2c6) and the temperature is increased due to the Joule heating effect (Fig. 4.2c5). During the set process, the gap formed by the reset process is filled via the $V_O^{\cdot\cdot}$ migration towards TE under negatively applied voltage, accompanied by the decrease of local temperature along the CF. The reconnection of the CF allows for a reduction of the overall resistance of the device. It is also seen that an additional $V_O^{\cdot\cdot}$ depletion region is formed

near the BE during the set process, as depicted in Fig. 4.2c7. This is because the BE is unable to provide sufficient $V_O^{\cdot\cdot}$ continuously. In this case, a relatively higher overall resistance after the set process is induced compared with the initial value.

4.3.2. Mechanical strain effect in RRAM

In metal oxide-based RRAM, the oxygen vacancy concentration in the CF region can reach up to ~10^{27} m^{-3}. This creates a lattice shrinkage strain of up to 1%, which could influence the vacancy transport and the resistance switching dynamics. Here, we study the effect of $V_O^{\cdot\cdot}$ induced local strain on resistive switching behavior. The local strain ε_{ij}^0 induced by the change of $V_O^{\cdot\cdot}$ density can be calculated by $\varepsilon_{ij}^0 = V_{ij}\Delta N_{V_O^{\cdot\cdot}}\delta_{ij}$, where V_{ij} is the Vegard strain coefficient or chemical expansion coefficient, δ_{ij} is the Kronecker operator, $\Delta N_{V_O^{\cdot\cdot}} = (N_{V_O^{\cdot\cdot}} - N_{V_{Oi}^{\cdot\cdot}})$ is the variation of oxygen vacancy density. The constant value $N_{V_{Oi}^{\cdot\cdot}}$ is the $V_O^{\cdot\cdot}$ density in the reference stress-free state. In this simulation work, the initial electroforming state is chosen as the reference stress-free state. This mechanical strain causes an additional elastic driving force for the $V_O^{\cdot\cdot}$ migration based on Eq. 4-8. We assume V_{ij} to be -0.064 based on our density functional theory (DFT) calculations, benchmarked to more accurate many-body theory-based methods[142], indicating that the oxygen vacancy will create a lattice shrinkage in HfO_2.

The calculated strain distribution at the end of the reset process under 1.1 V applied voltage is shown in Fig. 4.3a. Under the reset process, the $V_O^{\cdot\cdot}$ migrates towards the BE causing a local tensile strain up to 0.5% in the $V_O^{\cdot\cdot}$-rich region near BE (blue region), and a local compressive strain in the gap region where $V_O^{\cdot\cdot}$ deplete (red region). Meanwhile, a tensile strain is also seen aside from the CF due to the lateral diffusion of oxygen vacancies.

This inhomogeneous strain creates strain gradients ($d\varepsilon_{ij}^{0}/dz$ and $d\varepsilon_{ij}^{0}/dx$) along both vertical and lateral directions, which act as an additional driving force for oxygen vacancy transport. We compare the elastic (μ_{elastic}), electrical (μ_{electric}), and chemical potentials (μ_{chem}) for the initial electroforming state, the intermediate state, and the final reset state as shown in Fig. 4.3b. It should be noted that the μ_{elastic} is homogeneous in the initial state and becomes higher/lower near the BE/TE during the reset process (Fig. 4.3 b1, b4, b6). We can also find that the electrical potential μ_{electric} is reduced near BE and enhanced in TE (Fig. 4.3b3, b6, b9). That means the elastic effect counterbalances the electrical effect, during the reset process. Meanwhile, the μ_{elastic} map (Fig.4.3 b4, b6) also induces an additional lateral elastic potentials gradient which promotes the lateral diffusion of oxygen vacancies. To clearly understand the interactions among chemical, electrical, and elastic potential, we plot the 1D profiles of each of the energy potentials along the *z* direction across the center of the CF at the end of the reset process, as shown in Fig. 4.3c. At *z* = 17 nm (gap region), the chemical, electrical and elastic potentials all exhibit significant positive gradients, among which the electrical potential shows the largest drop (~ 10^5 J mol^{-1}), acting as the major driving force for the ion migration from TE to BE which makes a gap nearby the TE. On the other hand, at *z* = 5~15 nm, the electric potential gradually increases, while the chemical and elastic potentials decrease. The negative elastic potential gradient offsets the positive electrical potential gradient in this region indicating the $V_O^{\cdot\cdot}$ induced elastic potential partially inhibits the $V_O^{\cdot\cdot}$ drift to BE driven by the electrical field.

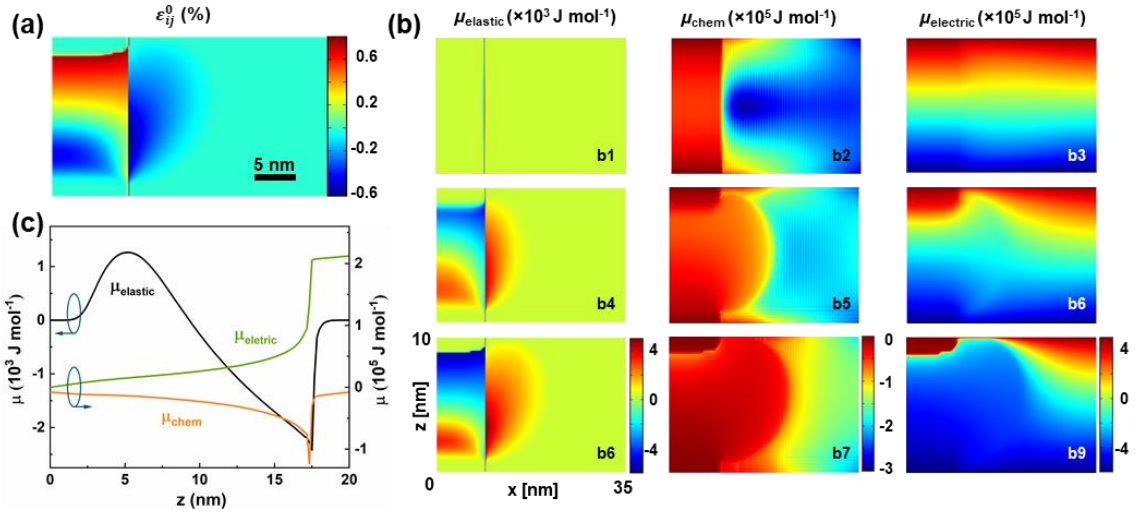

Fig. 4.3 Calculated $V_O^{\cdot\cdot}$ -induced mechanical strain. a. 2D map of the oxygen vacancy induced elastic strain in reset state, b.2D spatial profiles of μ_{elastic}, μ_{chem} and μ_{electric} with a constant applied voltages 1.1 V on top electrode at different states during reset process from 10 ps to 10 us: (b1-b3) 10^{-11} s initial state, (b4-b6) 10^{-8} s intermediate state, and (b6-b9) 10^{-5} s reset state. The scale bar in (b6) applies to (b1-b9), c. 1D profiles of the elastic, electrical and chemical potential along the center of CF (x = 0, z = 0~20 nm).

The mechanical effect on the CF properties and the performance of the HfO_2 switch cell are also investigated. The elastic potential inhibits the vertical $V_O^{\cdot\cdot}$ migration in the CF and promotes the lateral migration of $V_O^{\cdot\cdot}$ into the insulating region. This results in a relaxation of $V_O^{\cdot\cdot}$ segregation inside the CF near the BE (Fig. 4.4a), as compared to the case when μ_{elastic} is not taken into consideration (Fig. 4.4b). The details can be illustrated by the comparison of 1D profiles of $N_{V_O^{\cdot\cdot}}$ with and without considering μ_{elastic}, along both vertical and horizontal directions (Fig. 4.4c). The effect of mechanical strain on the temporal evolution of the overall resistance of the entire simulation system under a constant voltage pulse of 1.1 V with pulse width from 10 ps to 10 us during the reset process is shown in Fig. 4.4d. The initial resistance/current is R_{on} ~ 0.335 kΩ (or I_{on} ~ 3 mA) and increases with time. The final resistance in the current off state considering the mechanical effect is calculated to be R_{off} = 0.969 kΩ, which is nearly 12% lower than that without

considering the mechanical effect (1.1 kΩ). This causes a decrease of the current on/off ratio (I_{on}/I_{off}) from 3.28 to 2.89, and a slight increase in the resistive switching time (t_{switch}) from 18 to 23 ns (here t_{switch} is defined when the cell resistance increases by more than 50% from its initial value). This is because the elastic potential inhibits the $V_O^{\cdot\cdot}$ transport and local segregation, resulting in a long time for the CF fracture and a reduction in the R_{off} value.

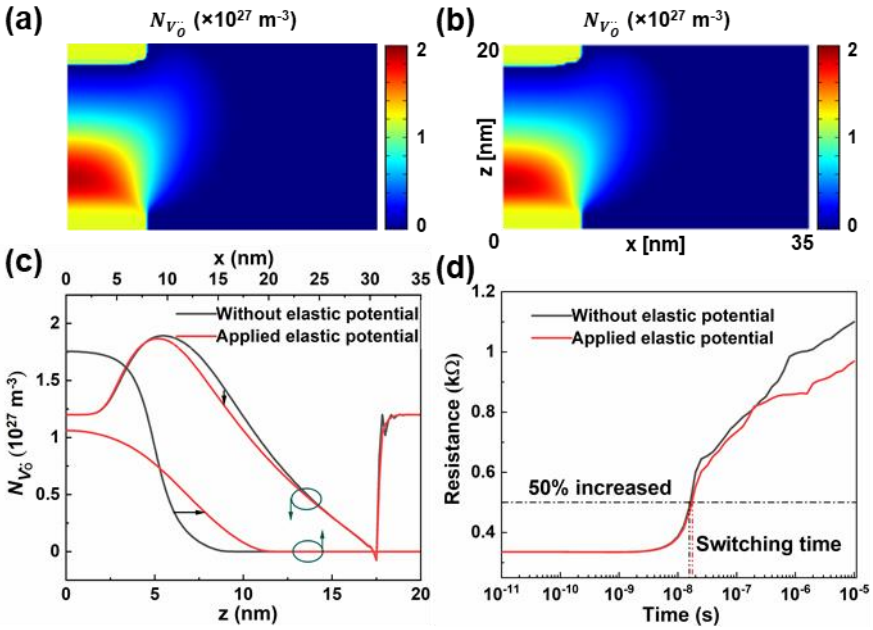

Fig. 4.4 Effect of $V_O^{\cdot\cdot}$-induced mechanical strain on resistive switching behavior. a, b. 2D maps of oxygen vacancy density $N_{V_O^{\cdot\cdot}}$ without and with coupling the mechanical effect during reset process, c. comparison of 1D profiles of $N_{V_O^{\cdot\cdot}}$ along the center of the CF (x = 0, z =0~20 nm) and the cylindrical direction (z = 10 nm, x = 0~35 nm) with and without coupling the mechanical effect, d. the evolution of total resistance under a constant applied voltage of 1.1 V during reset process. The switching time (t_{switch}) is defined by a 50% increase with respect to the initial resistance value. The scale bar in a applies to b.

4.3.3. Effect of metal oxide properties on the performance of memristor

From previous studies, the performances of switch cell (I_{on}/I_{off} and t_{switch}) are heavily dependent on $V_O^{\cdot\cdot}$ transport driven by the combined chemical, electrical, thermal,

and elastic effects. These effects scale with their relevant kinetic coefficients, such as the σ and k_{th} of the insulating metal oxides and their corresponding metallic states (of high oxygen deficiency), and the Vegard strain coefficients V_{ij}. While V_{ij} is assumed to be a constant, σ and k_{th} are spatially dependent on the local $V_O^{\cdot\cdot}$ density. This significantly increases the complexity of the vacancy transport dynamics and the resistive switching behavior. To untangle all these couplings and understand their independent roles in resistive switching, we performed systematic phase-field simulations by tuning one of the aforementioned three material constants while fixing the other two.

Fig. 4.5 shows the temporal evolutions of the overall resistance and the dependence of $I_{\text{on}}/I_{\text{off}}$ on V_{ij}. The initial resistance (ON state) remains constant for all V_{ij}'s, while the final resistance (off state) decreases with increasing V_{ij}, as shown in Fig. 4.5a, resulting in a decreasing $I_{\text{on}}/I_{\text{off}}$ with increasing V_{ij} (Fig. 4.5b). This agrees with the previous study that the additional mechanical driving force tends to reduce the current on/off ratio.

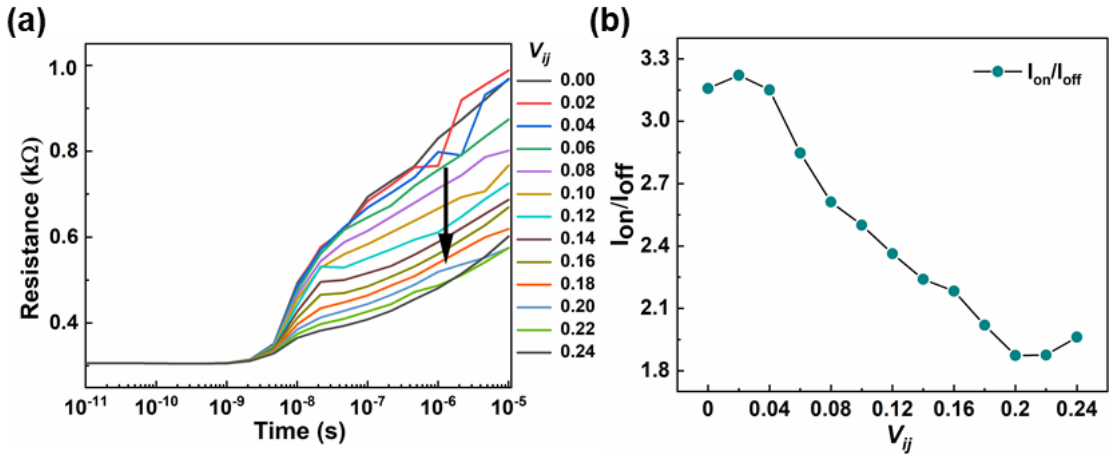

Fig. 4.5 Effects of material parameter_Vergard strain coefficient on the device performance. A Temporal evolution of overall resistance with different Vegard strain coefficient V_{ij}, b dependence of current on/off ratio $I_{\text{on}}/I_{\text{off}}$ on V_{ij}.

The effect of electrical conductivity σ (by its slope K_1) on the overall resistance is shown in Fig. 4.6. The initial resistance decreases with increasing K_1, while the final resistance experiences a decrease-increase-decrease behavior. This results in a peak value of $I_{on}/I_{off} \sim 15$ at $K_1 = 7.5$ shown in Fig. 4.6a and b. The $N_{V_O^{\cdot\cdot}}$, T and φ distributions under three typical electrical conductivities corresponding to $K_1 = 0.5$, 7.5 and 15 are plotted in Fig. 4.6c. It can be observed that no evident $V_O^{\cdot\cdot}$ depletion gap is formed inside the CF (Fig. 4.6c1), and no resistive switching occurs and I_{on}/I_{off} remains low value, under low electrical conductivity ($K_1 = 0.5$). That is because, when electrical conductivity is small, it cannot generate much heat (Fig. 4.6c2) causing the low mobility of $V_O^{\cdot\cdot}$ transport based on Eq. 4-11, so that the $V_O^{\cdot\cdot}$ are not able to migrate to BE. That means a higher voltage needs to be applied to reset the device. As σ increases ($K_1 = 7.5$), the more generated heat by Joule heating effect is found in Fig. 4.6c5. The enhanced temperature promotes the mobility of $V_O^{\cdot\cdot}$, and a wide gap is formed inside the CF by the $V_O^{\cdot\cdot}$ migration (Fig. 4.6c4), causing a significant increase in the resistance of the final reset state as well as I_{on}/I_{off} increase (Fig. 4.6b). However, when $K_1 = 15$, much heat generation (Fig. 4.6c8) gives rise to a significant $V_O^{\cdot\cdot}$ transport in the lateral direction to the entire system and reduces the local $V_O^{\cdot\cdot}$ segregation/depletion inside the CF, as shown in Fig. 4.6c7. Thus, the CF gap disappears and I_{on}/I_{off} reduces with increasing electrical conductivity.

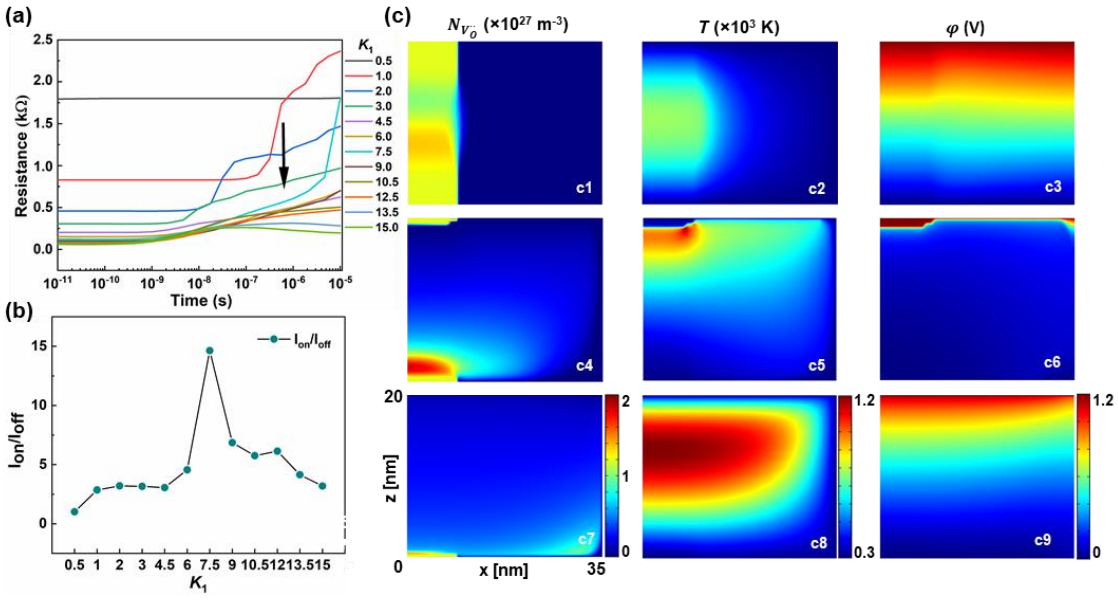

Fig. 4.6 Effects of material parameter_electrical conductivity on the device performance. a Temporal evolution of overall resistance with different electrical conductivity (by K_1), b Dependence of current on/off ratio I_{on}/I_{off} on K_1, c 2D maps of $N_{V_O^{\cdot\cdot}}$, T and φ: c1-c3 K_1 = 0.5, c4-c6 K_1 = 7.5, c7-c9 K_1 = 15. The scale bar in c7 applies to c1-c9. The results are calculated by increasing the electric conductivity (by K_1) of metal oxides with zero Vegard strain ($V_{ij} = 0$) and fixed thermal conductivity (K_2 = 1.5).

Finally, the effect of thermal conductivity k_{th} (by its slope K_2) on the switching behavior is shown in Fig. 4.7. It is seen that the initial resistance of RRAM remains the same, while the final resistance in the reset state decreases with increasing k_{th}, resulting in a monotonous decrease of I_{on}/I_{off}. Lower k_{th} favors the formation of larger $V_O^{\cdot\cdot}$ depletion gap (Fig. 4.7c1, c4, c7), giving rise to a higher I_{on}/I_{off} (Fig. 4.7b). That is due to low k_{th} prefer to generate much heat that accelerates the $V_O^{\cdot\cdot}$ migration along the electrical field direction. Higher k_{th} partially inhibits the vertical transport of the $V_O^{\cdot\cdot}$. When k_{th} reaches a very high value, the heat generated by Joule heating can easily dissipate through the CF (Fig. 4.7c8). The reduction of the thermal mobility of $V_O^{\cdot\cdot}$ increases the difficulty of the

gap formation along the CF, resulting in the decrease of I_{on}/I_{off}. When $K_2 > 0.8$, I_{on}/I_{off} is around 1.0 indicating that resistive switching no longer occurs.

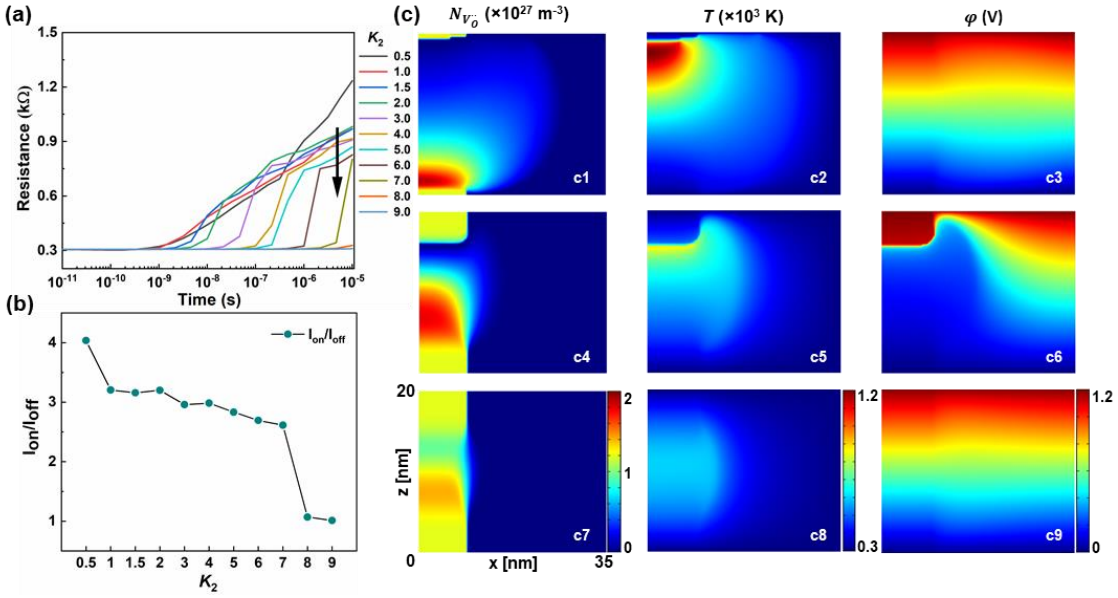

Fig. 4.7 Effects of material parameter_thermal conductivity on the device performance. a Temporal evolution of overall resistance with different thermal conductivity (by K_2), b Dependence of current on/off ratio I_{on}/I_{off} on K_2, c 2D maps of $N_{V_O^{\cdot\cdot}}$, T and φ: c1-c3 K_2 = 1.5, c4-c6 K_2 = 4, c7-c9 K_2 = 9. The scale bar in c7 applies to c1-c9. The results are calculated by increasing the thermal conductivity (by K_2) of metal oxides with zero Vegard strain ($V_{ij} = 0$) and fixed electrical conductivity (K_1 = 3).

4.3.4. High-throughput phase-field simulations and machine learning (ML)

We performed high-throughput phase-field simulations by parameterizing V_{ij}, K_1, and K_2 to calculate the corresponding I_{on}/I_{off} and t_{switch}, and establish a "material constant-resistive switching property" database in metal oxides-based RRAM. The ranges of V_{ij}, σ and k_{th} are chosen to be 0 ~ 0.24 (in absolute value $|V_{ij}|$), 0.06 ~ 18 (10^3 S cm^{-1}), and 6.5 ~ 120.5 (W m^{-1}K^{-1}), respectively, which include most of the metal oxides used in RRAM.

The calculated database is shown in Fig. 4.8a and b. It is clearly seen that most I_{on}/I_{off} ratios are in the range of 1~10, with a few exceptions reaching up to 20. To clearly identify the trend from the 3D database, we plotted the 2D mapped I_{on}/I_{off} and t_{switch} as a function of two out of the three materials parameters with a fixed remaining parameter (Fig. 4.8c-f). These results indicate that the electrical and thermal conductivities play dominant roles over the Vegard strain coefficient during resistive switching in metal oxide materials (Fig. 4.8c-e). It is clearly seen that higher σ and lower k_{th} give rise to higher I_{on}/I_{off} and smaller t_{switch} (or faster switching), as marked by the black circle shown in Fig. 4.8e and h. Several data points marked with colored solid symbols in Fig. 4.8e represent the metal oxides of VO_2, Ta_2O_5, SnO_2, NiO, and HfO_2, respectively, which are commonly used as switching layer in metal oxide-based RRAM[8,10]. It shows that the performance of metal oxide-based RRAM employed with these materials is not optimal. To further improve the performance of metal oxide-based RRAM, increasing the electrical conductivity and decreasing thermal conductivity, as well as avoiding large Vegard strain is necessary.

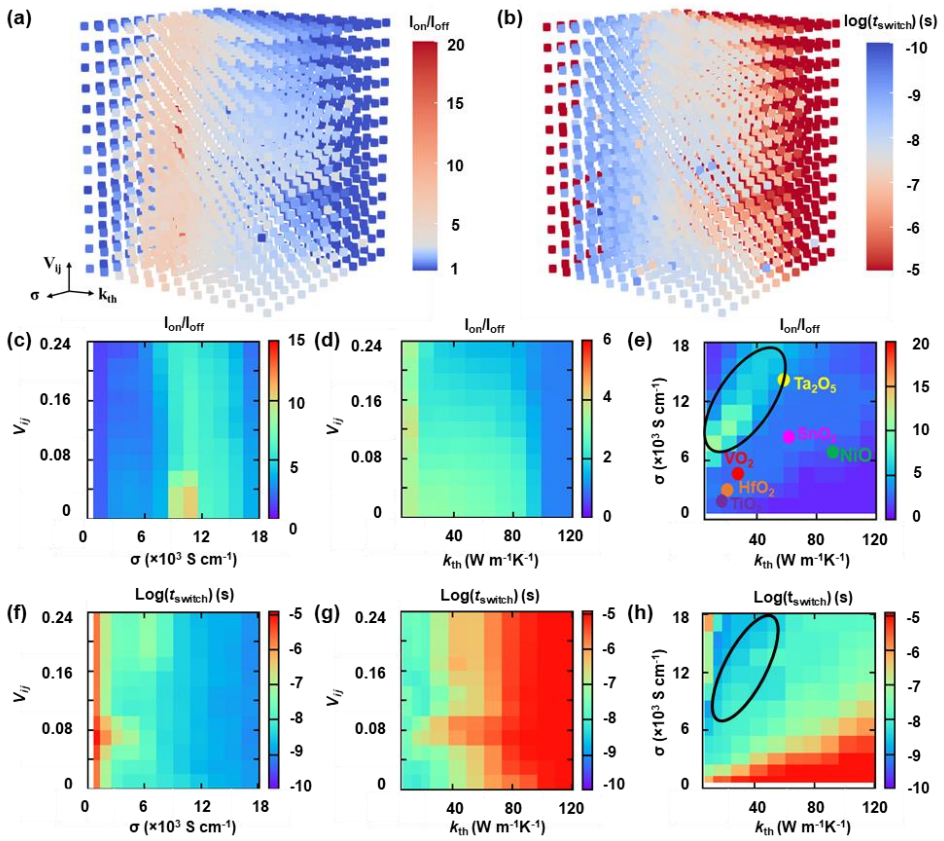

Fig. 4.8 High-throughput phase-field simulations. a. The current on/off ratios (I_{on}/I_{off}) and b the resistive switching time (t_{switch}) for metal oxides-based RRAM by parameterizing the three characteristic materials constants, i.e., the Vegard strain coefficient (V_{ij}), electrical conductivity (σ) and thermal conductivity (k_{th}). 2D mapped c-e I_{on}/I_{off} and f-h t_{switch} as a function of two out of the three materials parameters (V_{ij}, σ, k_{th}) at a fixed remaining parameter.

Based on the database from high-throughput simulations, a recently developed compressed-sensing based machine learning (ML) approach[66] is employed to further elucidate the correlation between (V_{ij}, σ, k_{th}) and (I_{on}/I_{off}, t_{switch}). First, linear correlations among V_{ij}, σ, k_{th}, I_{on}/I_{off}, t_{switch} were investigated using the Pearson correlation coefficient, as shown in Fig. 4.9a. Clearly, σ positively correlates with I_{on}/I_{off}, but negatively correlates with t_{switch}, indicating that I_{on}/I_{off} (t_{switch}) increases (decreases) with increasing σ. Meanwhile, k_{th} exhibits negative (positive) correlations I_{on}/I_{off} (t_{switch}).

These results agree with our previous calculations. Finally, V_{ij} shows a slight negative correlation with I_{on}/I_{off}, and almost no correlation with t_{switch}, indicating that V_{ij} bearly influences t_{switch}. We choose the Vegard strain coefficient V_{ij}, electrical conductivity σ (10^3 S cm^{-1}), and thermal conductivity k_{th} (W m^{-1}K^{-1}) of metal oxides as the fingerprints to build an interpretable machine learning model. We use the Sure Independence Screening and Sparsity Operator (SISSO) approach[144], to predict I_{on}/I_{off} as well as t_{switch}. The training error root-mean-squared-error (RMSE) is used as the criterion to select the suitable *n*D-descriptors. After performing machine learning on the training datasets, 2D-descriptor based predictive expressions of I_{on}/I_{off} with RMSE=0.453 and t_{switch} with RMSE=0.385 were found to be optimal (i.e., with relatively low RMSE and high interpretability), as shown in Eq. 4-15 and 4-16.

$$\log(t_{switch}) = -8.777 + \frac{k_{th}}{\sigma}\left[0.197\exp(V_{ij}) - 0.00354\left(\frac{k_{th}}{\sigma}\right)\right] \quad (4\text{-}15)$$

$$\frac{I_{on}}{I_{off}} = -0.597 - 7.676\left(\frac{\sigma}{k_{th}}\right) + 12.637\left(\sqrt{\frac{\sigma}{k_{th}}}\right) \quad (4\text{-}16)$$

Fig. 4.9b and c show the comparisons of t_{switch} and I_{on}/I_{off} calculated from the phase-field simulation and predicted from the machine learning model. It is seen that the training datasets are clustered near the orange straight line where the phase-field calculated and machine learning predicted properties are equal. In addition, six testing data points of NiO, TiO_2, SnO_2, VO_2, HfO_2, and Ta_2O_5 are also plotted in Fig. 4.9b and c (with solid-colored symbols). All these six data points are located around the solid orange lines, which further validates our machine learning as a predictive model. It should be noted that none of these six data points is used as training datasets.

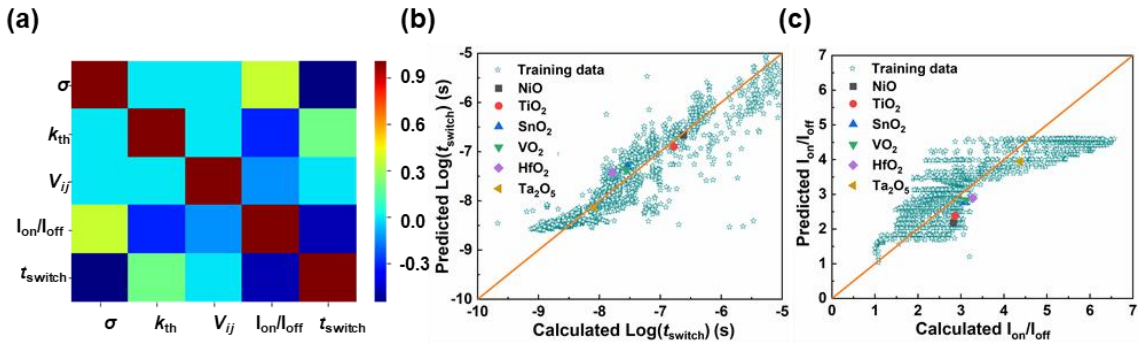

Fig. 4.9 Machine learning results. a. The Pearson correlation plot between the different material-characteristics and the performance metrics. The SISSO model fits to the data using a 2D-descriptor for b t_{switch} and c $I_{\text{on}}/I_{\text{off}}$.

From Eq. 4-15, by choosing V_{ij} = 0 ~ 0.24 which covers most metal oxide, log (t_{switch}) monotonously increases with increasing $\frac{k_{th}}{\sigma}$ ($\frac{\text{W m}^{-1}\text{K}^{-1}}{10^3\ \text{S cm}^{-1}}$) from 0.5 to 25, a range where resistive switching occurs. Fig. 4.10 plots Eq. 4-15 and Eq. 4-16 with the function of $\frac{k_{th}}{\sigma}$. We can see that increasing V_{ij} (magnitude only) results in increasing t_{switch} at given $\frac{k_{th}}{\sigma}$. $I_{\text{on}}/I_{\text{off}}$ gradually decreases with increasing $\frac{k_{th}}{\sigma}$. At very small $\frac{k_{th}}{\sigma}$(<2), $I_{\text{on}}/I_{\text{off}}$ increases with increasing $\frac{k_{th}}{\sigma}$.

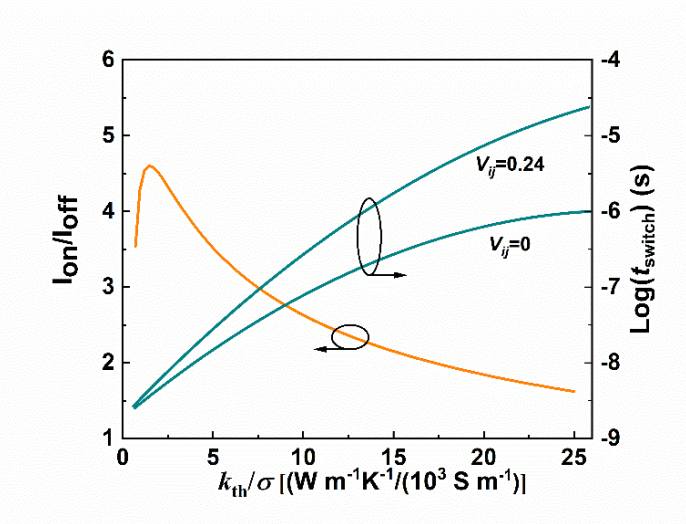

Fig. 4.10 Plot of machine learning predicted equations as a function of k_{th}/σ for I_{on}/I_{off} and t_{switch} with $V_{ij} = 0$ and $V_{ij} = 0.24$.

From the predicted machine learning expressions, it is clearly seen that the properties of the memristor can be enhanced by decreasing $\frac{k_{th}}{\sigma}$. According to the Wiedemann–Franz law, for nearly-free electron metals (and oxide metals), the ratio of the electronic contribution of the thermal conductivity (k_{th}) to the electrical conductivity (σ) of a pure metal is proportional to the temperature (T), i.e., $\frac{k_{\mathrm{th}}}{\sigma} \sim LT$, where L is the Lorenz number. Theoretically, $\frac{k_{\mathrm{th}}}{\sigma}$ has approximately the same value for different pure metals at the same temperature. But for binary transition-metal oxides, the strong electron-electron correlations have been shown to drastically lower the Lorenz number (L) by several orders of magnitude[147,148], due to an anomalously low electronic thermal conductivity. Therefore, Lorenz number would be at lower values for metal oxides with stronger electron-electron correlations at given temperatures. In short, a key design principle for future materials discovery and design to achieve optimally performing

memristor materials would be to select oxides with a relatively low Lorenz number at the same temperature, such as those with strong electron-electron correlations.

4.4. Summary

In summary, a comprehensive computational model based on fundamental thermodynamics and kinetics, including the ion and thermal transport, electrical conduction, and mechanical strain effect is developed to investigate the resistance switching process in metal oxide-based RRAM. It can successfully capture the resistive switching process. The local oxygen vacancy distribution induces a lattice expansion strain and a strain gradient, which act as an additional driving force that inhibits the $V_O^{\cdot\cdot}$ migration in the conductive filament and reduces the current on/off ratios. High-throughput phase-field simulations are performed to construct a "materials fingerprints - targeted performance" database, and machine learning approaches are employed to establish interpretable analytical predictive expressions for $I_{\text{on}}/I_{\text{off}}$ and t_{switch} of memristor in different metal oxides. The machine learning model is further verified by additional phase-field calculations of real metal oxides. This high-throughput/machine-learning approach reveals that metal oxides with relatively small $\frac{k_{th}}{\sigma}$ ratios, found in bad-metals with a low Lorenz number, yield high memristor performance, thereby establishing a key materials-design principle for designing new memristor materials by relating device performance metrics to fundamental material constants. This work thus establishes a strategy to select the metal oxides to optimize the performance and provide guidance to experimentalists in designing high performance metal oxide-based RRAM devices.

Chapter 5. Effect of embedded metallic nano-islands on the Resistive switching behavior in embedded metal oxide RRAMs.

5.1. Introduction

Switching uniformity is extremely important to the application of a large-scale RRAM array since a control unit will need to be programmed in advance to make sure that the input voltage and the probe current corresponding to a specific resistance state are uniform during multiple cycles or devices. However, due to the random growth and rupture of CFs, there are great variations between cycle-to-cycle and device-to-device in Forming, Reset and Set voltages, resistance states, and current ON/OFF ratio. In most metal oxide RRAMs, the stochasticity CF mainly stems from two major reasons: (a) the roughness of electrode/oxide interface [149-152], and (b) the variable chemical properties of the complicated microstructure of metal oxide layer [153,154]. Extensive experimental studies have been made to understand the stochasticity in RRAMs. For example, Nandi *et al*. [149] investigated the effect of roughness of electrodes on the electroforming in the HfO_2 memristor. They found that the roughness increases the variability of CF position and composition. On the other hand, disorder structures such as grain boundaries and defect clusters show various properties which strongly affect the electroforming process [154,155]. Consequently, the randomness of the formation and dissolution of the CFs eventually induces large temporal variations from cycle to cycle and spatial variation from device cell to cell in the set/reset operation voltage and resistance of HRS (R_{off}) and LRS (R_{on}) [156,157]. The uncertainty,

instability, and non-uniformity of CFs based RRAMs have become the most critical challenge that inhibits the applications of RRAM in large scale memory storage and neuromorphic computing [158,159]. Therefore, to improve the uniformity and stability of the RRAM devices, effectively controlling the CF formation and rupture is of key importance.

To address the variability of the RRAM devices, many methods have been proposed, and especially the strategies of filament control including the electrode modifications [34,160-163] and the switching layer optimizations [162-168] have achieved favorable results. For example, through simple electrode engineering, device-to-device uniformity can be effectively enhanced. It has been reported that fabricating an electrode with pyramid tips rather than a flattened electrode with random roughness could lower the operation voltages and improve the uniformity of RRAM devices[169-171]. On the other hand, optimization of the switching layer by doping nanoparticles to obtain stable high CFs is also a feasible method to effectively improve the performance of RRAM devices [167,168]. For example, Lee *et al*. [172] reported that the current ON/OFF ratio and uniformity were enhanced by dispersing Pt nanoparticles into a TiO_2 thin film memristor. Although the electrode engineering and doping nanoparticles can improve the performance of the RRAM devices to a certain extent, the variable size and random distribution of nanoparticles inside the switching layer inhibit further improvement in the uniformity of RRAM devices. Recently, some researchers have proposed that embedding highly ordered metal nano-islands (NIs) within the metal oxide switching layer could be an effective way to overcome the limitation of the random nanoparticle doping method. Wang *et al*. [173] employed a template-assisted fabrication approach to embedding the ordered metal NIs into the metal oxide thin film, in which the size, interspacing, and thickness of the NIs can be well controlled. The reduction

in operation voltages and the enhancement of the uniformity of resistance values at HRS and LRS are significant compared to the pristine oxide layer. Though the RRAM device embedded with ordered metal NIs has been shown to significantly improve the performance of the device, the underlying mechanism has not been fully understood.

In this Chapter, we develop a comprehensive physical model to study the electroforming and resistive switching behaviors in random and embedded HfO_2 based memristors. Firstly, we investigate the current-voltage characteristic, CF morphology, and current ON/OFF ratio of both random and embedded RRAM devices during electroforming and resistive switching processes. Secondly, the contribution of the embedded metal NIs to the enhancement of the uniformity of RRAMs is demonstrated. Our model clearly reveals that the initial nonuniform oxygen vacancy defect distribution is responsible for the stochasticity of CFs formation during the electroforming process, which leads to large variations in operation voltages and current ON/OFF ratios. Embedding metal NIs can effectively reduce variability and enhance the resistive switching performance of the devices. Moreover, the underlying mechanism of the role of the embedded metal NIs has been explored. Finally, we further investigate the impact of the height of metal NIs, the geometry, and the properties of different metal NIs (i.e., the oxygen affinity) on the resistive switching behavior. This model provides a fundamental understanding of how embedded NIs can improve the switching performance of the RRAMs which provides guidance for future microstructure design to realize more uniform and energy-efficient RRAMs.

5.2. Model

In this section, a simple Pt-HfO_2-Pt system is chosen as an example to describe the electroforming and subsequent resistive switching process. As mentioned in Chapter 3, a negative voltage is applied to perform the initial electroforming process, during which the $V_O^{\cdot\cdot}$ are generated from both a Frenkel defect inside the bulk oxide based on the Kröger-Vink notation ($O_O^{\times} \rightarrow V_O^{\cdot\cdot} + 2e' + \frac{1}{2}O_{2(g)}$)[34,108,117] and at metal/oxide interface based on the chemical reaction, i.e., $M_{electrode} + HfO_2 \rightarrow MO_\delta + HfO_{2-\delta} + \delta V_O^{\cdot\cdot}$. The bulk and interface generation rates of $V_O^{\cdot\cdot}$ are determined by Eq. (3-7) and Eq. (3-8), respectively. In this chapter, we ignore the $V_O^{\cdot\cdot}$ generation at the electrode/oxide interface due to the Pt electrode having a very large interface oxygen vacancy formation barrier. Once the CF is formed after the electroforming process, the subsequent reset and set processes are controlled by the $V_O^{\cdot\cdot}$ transport in the oxide layer driven by the local electric field and temperature [174]. Thus, the electroforming and resistive switching process controlled by the oxygen vacancy generation and migration can be described by the Nernst-Planck equation.

$$\frac{\partial N_{V_O^{\cdot\cdot}}}{\partial t} = -\nabla \cdot J_{V_O^{\cdot\cdot}} = \nabla \cdot (D\nabla N_{V_O^{\cdot\cdot}} + \frac{eD}{k_B T} N_{V_O^{\cdot\cdot}} \nabla\varphi + G) \tag{5-1}$$

The current continuity equation for electrical conduction (Eq. 5-2) and the thermal transport equation for Joule heating (Eq. 5-3) are coupled with Eq. 5-1 to calculate the local potential and temperature distribution.

$$\nabla \cdot \sigma\nabla\varphi = 0 \tag{5-2}$$

$$-\nabla \cdot k_{th}\nabla T = \sigma|\nabla\varphi|^2 \tag{5-3}$$

We use same the assumption for the electric conductivity σ and thermal conductivity k_{th} for the metal oxide layer, the details can be found in section 3.2.

Eq. 5-1 to 5-3 are self-consistently solved to obtain the oxygen vacancies density $N_{V_O^{\cdot\cdot}}$, the electrical potential φ and the temperature T using finite element method based on the platform of COMSOL Multi-physics. Fig. 5.1 illustrates the simulation geometry. A 10-nm-thick HfO_2 film is sandwiched between two 25-nm-thick Pt electrodes. The total simulation size is 60×60 nm^2 and the extremely fine physically controlled mesh size is chosen for simulation. The external electric voltage (V_{app}) with a sweep rate (dV/dt) of 1 V s^{-1} is applied to the top electrode, while the bottom electrode is grounded. The temperature at the outmost surfaces of two electrodes is defined with the boundary conditions T = 300 K. Zero migration flux $J_{V_O^{\cdot\cdot}}$ are assumed at the oxide/electrode interfaces and generation flux G.

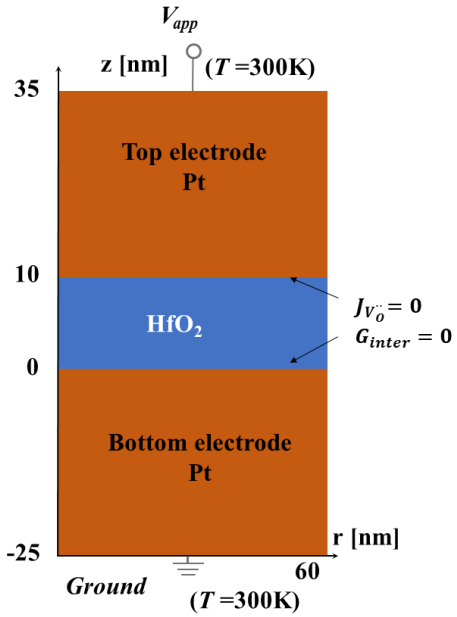

Fig. 5.1 Model geometry.

5.3. Results and discussion

5.3.1. The resistive switching behaviors for random and embedded RRAMs

To investigate the role of embedded metal NIs on the switching performance of the RRAMs, we model the CF growth and rupture dynamics during electroforming and resistive switching in both pristine random device and embedded metal NIs device. For the random structure, we simply assume that a small number of oxygen vacancy clusters are randomly dispersed in the HfO_2 layer, as shown in Fig. 5.2a. The oxygen vacancy density of the pre-existing $V_O^{\cdot\cdot}$ in defect cluster region (red dots) is assumed to be 1.2×10^{27} m^{-3}, whereas the stoichiometric HfO_2 region (grey matrix) has a lower oxygen vacancy density of 1.0×10^{15} m^{-3}. While for the embedded structure, highly ordered Pt NIs (d = 6 nm, h = 3 nm) is embedded in the middle of the oxide layer with the same initial $V_O^{\cdot\cdot}$ distribution, as shown in Fig. 5.2b. Then, a negative electric voltage is applied on the TE to perform the electroforming operation and stopped when the current (I_{stop}) reaches 200 μA. After that, a triangular positive voltage sweep is applied to realize the resistive switching process.

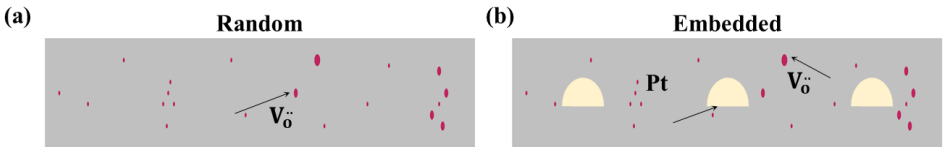

Fig. 5.2 The initial structure of the switching layer (a) random structure and (b) embedded structure.

Fig. 5.3 shows the current-voltage characteristics of HfO_2 thin film with random oxygen vacancies (black curve) and embedded with ordered metal NI arrays (red curve) during the electroforming, reset and set cycle. During the electroforming process, the total

currents of both random and embedded structures gradually increase until the applied voltage reaches the forming voltage (V_f), followed by a sudden increase of current for more than one order of magnitude, indicating the completion of the electroforming process. After that, the devices are switched from LRS to HRS under the application of a positive bias on TE (the reset process) and switched back to LRS under negative bias (the set process). By comparing the *I-V* curves of random and embedded structures, it is noted that the highly ordered embedded metal NIs effectively reduce the V_f from 1.82 V to 1.53 V and V_{set} from 1.22 V to 0.90 V, and slightly lower the V_{reset} from 0.81 V to 0.67 V.

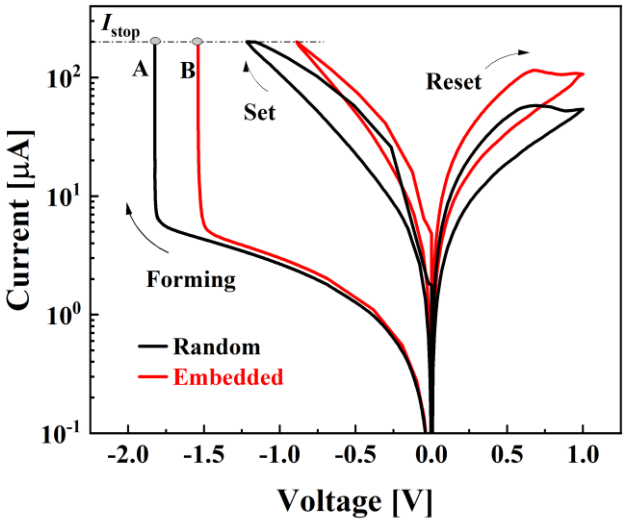

Fig. 5.3 Current-voltage curves for random and embedded devices

To investigate the different electroforming and resistive switching behaviors between random and embedded devices, we study the distributions of oxygen vacancy density $N_{V_O^{\cdot\cdot}}$, electrical field *E*, and temperature *T* for both random and embedded devices at the forming state, corresponding to points A and B as marked in Fig. 5.3. It is found that

a main CF is formed at the position where the initial oxygen vacancies are vertically concentrated (snapshot 1 in Fig. 5.4a), although multiple initial oxygen vacancy clusters are distributed in the HfO_2 layer. That is because the initial defect cluster has higher electrical conductivity than the stoichiometric HfO_2 matrix. Therefore, when a negative electric voltage is applied on the random device, the electric field distribution is inhomogeneous and enhanced above and below the oxygen vacancy clusters (snapshot 2 in Fig. 5.4a). Especially, the electric field is even larger in the local region with closely spaced $V_O^{\cdot\cdot}$ defects. Based on the Joule heating effect, the electric field enhancement further leads to localized heat generation (snapshot 3 in Fig. 5.4a). Therefore, the locally enhanced electric field and temperature promote the $V_O^{\cdot\cdot}$ generation rate, resulting in a large number of Frenkel pairs formation here. The CF growth formation and morphology highly depend on the initial defect clusters. Compared with random structures, the CFs with uniform morphology are only formed and aligned in the vicinity of the embedded Pt NIs. Due to the higher electric conductivity of Pt (1×10^7 S m^{-1}), the effective dielectric HfO_2 thickness around NIs is further decreased. As a result, the voltage drops over a shorter distance, and a higher field concentration at the top and bottom edge of metal NIs are generated by embedding Pt NIs inside the oxide layer, as snapshot 2 in Fig. 5.4b shows. Thus, the embedded NIs can be served as an electric concentrator. The corresponding temperature surrounding the metal NIs is also enhanced (snapshot 3 in Fig. 4b). The 1D profiles of the electric field and temperature along *z* direction across the center of NIs (Line 2 in snapshot 2 in Fig. 5.4b) and the closely spaced $V_O^{\cdot\cdot}$ defects cluster (Line 1 in snapshot 2 in Fig. 5.4b) in embedded device show that the electric field and temperature near the metal NIs are even larger than those around the initial $V_O^{\cdot\cdot}$ defect clusters, which favors the

$V_O^{\cdot\cdot}$ generation in these highly ordered regions during electroforming. Eventually, the CFs with uniform morphology preferentially grow along the metal NIs instead of along the initial $V_O^{\cdot\cdot}$ clusters. In addition, due to the enhanced electric field by embedding the Pt NIs within the oxide layer, the CF can be formed at a lower voltage, leading to a reduced temperature (~600K) near the CFs in comparison to the random structure (~1200K) (snapshots 3 in Fig. 5.4a and b). Since the high operation voltages and the temperature can cause undesirable crosstalk effects in the memristor crossbar, the reduction in the operation voltages and temperature benefits the application of memristor based electronic devices [175].

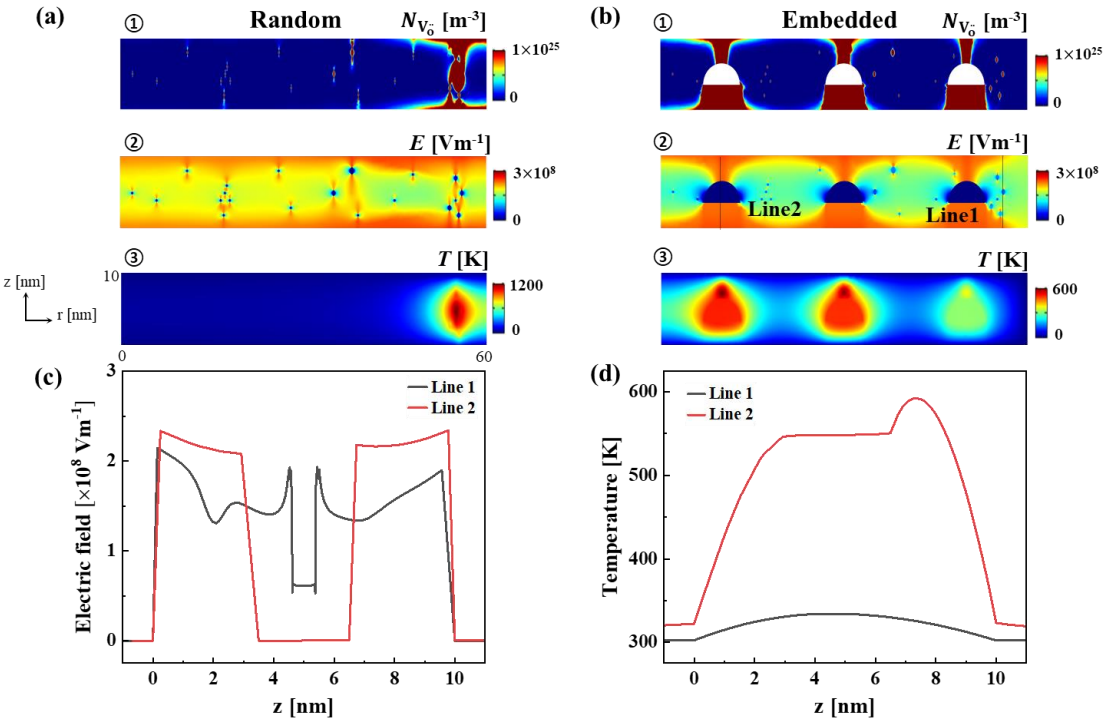

Fig. 5.4 (a, b) The 2D maps of oxygen vacancy density ($N_{V_O^{\cdot\cdot}}$), electric field (E), and temperature (T) at forming state for the HfO_2 thin film memristors with (a) random structure and (b) embedded structure. 1D profiles of (c) E and (d) T across the center of defect cluster (Line 1) and embedded NI (Line 2) marked as the dot lines in snapshot 2 in (b) at the forming state for the embedded structure.

A positive triangle voltage is applied on the devices to perform the reset process once the CF is formed. The $V_O^{\cdot\cdot}$ in the CF migrate from the TE to BE and the CF ruptures near TE for both random and embedded structures, as shown in Fig. 5.5a and b. The 1D electric field and temperature distributions along the center of the CFs at the final reset states (V_{app} = 1 V) in both random structure (Line 1 in Fig. 5.5a) and embedded structure (Line 2 in Fig. 5.5b) are shown in Fig. 5.5c and d. It is seen that the larger local electric field enhancement in the embedded device (red curve in Fig. 5.5c) increases the driving force for $V_O^{\cdot\cdot}$ migration towards BE, lowering the reset voltage and increasing the current ON/OFF ratio compared with the random case (Fig. 5.3). After reset switching, the CF is partially broken with some residual CF. Therefore, the subsequent set process requires a lower voltage than the initial electroforming process. Also, the embedded NI serves as an electric concentrator and facilitates the oxygen vacancy generation similar to the electroforming process, in which the V_{set} for embedded structure is smaller than that for random structure (Fig. 1c).

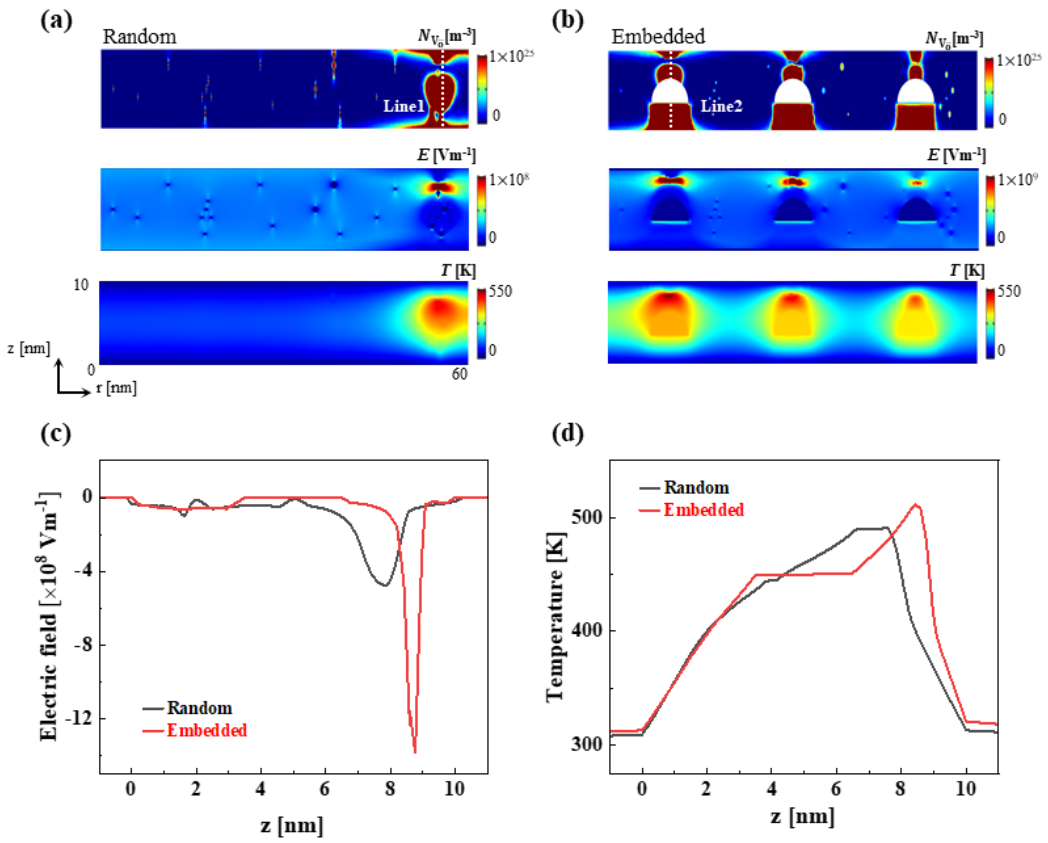

Fig. 5.5 (a, b) 2D maps of oxygen vacancy density $N_{V_O^{\cdot\cdot}}$, electric field (E) and temperature (T) at reset state (V_{app} = 1 V) in the (a) random structure and (b) embedded structure. (c, d) 1D profiles of (c) E and (d) T at reset state across the center of CF in the random structure and embedded structure marked as the dot lines in (a) and (b).

5.3.2. The improvement of uniformity of embedded RRAMs

The previous simulation results indicate that the initial oxygen vacancy density and distribution strongly affect the CF growth, however, the initial defect within the deposited HfO_2 thin film is unpredictable and uncontrollable due to the limitations of the synthesis process. To understand the effects of random $V_O^{\cdot\cdot}$ clusters, as well as the embedded NIs on confining the CF formation, we simulate the forming and switching behavior of devices containing different initial $V_O^{\cdot\cdot}$ defects in the switching layer, by changing the $V_O^{\cdot\cdot}$ clusters

distribution while keeping the total number of $V_O^{\cdot\cdot}$ constant in the initial HfO_2 film. The different random structures are shown in snapshot Init 1 to Init 3 in Fig. 5.6a-c. It is seen that the CFs are formed in different morphologies and at various positions for different initial random structures after the electroforming process. In some cases, a secondary sub-filament connected to TE and BE electrodes is formed within the HfO_2 layer (snapshot rm2 in Fig. 5.6b). The complexity of the morphologies and locations of the CFs due to the initial random microstructure is attributed to the instability and variability in RRAMs for both forming, reset, and set processes. In contrast to the stochastic formation of CFs in random devices, the CFs generated in the metal NIs embedded devices show much better uniformity. As snapshots emb1 to emb3 shown in Fig. 5.6a-c, three separately ordered CFs with uniform morphology and location are formed in the vicinity of metal Nis, regardless of the initial random structure of $V_O^{\cdot\cdot}$ clusters.

Moreover, the embedded devices also display highly uniform operation voltages and current ON/OFF ratios. Fig. 5.6d and e demonstrate the *I-V* characteristics of random and embedded devices, respectively. Fig. 5.6f compares the variations of the voltage and current ON/OFF ratio (I_{on}/I_{off}) for the random and embedded structures. It is seen that the I-V sweeps from multiple embedded devices are almost identical indicating a small fluctuation in the operation voltages and current ON/OFF ratio, whereas random devices have a large variation in these performance parameters, especially, the forming/set voltages often experience higher variability than the reset voltages, which are usually observed in many experimental works [156,166].

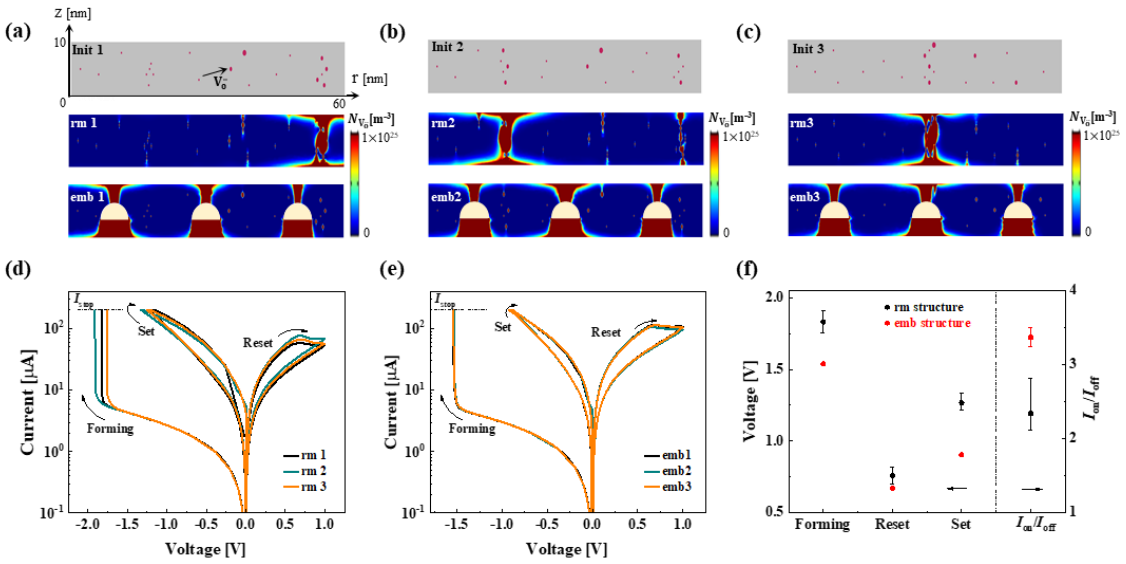

Fig. 5.6 (a-c) Three different initial states with the same number of $V_O^{\cdot\cdot}$ and the corresponding 2D maps of $N_{V_O^{\cdot\cdot}}$ at forming state. (d, e) Current-voltage curves for (d) the random structures (rm 1 to rm 3) and (e) embedded structures (emb 1 to 3). (f) The variations of the voltage and current ON/OFF ratio (I_{on}/I_{off}) for the random and embedded structures.

Table 5-1 summarizes the statistical results of operation voltages and I_{on}/I_{off} ratio of random and embedded devices. From this table, two distinct trends are obtained. First, the embedded metal NIs can reduce the V_f, V_{reset}, and V_{set} by 16%, 17%, and 28% on average, and enhance the I_{on}/I_{off} by an average of 30.8%, compared to the random structure. Second, the introduction of NIs effectively reduces the variations in operation voltages and I_{on}/I_{off}. To quantify these changes, we introduce a coefficient of variation (CV, defined as the ratio of the standard deviation (δ) to the mean value (μ)). The embedded devices show a significant uniformity in comparison with random structures, in which the CV of V_f, V_{reset}, and V_{set} are reduced by 97%, 63%, and 80%, respectively. Moreover, the embedded NIs significantly reduce the CV of I_{on}/I_{off} from 17.8% for random devices to 3.8%. The significantly reduced variation of the current ON/OFF ratio is highly favorable in the

application of the artificial neural network [159,175]. These findings highlight that the ordered metal NIs can achieve a highly controllable CF formation, which reduces the operation voltages and enhances the uniformity for both operation voltages and the current ON/OFF ratio in RRAMs.

Table 5-1 The results of V_f, V_{reset} and V_{set} and I_{on}/I_{off} comparing the Pt NIs embedded and random device

	V_f [V]	V_{reset} [V]	V_{set} [V]	I_{on}/I_{off}
rm 1	-1.82474	0.81	-1.218479	2.12
rm 2	-1.911527	0.760099	-1.331	2.075
rm 3	-1.754877	0.820106	-1.252	2.82
Average-random	-1.83	0.80	-1.27	2.33
CV-random	0.042875	0.040325	0.045592	0.178649
emb 1	-1.539636	0.670087	-0.901	3.5
emb 2	-1.536138	0.660086	-0.900091	3.24
emb 3	-1.53816	0.680088	-0.915	3.36
Average-embedded	-1.54	0.67	-0.91	3.37
CV-embedded	0.001138	0.014925	0.009231	0.038652

5.3.3. Effect of the height of the embedded metal nano-islands

Based on the previous results, the NIs can be served as an electric field concentrator and play a significant role in the dynamics of CF growth and rupture. In this section, we investigate the effect of the height of the metal NIs on the CF growth and the resistive switching behaviors. For simplicity, we ignore the initial pre-existing $V_O^{\cdot\cdot}$ defects within the HfO_2 layer and introduce only one embedded NI. From Fig. 5.7a and Table 5-2, it is found that V_f, V_{reset}, and V_{set} all decrease when h increases. That is because the effective thickness of HfO_2 along the vertical region of the NI decreases with the increasing of h, accordingly, resulting in a further enhanced local electric field above and below the NI. Comparing the electric field along the center of CF under the same applied voltage (V_{app} = -1 V,

corresponding to the point A marked in Fig. 5.7a) during the electroforming process, the maximum electric field has doubled when h increases from 1 nm to 5 nm (Fig. 5.7b). The enhancement of the local electric field accelerates the oxygen vacancies generation rate in the vicinity of NI which eventually decreases the forming and set voltages. Fig. 5.7c shows the 2D maps of $N_{V_O^{\cdot\cdot}}$ at forming state with metal NIs of different heights. It is also seen that a number of oxygen vacancies ($N_{V_O^{\cdot\cdot}}$ > 10^{25} m^{-3}) are generated at the oxide/electrode interfaces, when h = 1 nm, in addition to the CF of high oxygen vacancy density ($N_{V_O^{\cdot\cdot}}$) in the vicinity of the embedded NI. In contrast, when h = 5 nm, a small amount of $V_O^{\cdot\cdot}$ is generated at the electrode/oxide interfaces. This could be explained by the distribution of the electric field modulated by the NIs of various heights. By analyzing the electric field distribution at the forming state (Fig. 5.7d), it is seen that the electric field has been concentrated in the region above and below the NIs. When h decreases, the electric field concentration effect has been weakened, while that along the oxide/electrode interfaces gradually increases, which promotes the $V_O^{\cdot\cdot}$ generation in the electrode/oxide interfaces region.

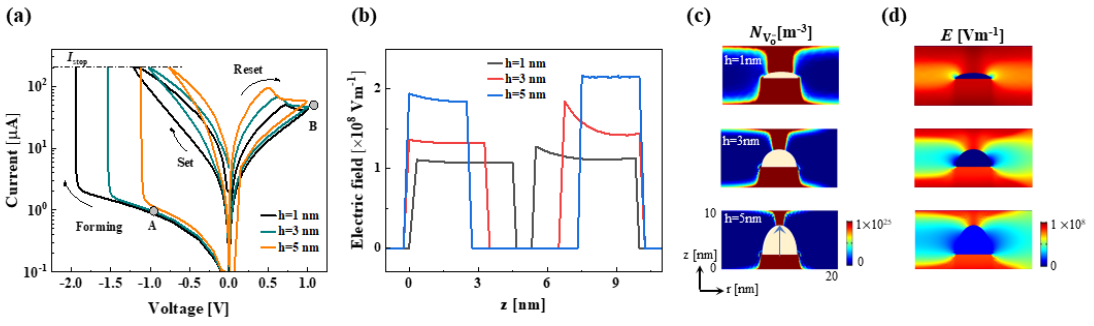

Fig. 5.7 (a) Current-voltage curves. (b) The electric field along the center of CF (r = 10 nm, z = 0 ~ 10 nm) at V_{app} = -1.0 V during the forming process, corresponding to the state A in (b). (c, d) 2D maps of (c) $N_{V_O^{\cdot\cdot}}$ and (d) E at forming state for device embedding metal NIs with increasing height.

Under positive voltage sweep, oxygen vacancies are driving to migrate from TE to BE and the CF is broken, thus increasing the device resistance, as shown in Fig. 5.8a. Fig. 5.8b and c demonstrate the 1D electric and temperature profiles along the center of the CF (r = 10 nm, z = 0 ~10 nm) at the reset state, corresponding to point B state marked in Fig. 5.7a. It is seen that the maximum local electric field near TE and the maximum temperature gradually increase when the height of NI increases, which promotes the $V_O^{\cdot\cdot}$ migration from TE to BE. Therefore, embedding NI with increasing height in the HfO_2 switching layer leads to an effective reduction in reset voltages and a significant increase in the I_{on}/I_{off} ratio, as shown in Fig. 5.7a and Table 5-2.

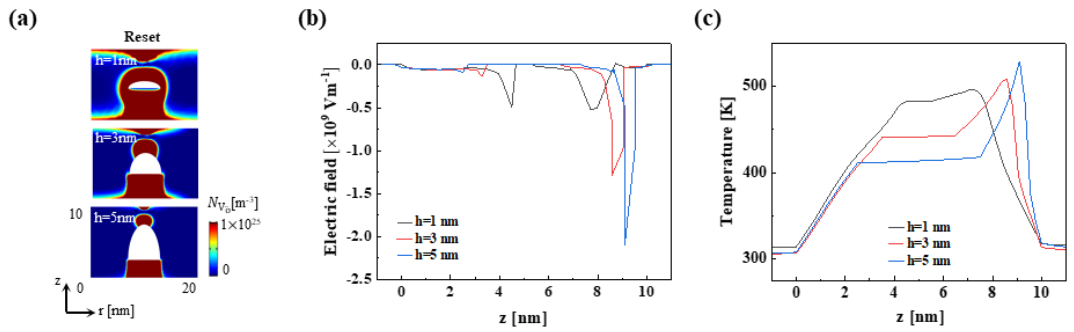

Fig. 5.8 (a) 2D maps of $N_{V_O^{\cdot\cdot}}$ at reset state for the structure embedding metal NI with increasing height. (b) The E and (c) T along the center of CF (r = 10 nm, z = 0 ~ 10 nm) at reset state (V_{app} = 1 V), corresponding to the sate B in Fig. 5.7a.

5.3.4. Effect of the geometry of the embedded metal nano-islands

The effect of the NI's geometry on the switching performance is also investigated. To focus on the shape effect, we employ three typical geometries (i.e., rectangle, semicircle, and triangle) NIs with the same area size and height (Fig. 5.9b). From Fig. 5.9a and Table 5-2, the forming and set voltages for devices with different geometries are unchanged,

while the reset voltage for triangle NIs based devices decreases and the I_{on}/I_{off} ratio enhances. Fig. 5.9c shows the 1D profile of oxygen vacancy density distribution along the center of CF at the forming state, corresponding to point A in Fig. 5.9a. It is seen that there is a local $V_O^{\cdot\cdot}$ enhancement at the tip of the triangle NI compared with semicircle and rectangle NIs although the forming voltages for different geometries are the same. To understand this phenomenon, we compared the evolution of the electric field distributions along the center of CF for different geometry of NIs during electroforming, as shown in Fig. 5.9d-f. It is seen that the electric field above and below the NIs gradually increases with time for all devices. However, the electric field enhancement above and below the NI are symmetric for rectangle NI, while it is highly asymmetric for triangle NIs with a local field concentration on top of the triangle tip (dash circle in Fig. 5.9f). This locally enhanced field accelerates the $V_O^{\cdot\cdot}$ generation and causes a local $V_O^{\cdot\cdot}$ enhancement at the tip of the triangle NI.

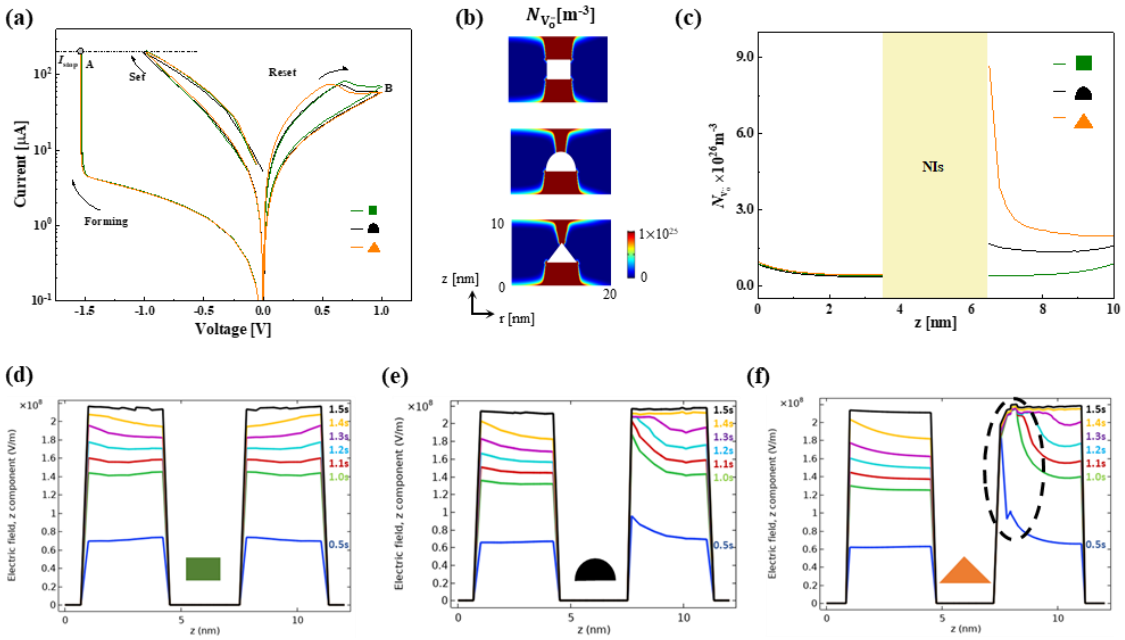

Fig. 5.9. (a) Current-voltage curves and (b) 2D maps of $N_{V_O^{\cdot\cdot}}$ at forming state. (c) 1D profiles of $N_{V_O^{\cdot\cdot}}$ along the center of CF at forming state, corresponding the point A in (a). (d-f) The evolution of electric field distribution along the center of CF during the forming process for devices embedding metal NIs with different geometries.

The geometry of NI has an influence on the reset behavior of the embedded device. Due to the higher $V_O^{\cdot\cdot}$ density at the tip of the triangle NI exhibits higher electric conductivity, and the locally enhanced electric field and temperature above the triangle NI tip are higher than those in other NI geometries during the reset operation (Fig. 5.10b and c), which promotes the $V_O^{\cdot\cdot}$ migration from TE to BE. Therefore, the corresponding V_{reset} is decreased and the $I_{\text{on}}/I_{\text{off}}$ ratio is enhanced by embedding triangle NI (Fig. 5.10 and Table 5-2).

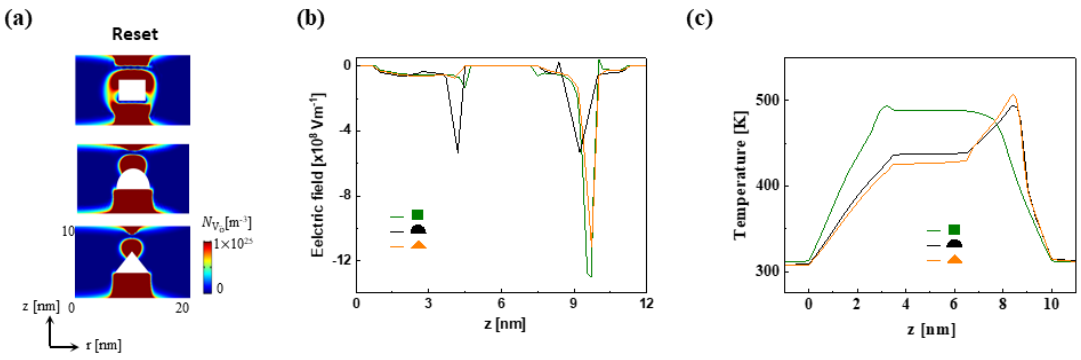

Fig. 5.10 (a) 2D maps of $N_{V_O^{\cdot\cdot}}$ at reset state for the structure embedding metal NI with different geometries. (b) The E and (c) T along the center of CF (r = 10 nm, z = 0 ~ 10 nm) at reset state (V_{app} = 1 V).

5.3.5. Effect of material properties of the embedded nano-islands

In the previous simulation, we ignored the $V_O^{\cdot\cdot}$ exchange at the electrode/oxide and oxide/NI interfaces (i.e., Pt/HfO_2 interfaces) due to the low oxygen affinity of the inert Pt, and we assume that the $V_O^{\cdot\cdot}$ are generated only from the Frenkel pairs inside the bulk of HfO_2 oxide. However, many works demonstrate that some active metals can also extract the oxygen atom from the oxide switching layer[118,173], which provides an additional $V_O^{\cdot\cdot}$ generation source. The $V_O^{\cdot\cdot}$ generation rate at the interface of metal/oxide ($G_{inter} = G_1 \cdot \left[\exp\left(\frac{-(E_b - \gamma E)}{k_B T}\right)\right]$) is strongly dependent on the metal properties, i.e., the ability to extract oxygen atoms from HfO_2 indicated by the interface vacancy formation energy E_b (details can be found in section 3.2). To fully understand the role of different metal NIs in the electroforming and switching processes, we select the metal Ti, Ta, and Pt as candidates for the embedded metal NIs with increasing E_b of 0.6, 2.5, and 8.5 eV, respectively [118], and incorporate the $V_O^{\cdot\cdot}$ generation from both bulk Frenkel pair and replacement reaction at the metal oxide/NI interface. Fig. 5.11a shows the current evolution of embedded devices with

different metal NIs (Ti, Ta, and Pt). It is clearly seen that embedding active metal with a smaller active vacancy formation energy barrier (E_b) result in a much smaller forming voltage for CF during the electroforming process. For example, compared with the Pt NI, embedding Ti NI within the HfO_2 layer decreases the forming voltage from 1.54 to 1.06 V. In addition, embedding NIs of different types of metals also affects the CF morphology after electroforming. Fig. 5.11b demonstrates the 2D maps of $V_O^{\cdot\cdot}$ density of embedded devices with different metal NIs at forming state. Due to the high affinity with oxygen, the Ti NI (E_b = 0.6 eV) could introduce additional oxygen vacancies around the HfO_2/Ti_NI interface compared to Pt NI (E_b = 8.5 eV). Compared to the interface oxygen vacancy generation rate during electroforming, the interface oxygen vacancy generation rate is suppressed with the increasing of E_b, as shown in Fig. 5.11c. Especially for inert embedding Pt NIs with a large vacancy formation barrier, almost no oxygen vacancies are generated near the oxide/Pt_NI interface, and the embedded Pt NI only displays the electric field concentration effect. To quantitatively analyze the oxygen vacancy generation with different embedded NIs, Fig. 5.11d displays the average $V_O^{\cdot\cdot}$ density along the center of the CF (r = 10, z = 0 ~ 10 nm) at the forming state. It is seen that the average $V_O^{\cdot\cdot}$ density of Ti NI embedded device reaches 2.32×10^{26} m^{-3}, which is almost ten times of that in Pt NI embedded device. Our analyses indicate that embedding active metal NIs can not only enlarge the width of CF, but also increase the $V_O^{\cdot\cdot}$ density inside the CF. Therefore, selecting metallic NIs of lower oxygen vacancy formation barrier within the host oxide is ideal to realize controllable CF growth at a much smaller formation voltage.

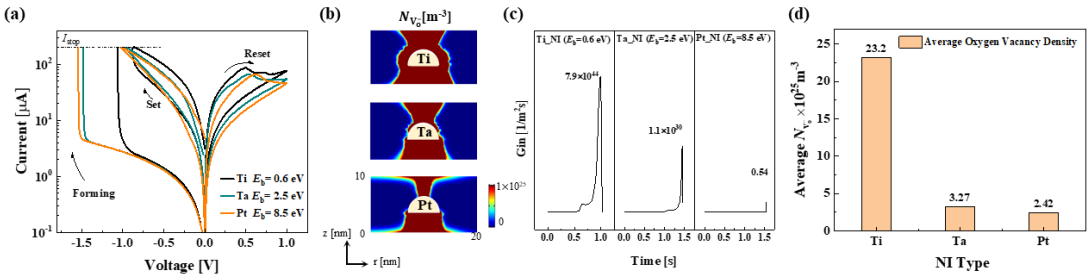

Fig. 5.11 (a) Current-voltage curves. (b) 2D maps of $N_{V_O^{\cdot\cdot}}$ at forming state for embedded devices with different metal NIs. (c) The interface oxygen vacancy generation rate at different metal NIs/oxide interfaces during electroforming process. (d) The average $N_{V_O^{\cdot\cdot}}$ along the center of CF (r = 10 nm, z = 0 ~ 10 nm) at the forming state.

Due to the high density of $V_O^{\cdot\cdot}$ in the Ti NI embedded devices, the formed CF exhibits a higher electric conductivity. The maximum local electric field and temperature for Ti NI embedded device are also larger than the others (Fig. 5.12b and c), which further promotes the $V_O^{\cdot\cdot}$ drift to BE to form a wider $V_O^{\cdot\cdot}$ depletion gap near TE, and switch the device to HRS. Therefore, the corresponding V_{reset} is further decreased and the I_{on}/I_{off} is enhanced by embedding active metal NIs with a smaller interface vacancy formation barrier, as shown in Fig. 5.11a and Table 5-2.

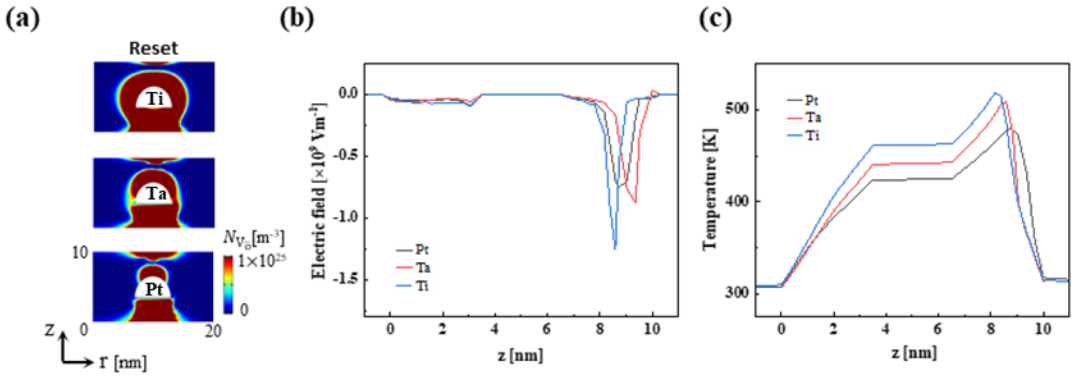

Fig. 5.12 (a) 2D maps of $N_{V_O^{\cdot\cdot}}$ at reset for the structure embedding different metal NIs. (b) The E and (c) T along the center of CF (r = 10 nm, z = 0 ~ 10 nm) at reset state (V_{app} = 1 V).

Table 5-2 The statistical results of operation voltages and I_{on}/I_{off} ratio of HfO_2 films embedding NIs with different heights, geometries, and materials.

	Type	V_f [V]	V_{reset} [V]	V_{set} [V]	I_{on}/I_{off}
Height	h = 1 nm	-1.94	0.72	-1.2	1.95
	h = 3 nm	-1.54	0.62	-1.01	3.56
	h = 5 nm	-1.11	0.48	-0.76	6.33
Geometry	Semicircle	-1.54	0.62	-1.01	3.56
	Rectangle	-1.54	0.74	-0.99	2.64
	Triangle	-1.53	0.57	-0.98	4.12
Materials	Ti (E_b = 0.6 eV)	-1.06	0.51	-0.87	4.2
	Ta (E_b = 2.5 eV)	-1.48	0.54	-0.94	3.85
	Pt (E_b = 8.5 eV)	-1.54	0.62	-1.01	3.56

5.4. Summary

In this section, we develop a physical model to understand the dynamic switching process including electroforming, reset, and set cycle in both random and embedded RRAM devices. It is found that the stochasticity in the CF growth during the electroforming process arises from the unpredictable and uncontrollable initial $V_O^{\cdot\cdot}$ defect clusters, which act as the CF formation seeds. Embedding highly ordered NIs could enhance the electrical field above and below the NIs, which promotes the oxygen vacancy generation and accumulation in the vicinity of NIs rather than surrounding the initial defect clusters, and realizes the controllable CF growth. In addition, the embedded metal NIs reduces the operation voltages and enhances the device-to-device uniformity in terms of operation voltages and I_{on}/I_{off} ratio. Our results also show that further improvements to decrease the operation voltages and increase the I_{on}/I_{off} ratio are achievable by increasing the height of NIs. We also demonstrate that the electric field is further enhanced on the top of the triangle NI compared with rectangle and semicircle shaped NIs, which influences the switching

behavior. Finally, the effect of material properties of the metal NIs (i.e., the energy barrier to extract oxygen atoms from the HfO_2 matrix, E_b) on the CF morphology and switching performance are investigated. The results demonstrate that embedding active metal NIs with smaller E_b enables additional $V_O^{\cdot\cdot}$ generation at the oxide/NI interface and enlarges the width of CF of higher $V_O^{\cdot\cdot}$ density. The reduction in the corresponding operation voltages and the increase in I_{on}/I_{off} ratio are also illustrated. This work provides a comprehensive understanding of the effect of embedding NIs on the CF formation and rupture during switching, and how it can be utilized to optimize the RRAM device variability, which can be employed to guide the experimental design of future memristors with high uniformity.

Chapter 6. Conclusions and future works

6.1. Conclusions

In conclusion, we developed a phase-field model by integrating the chemical reaction, ion and thermal transport, electrical conduction, and micro-elasticity theories to study the resistive switching behavior in metal oxide-based RRAMs. Our model can quantitatively describe the dynamic processes including electroforming and set/reset cycles which agree well with experimental electric measurement. First, we investigate the effects of the electrode on the conductive filament growth behavior during the initial one-time electroforming process. The competition between the oxygen vacancy generation rate at the active anodic interface and the migration rate in the bulk determines the CF morphology and growth direction. More active metal anode has a high affinity with oxygen exhibiting a smaller interface oxygen vacancy generation barrier (E_b) can provide high $V_O^{\cdot\cdot}$ generation rate at the anodic interface that larger than $V_O^{\cdot\cdot}$ migration rate inside the bulk, which allows CF grows from the anode to the cathode. The low $V_O^{\cdot\cdot}$ generation rate induced by inert anode is much smaller than the $V_O^{\cdot\cdot}$ migration rate which makes the $V_O^{\cdot\cdot}$ segregation in the cathode region and the CF propagates from the cathode to the anode.

Then, the effect of three key material properties including Vegard strain induced by the $V_O^{\cdot\cdot}$, electric conductivity and thermal conductivity of the metal oxide on the resistive switching behavior are systematically explored. It is revealed that metal oxide with a large Vegard strain coefficient inhibits the reset process and reduces the current ON/OFF ratio, as well as enhances the switching time. In addition, the metal oxide layer with higher

electric conductivity and lower thermal conductivity can form a homogenous CF during the electroforming process and exhibit a high current on/off ratio during resistive switching. Moreover, high-throughput phase-field simulations and a machine learning approach are employed to systematically explore the interpretable analytical correlations between these intrinsic material properties and the performance of metal oxide-based RRAM in terms of the current ON/OFF ratio (I_{on}/I_{off}) and resistance switching time (t_{switch}). This analytical model reveals that metal oxides with relatively small $\frac{k_{th}}{\sigma}$ ratios yield a higher switching performance (larger current ON/OFF ratio and faster switching speed). This work thereby establishes a key materials-design principle accelerating the future material discovery of RRAM and potentially guides the selection and design of metal oxide layer materials for further enhanced switching performance.

The large variations in the switching performance are contributed to the uncontrolled formation and rupture of CFs. By modeling the electroforming, reset, and set cycle in both random and embedded RRAM devices. It is illustrated that the unpredictable and uncontrollable initial $V_O^{\cdot\cdot}$ defect clusters act as the CF formation seeds, resulting in a large variation in forming, reset, and set operation voltages. Embedding highly ordered NIs can not only reduce the operation voltages, and enhance the current ON/OFF ratio, but also improve their uniformity compared with random devices. This behavior is attributed to the dimension confinement effect, embedding metal NIs can modulate the electric field distribution and leads to a more deterministic CF formation around NI's vicinity, in contrast to the random growth of CFs without embedded NIs. In addition, increasing the height of NIs, embedding triangle metal NIs, and using active metal NIs with high affinity with oxygen could further reduce the operation voltages and enhance the I_{on}/I_{off} ratio. This

work provides a fundamental understanding of how embedded metal NIs improve the switching behavior in oxide-based memristors and a potential strategy for microstructure optimization to realize a more uniform and highly energy-efficient RRAM devices than present materials.

These works presented here can either yield deeper insights into the resistive switching mechanism or will lower the barrier in finding the optimal materials and microstructure design for future RRAM devices suitable for neuromorphic computing hardware.

6.2. Future works

As mentioned, one of the critical challenges that inhibit the applications of metal oxides-based RRAM is the randomness in the formation and dissolution of the CFs, which results in large variance from cycle to cycle or cell to cell, especially in RRAM based neurocomputing crossbar. In our present work, we have only considered the initial point defects within the oxide switching layer which have a great influence on the formation and rupture of CFs, and embedding NIs can yield highly consistency switching among devices-to-device. However, the as-fabricated metal oxide switching layer consists of multiple defect types, such as grain boundary, dislocation, cracks, etc. Especially, the grain boundaries in the metal oxide layer are found as the preferred locations of oxygen vacancy formation and provide a path of lowered diffusion barrier for oxygen ions for several reports[176-179]. DFT calculations by K. Mckenna *et al*., yielded a diffusion barrier for oxygen vacancy migration along the 101-twin boundary in monoclinic HfO_2, compared with a value of 1.49 eV for oxygen vacancy migration through the lattice[177]. As shown in Fig. 6.1

and Table 6-1, our current molecular dynamics simulation results also show that the energy barriers for both oxygen formation and diffusion at 001- twin boundary are smaller than that in the bulk of HfO_2. In addition, grain boundaries will naturally occur in resistive switching devices and have been correlated with the non-uniformity of forming voltages due to randomized grain boundary networks in polycrystalline dielectric layers. Therefore, the effect of grain boundaries on the electroforming and resistive switching performance should be investigated. There are three main aspects of grain boundaries that can be studied in future works.

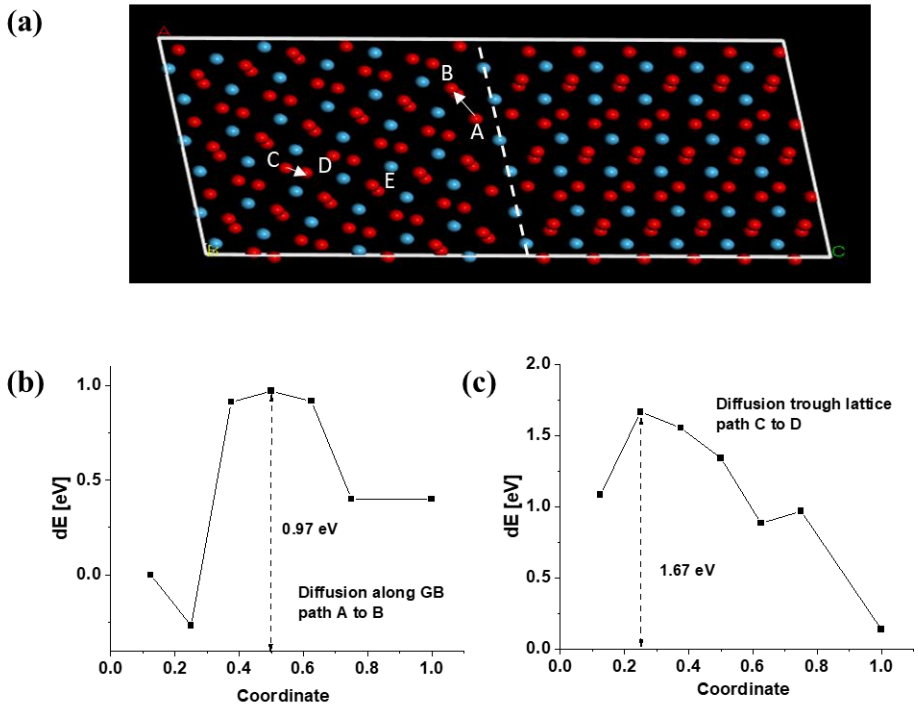

Fig. 6.1 a. Atomic structure near the 001-twin boundary in m-HfO_2, Hf ions (blue spheres) and O ions (red spheres). Migration barriers for oxygen ion diffusion b along the GB and c through the bulk lattice.

Table 6-1 The oxygen vacancy formation and diffusion barriers in the bulk and at the GB calculated by MD simulation.

$V_O^{\cdot\cdot}$ formation barrier	
3-fold $V_O^{\cdot\cdot}$ at C site	2.73 eV
4-fold $V_O^{\cdot\cdot}$ at E site	3.26 eV
$V_O^{\cdot\cdot}$ at GB	1.99 eV
$V_O^{\cdot\cdot}$ diffusion barrier	
Diffusion along GB path A to B	0.97 eV
Diffusion through lattice path C to D	1.67 eV

(1) Perform a molecular dynamics simulation to investigate the properties of grain boundaries including the vacancy formation barrier, vacancy diffusion barrier, and elastic properties. Then, by integrating atomic-scale simulation with phase-field simulation, the grain structure and their effect on the growth and rupture of the CFs shall be systematically studied.

(2) Investigate the effect of grain size, density, and orientation on the switching performances of metal oxide-based devices.

(3) Investigate the grain boundaries on the uniformity of RRAMs and study how to employ a grain boundary engineering approach to provide a perfect predefined CF growth and rupture, such as texture grain boundary.

APPENDIX: Material parameters used in the model

Parameters		Value	Description
D_0	[78,180]	2×10^{-7} [m^2/s]	Pre-exponential factor of diffusivity
E_a	[79]	1 [eV]($\varphi>0$) or 2.5 [eV]($\varphi<0$)	Diffusion barrier for oxygen vacancy
E_f	[181]	2.5 [eV]	Bulk vacancy formation energy barrier inside HfO_2 for Frenkel pair
γ	[182]	100 eÅ	Bond polarization factor of HfO_2
E_b (Ti/HfO_2)	[5]	0.6 [eV]	Interface vacancy formation energy barrier at Ti/HfO_2 interface
E_b (Ta/HfO_2)	[5]	2.5 [eV]	Interface vacancy formation energy barrier at Ta/HfO_2 interface
E_b (Pt/HfO_2)	[5]	8.5 [eV]	Interface vacancy formation energy barrier at Pt/HfO_2 interface
σ_{Pt}		1.0×10^7 [S m^{-1}]	Electrical conductivity of Pt
σ_{Ta}		7.7×10^6 [S m^{-1}]	Electrical conductivity of Ta
σ_{Ti}		2.5×10^6 [S m^{-1}]	Electrical conductivity of Ti
$k_{th\,(Pt)}$		77 [W m^{-1} K^{-1}]	Thermal conductivity of Pt
$k_{th\,(Ta)}$		57 [W m^{-1} K^{-1}]	Thermal conductivity of Ta
$k_{th\,(Ti)}$		22 [W m^{-1} K^{-1}]	Thermal conductivity of Ti
G_1		7×10^{25} [cm^{-3} s^{-1}]	Pre-exponential factors for bulk generation rates
G_2		7×10^{25} [cm^{-3} s^{-1}]	Pre-exponential factors for interface generation rates

REFERENCE

1 Borghetti, J. *et al.* 'Memristive' switches enable 'stateful' logic operations via material implication. *Nature* **464**, 873-876, doi:10.1038/nature08940 (2010).

2 Zidan, M. A., Strachan, J. P. & Lu, W. D. The future of electronics based on memristive systems. *Nature Electronics* **1**, 22-29, doi:10.1038/s41928-017-0006-8 (2018).

3 Xu, X., Rajendran, B. & Anantram, M. P. Kinetic Monte Carlo Simulation of Interface-Controlled Hafnia-Based Resistive Memory. *IEEE Transactions on Electron Devices* **67**, 118-124, doi:10.1109/ted.2019.2953917 (2020).

4 A. Padovani, L. Larcher, P. Padovani, C. Cagli & Salvo, B. D. Understanding the role of the Ti metal electrode on the forming of HfO_2-based RRAMs. *2012 4th IEEE International Memory Workshop*, 1-4, doi:10.1109/IMW.2012.6213667 (2012).

5 Chen, Y. Y. *et al.* Endurance/Retention Trade-off on HfO2/Metal Cap 1T1R Bipolar RRAM. *IEEE Transactions on Electron Devices* **60**, 1114-1121, doi:10.1109/ted.2013.2241064 (2013).

6 Lee, M. J. *et al.* A fast, high-endurance and scalable non-volatile memory device made from asymmetric $Ta_2O_{(5-x)}/TaO_{(2-x)}$ bilayer structures. *Nat Mater* **10**, 625-630, doi:10.1038/nmat3070 (2011).

7 Nardi, F., Larentis, S., Balatti, S., Gilmer, D. C. & Ielmini, D. Resistive switching by voltage-driven ion migration in bipolar RRAM-part I: experimental study. *IEEE Transactions on Electron Devices* **59**, 2461-2467, doi:10.1109/ted.2012.2202319 (2012).

8 Yang, J. J., Strukov, D. B. & Stewart, D. R. Memristive devices for computing. *Nat. Nanotechnol.* **8**, 13-24, doi:10.1038/nnano.2012.240 (2013).

9 Waser, R. & Aono, M. Nanoionics-based resistive switching memories. *Nat. Mater.* **6**, 833-840, doi:10.1038/nmat2023 (2007).

10 Ielmini, D. Resistive switching memories based on metal oxides: mechanisms, reliability and scaling. *Semiconductor Science and Technology* **31**, doi:10.1088/0268-1242/31/6/063002 (2016).

11 Celano, U. *et al.* Imaging the three-dimensional conductive channel in filamentary-based oxide resistive switching memory. *Nano Lett* **15**, 7970-7975, doi:10.1021/acs.nanolett.5b03078 (2015).

12 Yang, Y. C. *et al.* Observation of conducting filament growth in nanoscale resistive memories. *Nat Commun* **3**, 732 (2012).

13 Ielmini, D. Brain-inspired computing with resistive switching memory (RRAM): Devices, synapses and neural networks. *Microelectron. Eng.* **190**, 44-53, doi:10.1016/j.mee.2018.01.009 (2018).

14 Wang, Z. *et al.* Resistive switching materials for information processing. *Nat. Rev. Mater.* **5**, 173-195, doi:10.1038/s41578-019-0159-3 (2020).

15 Ielmini, D. & Wong, H. S. P. In-memory computing with resistive switching devices. *Nat. Electron.* **1**, 333-343, doi:10.1038/s41928-018-0092-2 (2018).

16 Ismail, M., Abbas, H., Choi, C. & Kim, S. Controllable analog resistive switching and synaptic characteristics in ZrO_2/ZTO bilayer memristive device for neuromorphic systems. *Appl. Surf. Sci.* **529**, 147107, doi:10.1016/j.apsusc.2020.147107 (2020).

17 Yao, P. *et al.* Face classification using electronic synapses. *Nat Commun* **8**, 15199, doi:10.1038/ncomms15199 (2017).

18 Prezioso, M. *et al.* Training and operation of an integrated neuromorphic network based on metal-oxide memristors. *Nature* **521**, 61-64, doi:10.1038/nature14441 (2015).

19 Yang, Y. *et al.* Electrochemical dynamics of nanoscale metallic inclusions in dielectrics. *Nat Commun* **5**, 4232, doi:10.1038/ncomms5232 (2014).

20 Kwon, D. H. *et al.* Atomic structure of conducting nanofilaments in TiO_2 resistive switching memory. *Nat Nanotechnol* **5**, 148-153, doi:10.1038/Nnano.2009.456 (2010).

21 Chen, J. Y. *et al.* Dynamic evolution of conducting nanofilament in resistive switching memories. *Nano Lett* **13**, 3671-3677, doi:10.1021/nl4015638 (2013).

22 Chen, J. Y., Huang, C. W., Chiu, C. H., Huang, Y. T. & Wu, W. W. Switching kinetic of VCM-based memristor: evolution and positioning of nanofilament. *Adv Mater* **27**, 5028-5033, doi:10.1002/adma.201502758 (2015).

23 Celano, U. *et al.* Three-dimensional observation of the conductive filament in nanoscaled resistive memory devices. *Nano Letters* **14**, 2401-2406, doi:10.1021/nl500049g (2014).

24 Celano, U. *et al.* Imaging the three-dimensional conductive channel in filamentary-based oxide resistive switching memory. *Nano Letters* **15**, 7970-7975, doi:10.1021/acs.nanolett.5b03078 (2015).

25 Wang, J. Y., Li, L. Z., Huyan, H. X., Pan, X. Q. & Nonnenmann, S. S. Highly uniform resistive switching in HfO_2 films embedded with ordered metal nanoisland arrays. *Adv Funct Mater* **29**, doi:10.1002/Adfm.201808430 (2019).

26 Chua, L. O. Memristor-The Missing Circuit Element. *IEEE TRANSACTIONS ON CIRCUIT THEORY* **CT18**, 507-519 (1971).

27 Strukov, D. B., Snider, G. S., Stewart, D. R. & Williams, R. S. The missing memristor found. *Nature* **453**, 80-83, doi:10.1038/nature06932 (2008).

28 Chen, Y. *et al.* Polymer memristor for information storage and neuromorphic applications. *Materials Horizons* **1**, doi:10.1039/c4mh00067f (2014).

29 Piotr Matyba, H. Y., Manish Chhowalla, Nathaniel D. Robinson, Ludvig Edman. Flexible and Metal-Free Light-Emitting Electrochemical Cells Based on Graphene

and PEDOT-PSS as the Electrode Materials. *Acs Nano* **5(1)**, 574-580, doi:https://doi.org/10.1021/nn102704h (2011).

30 Wu, G. *et al.* Artificial Synaptic Devices Based on Natural Chicken Albumen Coupled Electric-Double-Layer Transistors. *Sci Rep* **6**, 23578, doi:10.1038/srep23578 (2016).

31 Xu, J. *et al.* Biodegradable Natural Pectin-Based Flexible Multilevel Resistive Switching Memory for Transient Electronics. *Small* **15**, e1803970, doi:10.1002/smll.201803970 (2019).

32 Raeis-Hosseini, N., Park, Y. & Lee, J.-S. Flexible Artificial Synaptic Devices Based on Collagen from Fish Protein with Spike-Timing-Dependent Plasticity. *Adv Funct Mater* **28**, doi:10.1002/adfm.201800553 (2018).

33 H. Y. Lee *et al.* Low power and high speed bipolar switching with a thin reactive Ti buffer layer in robust HfO2 based RRAM. *2008 IEEE International Electron Devices Meeting*, 1-4, doi:10.1109/IEDM.2008.4796677 (2008).

34 Jeong, D. S., Schroeder, H., Breuer, U. & Waser, R. Characteristic electroforming behavior in Pt/TiO_2/Pt resistive switching cells depending on atmosphere. *Journal of Applied Physics* **104**, 123716, doi:10.1063/1.3043879 (2008).

35 Nam, Y. *et al.* Switchable Schottky diode characteristics induced by electroforming process in Mn-doped ZnO thin films. *Applied Physics Letters* **102**, 162105, doi:10.1063/1.4803088 (2013).

36 Z. Wei *et al.* Highly reliable TaO_x ReRAM and direct evidence of redox reaction mechanism. *2008 IEEE International Electron Devices Meeting*, 1-4, doi:10.1109/IEDM.2008.4796676 (2008).

37 Ielmini, D. *et al.* Scaling analysis of submicrometer nickel-oxide-based resistive switching memory devices. *Journal of Applied Physics* **109**, 034506, doi:10.1063/1.3544499 (2011).

38 Zhou, X. *et al.* A high performance electroformed single-crystallite VO_2 threshold switch. *Nanoscale* **11**, 22070-22078, doi:10.1039/c9nr08364b (2019).

39 Wang, S.-Y., Huang, C.-W., Lee, D.-Y., Tseng, T.-Y. & Chang, T.-C. Multilevel resistive switching in Ti/CuxO/Pt memory devices. *Journal of Applied Physics* **108**, doi:10.1063/1.3518514 (2010).

40 Nandi, S. K. *et al.* Electric field- and current-induced electroforming modes in NbO_x. *ACS Appl Mater Interfaces* **12**, 8422-8428, doi:10.1021/acsami.9b20252 (2020).

41 Janousch, M. *et al.* Role of oxygen vacancies in Cr-doped $SrTiO_3$ for resistance-change memory. *Adv Mater* **19**, 2232-2235, doi:10.1002/adma.200602915 (2007).

42 Sun, H. *et al.* Direct Observation of Conversion Between Threshold Switching and Memory Switching Induced by Conductive Filament Morphology. *Adv Funct Mater* **24**, 5679-5686, doi:10.1002/adfm.201401304 (2014).

43 Yang, Y. *et al.* Observation of conducting filament growth in nanoscale resistive memories. *Nature Communications* **3**, 732, doi:10.1038/Ncomms1737 (2012).

44 Yu Chao Yang, F. P., Qi Liu, Ming Liu, and Fei Zeng. Fully Room-Temperature-Fabricated Nonvolatile Resistive Memory for Ultrafast and High-Density Memory Application. *Nano Lett* **4**, 1636-1643 (2009).

45 Prakash, A. *et al.* Demonstration of Low Power 3-bit Multilevel Cell Characteristics in a TaO_{<italic>x</italic>}-Based RRAM by Stack Engineering. *IEEE Electron Device Letters* **36**, 32-34, doi:10.1109/led.2014.2375200 (2015).

46 Liu, L. *et al.* Coexistence of unipolar and bipolar resistive switching in BiFeO3 and Bi0.8Ca0.2FeO3 films. *Journal of Applied Physics* **111**, doi:10.1063/1.4716867 (2012).

47 Goux, L. *et al.* Evidences of oxygen-mediated resistive-switching mechanism in TiN\HfO2\Pt cells. *Applied Physics Letters* **97**, doi:10.1063/1.3527086 (2010).

48 Tsai, T.-L., Ho, T.-H. & Tseng, T.-Y. Unipolar resistive switching behaviors and mechanisms in an annealed Ni/ZrO2/TaN memory device. *Journal of Physics D: Applied Physics* **48**, doi:10.1088/0022-3727/48/3/035108 (2015).

49 Le, V.-Q. *et al.* Van der Waals heteroepitaxial AZO/NiO/AZO/muscovite (ANA/muscovite) transparent flexible memristor. *Nano Energy* **56**, 322-329, doi:10.1016/j.nanoen.2018.10.042 (2019).

50 Shariffar, A., Salman, H., Siddique, T. A., Gebril, W. & Manasreh, M. O. Resistive switching in FTO/CuO–Cu2O/Au memory devices. *Micro & Nano Letters* **15**, 853-857, doi:10.1049/mnl.2020.0300 (2020).

51 Seul Ki, H., Ji Eun, K., Sang Ouk, K., Sung-Yool, C. & Byung Jin, C. Flexible Resistive Switching Memory Device Based on Graphene Oxide. *IEEE Electron Device Letters* **31**, 1005-1007, doi:10.1109/led.2010.2053695 (2010).

52 Nandi, S. K., Liu, X., Venkatachalam, D. K. & Elliman, R. G. Effect of electrode roughness on electroforming in HfO_2 and defect-induced moderation of electric-field enhancement. *Physical Review Applied* **4**, 064010, doi:10.1103/PhysRevApplied.4.064010 (2015).

53 E. Abbaspour, S. Menzel & Jungemann, C. The role of the interface reactions in the electroforming of redox-based resistive switching devices using KMC simulations. *2015 International Conference on Simulation of Semiconductor Processes and Devices (SISPAD)*, 293-296, doi:10.1109/SISPAD.2015.7292317 (2015).

54 Gomez-Marlasca, F., Ghenzi, N., Rozenberg, M. J. & Levy, P. Understanding electroforming in bipolar resistive switching oxides. *Applied Physics Letters* **98**, 042901, doi:10.1063/1.3537957 (2011).

55 F.A. Chudnovskii, L.L. Odynets, A.L. Pergament & Stefanovich, G. B. Electroforming and switching in oxides of transition metals: the role of metal–insulator transition in the switching mechanism. *Journal of Solid State Chemistry* **122**, 95-99 (1996).

56 Pan, F., Gao, S., Chen, C., Song, C. & Zeng, F. Recent progress in resistive random access memories: Materials, switching mechanisms, and performance. *Materials*

Science and Engineering: R: Reports **83**, 1-59, doi:10.1016/j.mser.2014.06.002 (2014).

57 Kozicki, M. N., Park, M. & Mitkova, M. Nanoscale memory elements based on solid-state electrolytes. *IEEE Transactions On Nanotechnology* **4**, 331-338, doi:10.1109/tnano.2005.846936 (2005).

58 Guo, X., Schindler, C., Menzel, S. & Waser, R. Understanding the switching-off mechanism in Ag^+ migration based resistively switching model systems. *Applied Physics Letters* **91**, doi:10.1063/1.2793686 (2007).

59 Jeong, D. S., Schroeder, H., Breuer, U. & Waser, R. Characteristic electroforming behavior in Pt/TiO_2/Pt resistive switching cells depending on atmosphere. *Journal of Applied Physics* **104**, doi:10.1063/1.3043879 (2008).

60 Ielmini, D. *et al.* Scaling analysis of submicrometer nickel-oxide-based resistive switching memory devices. *Journal of Applied Physics* **109**, doi:10.1063/1.3544499 (2011).

61 Ielmini, D., Nardi, F. & Cagli, C. Physical models of size-dependent nanofilament formation and rupture in NiO resistive switching memories. *Nanotechnology* **22**, 254022, doi:10.1088/0957-4484/22/25/254022 (2011).

62 Bersuker, G. *et al.* Metal oxide resistive memory switching mechanism based on conductive filament properties. *Journal of Applied Physics* **110**, doi:10.1063/1.3671565 (2011).

63 Zhuang, H. L., Ganesh, P., Cooper, V. R., Xu, H. & Kent, P. R. C. Understanding the interactions between oxygen vacancies at $SrTiO_3$ (001) surfaces. *Physical Review B* **90**, doi:10.1103/PhysRevB.90.064106 (2014).

64 Li, C. *et al.* Dynamic observation of oxygen vacancies in hafnia layer by in situ transmission electron microscopy. *Nano Research* **8**, 3571-3579, doi:10.1007/s12274-015-0857-0 (2015).

65 Sawa, A. Resistive switching in transition metal oxides. *Materials Today* **11**, 28-36, doi:10.1016/s1369-7021(08)70119-6 (2008).

66 Chen, A. B., Kim, S. G., Wang, Y., Tung, W. S. & Chen, I. W. A size-dependent nanoscale metal-insulator transition in random materials. *Nat Nanotechnol* **6**, 237-241, doi:10.1038/nnano.2011.21 (2011).

67 Ding, G. *et al.* Configurable multi-state non-volatile memory behaviors in Ti3C2 nanosheets. *Nanoscale* **11**, 7102-7110, doi:10.1039/c9nr00747d (2019).

68 Li, C. *et al.* Direct Observations of Nanofilament Evolution in Switching Processes in HfO2 -Based Resistive Random Access Memory by In Situ TEM Studies. *Adv Mater* **29**, doi:10.1002/adma.201602976 (2017).

69 Kwon, D. H. *et al.* Atomic structure of conducting nanofilaments in TiO_2 resistive switching memory. *Nat Nanotechnol* **5**, 148-153, doi:10.1038/nnano.2009.456 (2010).

70 Celano, U. *et al.* Three-dimensional observation of the conductive filament in nanoscaled resistive memory devices. *Nano Lett* **14**, 2401-2406, doi:10.1021/nl500049g (2014).

71 Sankaran, K. *et al.* Modeling of copper diffusion in amorphous aluminum oxide in CBRAM stack. *Ecs Transactions* **45**, 317-330, doi:10.1149/1.3700896 (2012).

72 Kamiya, K. *et al.* ON-OFF switching mechanism of resistive-random-access-memories based on the formation and disruption of oxygen vacancy conducting channels. *Applied Physics Letters* **100**, doi:10.1063/1.3685222 (2012).

73 Clima, S. *et al.* First-principles simulation of oxygen diffusion in HfOx: Role in the resistive switching mechanism. *Applied Physics Letters* **100**, doi:10.1063/1.3697690 (2012).

74 Jiang, H. & Stewart, D. A. Enhanced oxygen vacancy diffusion in Ta_2O_5 resistive memory devices due to infinitely adaptive crystal structure. *Journal of Applied Physics* **119**, doi:10.1063/1.4945579 (2016).

75 Bondi, R. J., Fox, B. P. & Marinella, M. J. Role of atomistic structure in the stochastic nature of conductivity in substoichiometric tantalum pentoxide. *Journal of Applied Physics* **119**, doi:10.1063/1.4943163 (2016).

76 Onofrio, N., Guzman, D. & Strachan, A. Atomic origin of ultrafast resistance switching in nanoscale electrometallization cells. *Nature Materials* **14**, 440-446, doi:10.1038/NMAT4221 (2015).

77 Onofrio, N., Guzman, D. & Strachan, A. Atomistic simulations of electrochemical metallization cells: mechanisms of ultra-fast resistance switching in nanoscale devices. *Nanoscale* **8**, 14037-14047, doi:10.1039/c6nr01335j (2016).

78 Larentis, S., Nardi, F., Balatti, S., Gilmer, D. C. & Ielmini, D. Resistive switching by voltage-driven ion migration in bipolar RRAM-part II: modeling. *Ieee Transactions on Electron Devices* **59**, 2468-2475, doi:10.1109/Ted.2012.2202320 (2012).

79 Kim, S. *et al.* Physical electro-thermal model of resistive switching in bi-layered resistance-change memory. *Sci Rep-Uk* **3**, 1680, doi:10.1038/Srep01680 (2013).

80 Kim, S., Choi, S. & Lu, W. Comprehensive physical model of dynamic resistive switching in an oxide memristor. *Acs Nano* **8**, 2369-2376, doi:10.1021/nn405827t (2014).

81 Menzel, S. *et al.* Origin of the ultra-nonlinear switching kinetics in oxide-based resistive switches. *Adv Funct Mater* **21**, 4487-4492, doi:10.1002/adfm.201101117 (2011).

82 Marchewka, A. *et al.* Nanoionic resistive switching memories: on the physical nature of the dynamic reset process. *Adv Electron Mater* **2**, doi:10.1002/Aelm.201500233 (2016).

83 Guan, X., Yu, S. & Wong, H. S. P. A SPICE Compact Model of Metal Oxide Resistive Switching Memory With Variations. *IEEE Electron Device Letters* **33**, 1405-1407, doi:10.1109/led.2012.2210856 (2012).

84 Shimeng Yu, B. G., Zheng Fang, Hongyu Yu, Jinfeng Kang, and H.-S. Philip Wong. A Neuromorphic Visual System Using RRAM Synaptic Devices with Sub-pJ Energy and Tolerance to Variability:Experimental Characterization and Large-

Scale Modeling. *2012 International Electron Devices Meeting* **33**, 1405-1407, doi:doi: 10.1109/IEDM.2012.6479018. (2012).

85 Russo, U., Ielmini, D., Cagli, C. & Lacaita, A. L. Self-Accelerated Thermal Dissolution Model for Reset Programming in Unipolar Resistive-Switching Memory (RRAM) Devices. *IEEE Transactions on Electron Devices* **56**, 193-200, doi:10.1109/ted.2008.2010584 (2009).

86 Russo, U., Ielmini, D., Cagli, C. & Lacaita, A. L. Filament Conduction and Reset Mechanism in NiO-Based Resistive-Switching Memory (RRAM) Devices. *IEEE Transactions on Electron Devices* **56**, 186-192, doi:10.1109/ted.2008.2010583 (2009).

87 U. Russo, D. J., C. Cagli, A. L. Lacaita, S. Spigat, C. Wiemert, M. Peregot and M. Fanciullit. Conductive-filament switching analysis and self-accelerated thermal dissolution model for reset in NiO-based RRAM. *2007 IEEE International Electron Devices Meeting*, 775-778, doi:doi: 10.1109/IEDM.2007.4419062 (2007).

88 Abbaspour;, E., Menzel;, S. & Jungemann;, C. KMC Simulation of the Electroforming, Set and Reset Processes in Redox-based Resistive Switching Devices. *Simulation of Semiconductor Processes and Devices*, 141-144 (2016).

89 Dirkmann, S., Kaiser, J., Wenger, C. & Mussenbrock, T. Filament Growth and Resistive Switching in Hafnium Oxide Memristive Devices. *ACS Appl Mater Interfaces* **10**, 14857-14868, doi:10.1021/acsami.7b19836 (2018).

90 Jagan Singh Meena, S. M. S., Umesh Chand and Tseung-Yuen Tseng. Overview of emerging nonvolatile memory technologies. *Nanoscale Research Letters* **9** (2014).

91 Zahoor, F., Azni Zulkifli, T. Z. & Khanday, F. A. Resistive Random Access Memory (RRAM): an Overview of Materials, Switching Mechanism, Performance, Multilevel Cell (mlc) Storage, Modeling, and Applications. *Nanoscale Res Lett* **15**, 90, doi:10.1186/s11671-020-03299-9 (2020).

92 Prakash, A., Deleruyelle, D., Song, J., Bocquet, M. & Hwang, H. Resistance controllability and variability improvement in a TaOx-based resistive memory for multilevel storage application. *Applied Physics Letters* **106**, doi:10.1063/1.4922446 (2015).

93 Zhao, L. *et al.* Multi-level control of conductive nano-filament evolution in HfO2 ReRAM by pulse-train operations. *Nanoscale* **6**, 5698-5702, doi:10.1039/c4nr00500g (2014).

94 Yu, S., Wu, Y. & Wong, H. S. P. Investigating the switching dynamics and multilevel capability of bipolar metal oxide resistive switching memory. *Applied Physics Letters* **98**, doi:10.1063/1.3564883 (2011).

95 Paul A. Merolla, J. V. A., Rodrigo Alvarez-Icaza,Andrew S. Cassidy,Jun Sawada, Filipp Akopyan, Bryan L. Jackson,Nabil Imam, Chen Guo, Yutaka Nakamura, Bernard Brezzo, Ivan Vo, Steven K. Esser, Rathinakumar Appuswamy, Brian Taba, Arnon Amir, Myron D. Flickner, William P. Risk, Rajit Manohar, Dharmendra S. Modha. Amillion spiking-neuron integrated circuit with a scalable communication network and interface. *SCIENCE* **345**, 668-673, doi:DOI: 10.1126/science.1254642 (2014).

96 Jo, S. H. *et al.* Nanoscale memristor device as synapse in neuromorphic systems. *Nano Lett* **10**, 1297-1301, doi:10.1021/nl904092h (2010).

97 Yao, P. *et al.* Face classification using electronic synapses. *Nat Commun* **8**, 15199, doi:10.1038/ncomms15199 (2017).

98 Y. S. Chen, H. Y. L., P. S. Chen, P. Y. Gu, C. W. Chen, W. P. Lin, W. H. Liu, Y. Y. Hsu, S. S. Sheu, P. C. Chiang, W. S. Chen, F. T. Chen,C. H. Lien, and M.-J. Tsai. Highly Scalable Hafnium Oxide Memory with Improvements of Resistive Distribution and Read Disturb Immunity. *2009 IEEE International Electron Devices Meeting (IEDM)* **9**, 105-108, doi:DOI:10.1109/IEDM.2009.5424411 (2009).

99 Chen, C. Y., Goux, L., Fantini, A., Redolfi, A., Clima, S., Degraeve, R., Chen, Y.Y., Groeseneken, G., Jurczak, M. Understanding the impact of programming pulses and electrode materials on the endurance properties of scaled Ta2O5 RRAM cells. *2014 IEEE International Electron Devices Meeting* **14**, 1-4, doi:	10.1109/IEDM.2014.7047049 (2014).

100 L. Goux, A. F., A. Redolfi, C.Y. Chen, F.F. Shi, R. Degraeve, Y.Y. Chen, T. Witters, G. Groeseneken, M. Jurczak. Role of the Ta scavenger electrode in the excellent switching control and reliability of a scalable low-current operated TiN\Ta2O5\Ta RRAM device. *2014 Symposium on VLSI Technology Digest of Technical Papers*, doi:DOI:10.1109/VLSIT.2014.6894401 (2014).

101 Wang, C. *et al.* Conduction mechanisms, dynamics and stability in ReRAMs. *Microelectronic Engineering* **187-188**, 121-133, doi:10.1016/j.mee.2017.11.003 (2018).

102 A. Fantini, L. G., R. Degraeve, D.J. Wouters, N. Raghavan, G. Kar, A. Belmonte,Y.-Y. Chen, B. Govoreanu, M. Jurczak. Intrinsic Switching Variability in HfO2 RRAM. *2013 5th IEEE International Memory Workshop*, 30-33, doi:doi: 10.1109/IMW.2013.6582090 (2013).

103 Ambrogio, S. *et al.* Statistical Fluctuations in HfO_{<italic><bold>x</bold></italic>} Resistive-Switching Memory: Part I - Set/Reset Variability. *IEEE Transactions on Electron Devices* **61**, 2912-2919, doi:10.1109/ted.2014.2330200 (2014).

104 Baeumer, C. *et al.* Subfilamentary Networks Cause Cycle-to-Cycle Variability in Memristive Devices. *ACS Nano* **11**, 6921-6929, doi:10.1021/acsnano.7b02113 (2017).

105 Bersuker, G. *et al.* Metal oxide resistive memory switching mechanism based on conductive filament properties. *Journal of Applied Physics* **110**, 124518, doi:10.1063/1.3671565 (2011).

106 Sharma, A. A. *et al.* Dynamics of electroforming in binary metal oxide-based resistive switching memory. *Journal of Applied Physics* **118**, 114903, doi:10.1063/1.4930051 (2015).

107 Chakraverty, B. K. Metal-insulator transition; nucleation of a conducting phase in amorphous semiconductors. *Journal of Non-Crystalline Solids* **3**, 317-326, doi:https://doi.org/10.1016/0022-3093(70)90002-5 (1970).

108 Yang, J. J. *et al.* The mechanism of electroforming of metal oxide memristive switches. *Nanotechnology* **20**, 215201, doi:10.1088/0957-4484/20/21/215201 (2009).

109 Huang, J. J., Kuo, C. W., Chang, W. C. & Hou, T. H. Transition of stable rectification to resistive-switching in Ti/TiO_2/Pt oxide diode. *Applied Physics Letters* **96**, 262901, doi:10.1063/1.3457866 (2010).

110 Yalon, E. *et al.* Detection of the insulating gap and conductive filament growth direction in resistive memories. *Nanoscale* **7**, 15434-15441, doi:10.1039/c5nr03314d (2015).

111 Sun, P. *et al.* Physical model for electroforming process in valence change resistive random access memory. *Journal of Computational Electronics* **14**, 146-150, doi:10.1007/s10825-014-0634-4 (2014).

112 Noman, M. *et al.* Mechanism of localized electrical conduction at the onset of electroforming in TiO_2 based resistive switching devices. *Applied Physics Letters* **104**, 113510, doi:10.1063/1.4869230 (2014).

113 D. C. Gilmer *et al.* Effects of RRAM stack configuration on forming voltage and current overshoot. *2011 3rd IEEE International Memory Workshop (IMW)*, 1-4, doi:10.1109/IMW.2011.5873225 (2011).

114 Ielmini, D., Cagli, C. & Nardi, F. Resistance transition in metal oxides induced by electronic threshold switching. *Applied Physics Letters* **94**, 063511, doi:10.1063/1.3081401 (2009).

115 Sharma, A. A., Noman, M., Abdelmoula, M., Skowronski, M. & Bain, J. A. Electronic instabilities leading to electroformation of binary metal oxide-based resistive switches. *Adv Funct Mater* **24**, 5522-5529, doi:10.1002/adfm.201400461 (2014).

116 Ielmini, D., Nardi, F. & Cagli, C. Universal reset characteristics of unipolar and bipolar metal-oxide RRAM. *IEEE Transactions on Electron Devices* **58**, 3246-3253, doi:10.1109/ted.2011.2161088 (2011).

117 Sharath, S. U. *et al.* Impact of oxygen stoichiometry on electroforming and multiple switching modes in TiN/TaO*x*/Pt based ReRAM. *Appl. Phys. Lett.* **109**, 173503, doi:10.1063/1.4965872 (2016).

118 Chen, Y. Y. *et al.* Endurance/retention trade-off on HfO_2/metal cap 1T1R bipolar RRAM. *IEEE Tran. Electron Devices* **60**, 1114-1121, doi:10.1109/ted.2013.2241064 (2013).

119 Huang, J. J., Kuo, C. W., Chang, W. C. & Hou, T. H. Transition of stable rectification to resistive-switching in Ti/TiO_2/Pt oxide diode. *Appl. Phys. Lett.* **96**, 262901, doi:10.1063/1.3457866 (2010).

120 Bersuker, G. *et al.* Metal oxide resistive memory switching mechanism based on conductive filament properties. *J. Appl. Phys.* **110**, 124518, doi:10.1063/1.3671565 (2011).

121 Xu, X., Rajendran, B. & Anantram, M. P. Kinetic monte carlo simulation of interface-controlled hafnia-based resistive memory. *IEEE Trans. Electron Devices* **67**, 118-124, doi:10.1109/ted.2019.2953917 (2020).

122 Panzer, M. A. *et al.* Thermal properties of ultrathin hafnium oxide gate dielectric films. *IEEE Electron Device Letters* **30**, 1269-1271, doi:10.1109/led.2009.2032937 (2009).

123 Milošević, N. D. & Maglić, K. D. Thermophysical properties of solid phase hafnium at high temperatures. *International Journal of Thermophysics* **27**, 530-553, doi:10.1007/s10765-006-0045-2 (2006).

124 Chen, Y.-C. *et al.* Dynamic conductance characteristics in HfOx-based resistive random access memory. *RSC Advances* **7**, 12984-12989, doi:10.1039/c7ra00567a (2017).

125 Chand, U. *et al.* Suppression of endurance degradation by utilizing oxygen plasma treatment in HfO2 resistive switching memory. *Applied Physics Letters* **106**, doi:10.1063/1.4918679 (2015).

126 Wu, Q. *et al.* Improvement of durability and switching speed by incorporating nanocrystals in the HfOx based resistive random access memory devices. *Applied Physics Letters* **113**, doi:10.1063/1.5030780 (2018).

127 Yoon, J. H. *et al.* Highly uniform, electroforming-free, and self-rectifying resistive memory in the Pt/Ta_2O_5/HfO_{2-x}/TiN Structure. *Adv Funct Mater* **24**, 5086-5095, doi:10.1002/adfm.201400064 (2014).

128 Yang, J. J. *et al.* High switching endurance in TaOx memristive devices. *Applied Physics Letters* **97**, 232102, doi:10.1063/1.3524521 (2010).

129 Ambrogio, S., Balatti, S., Choi, S. & Ielmini, D. Impact of the mechanical stress on switching characteristics of electrochemical resistive memory. *Adv Mater* **26**, 3885-3892, doi:10.1002/adma.201306250 (2014).

130 Nicholas, J. D., Qi, Y., Bishop, S. R. & Mukherjee, P. P. Introduction to mechano-electro-chemical coupling in energy related materials and devices. *Journal of The Electrochemical Society* **161**, Y11-Y12, doi:10.1149/2.0231411jes (2014).

131 Billah, M. M., Hasan, M. M. & Jang, J. Effect of tensile and compressive bending stress on electrical performance of flexible a-IGZO TFTs. *IEEE Electron Device Letters* **38**, 890-893, doi:10.1109/led.2017.2707279 (2017).

132 Korobko, R. *et al.* Giant electrostriction in Gd-doped ceria. *Adv Mater* **24**, 5857-5861, doi:10.1002/adma.201202270 (2012).

133 Schmitt, R., Spring, J., Korobko, R. & Rupp, J. L. M. Design of oxygen vacancy configuration for memristive systems. *ACS Nano* **11**, 8881-8891, doi:10.1021/acsnano.7b03116 (2017).

134 Esposito, V. & Traversa, E. Design of electroceramics for solid oxides fuel cell applications: playing with ceria. *Journal of the American Ceramic Society* **91**, 1037-1051, doi:10.1111/j.1551-2916.2008.02347.x (2008).

135 Ghicov, A. & Schmuki, P. Self-ordering electrochemistry: a review on growth and functionality of TiO^2 nanotubes and other self-aligned MO(x) structures. *Chem Commun (Camb)*, 2791-2808, doi:10.1039/b822726h (2009).

136 Balachandran, J., Lin, L., Anchell, J. S., Bridges, C. A. & Ganesh, P. Defect genome of cubic perovskites for fuel cell applications. *The Journal of Physical Chemistry C* **121**, 26637-26647, doi:10.1021/acs.jpcc.7b08716 (2017).

137 Hu, G., Fung, V., Sang, X., Unocic, R. R. & Ganesh, P. Predicting synthesizable multi-functional edge reconstructions in two-dimensional transition metal dichalcogenides. *npj Computational Materials* **6**, doi:10.1038/s41524-020-0327-4 (2020).

138 Shen, Z. H. *et al.* Phase-field modeling and machine learning of electric-thermal-mechanical breakdown of polymer-based dielectrics. *Nat Commun* **10**, 1843, doi:10.1038/S41467-019-09874-8 (2019).

139 Zhang, Y. *et al.* Unsupervised discovery of solid-state lithium ion conductors. *Nat Commun* **10**, 5260, doi:10.1038/S41467-019-13214-1 (2019).

140 Cao, Y., Morozovska, A. & Kalinin, S. V. Pressure-induced switching in ferroelectrics: Phase-field modeling, electrochemistry, flexoelectric effect, and bulk vacancy dynamics. *Physical Review B* **96**, 184109, doi:10.1103/PhysRevB.96.184109 (2017).

141 Blochl, P. E. Projector augmented-wave method. *Phys Rev B Condens Matter* **50**, 17953-17979, doi:10.1103/physrevb.50.17953 (1994).

142 Chimata, R., Shin, H., Benali, A. & Heinonen, O. Defect energetics of cubic hafnia from quantum Monte Carlo simulations. *Physical Review Materials* **3**, 075005, doi:10.1103/PhysRevMaterials.3.075005 (2019).

143 Perdew, J. P., Burke, K. & Ernzerhof, M. Generalized gradient approximation made simple. *Phys. Rev. Lett.* **77**, 3865-3868, doi: 10.1103/PhysRevLett.77.3865 (1996).

144 Ouyang, R., Curtarolo, S., Ahmetcik, E., Scheffler, M. & Ghiringhelli, L. M. SISSO: a compressed-sensing method for identifying the best low-dimensional descriptor in an immensity of offered candidates. *Physical Review Materials* **2**, 083802, doi:10.1103/PhysRevMaterials.2.083802 (2018).

145 JC, F. J. L. Sure independence screening for ultrahigh dimensional feature space. *J. R. Statist. Soc. B* **70**, 849-911, doi: https://doi.org/10.1111/j.1467-9868.2008.00674.x (2008).

146 Fan JQ *et al*. Ultrahigh dimensional feature selection: beyond the linear model. *J Mach Learn Res* **10**, 2013–2038, doi:https://dl.acm.org/doi/10.5555/1577069.1755853 (2009).

147 Ganesh, P. *et al.* Doping a bad metal: origin of suppression of metal-insulator transition in non-stoichiometric VO_2. *Physical Review B* **101**, 155129, doi:10.1103/PhysRevB.101.155129 (2020).

148 Lee, S. *et al.* Anomalously low electronic thermal conductivity in metallic vanadium dioxide. *Science* **355**, 371-374, doi:10.1126/science.aag0410 (2017).

149 Nandi, S. K., Liu, X., Venkatachalam, D. K. & Elliman, R. G. Effect of electrode roughness on electroforming in HfO_2 and defect-induced moderation of electric-field enhancement. *Phys. Rev. Appl.* **4**, 064010, doi:10.1103/PhysRevApplied.4.064010 (2015).

150 Yong, Z. *et al.* Tuning oxygen vacancies and resistive switching properties in ultra-thin HfO_2 RRAM via TiN bottom electrode and interface engineering. *Appl. Surf. Sci.* **551**, doi:10.1016/j.apsusc.2021.149386 (2021).

151 Koroleva, A. A. *et al.* Impact of the atomic layer-deposited Ru electrode surface morphology on resistive switching properties of TaO_x-based memory structures. *ACS Appl. Mater. Interfaces* **12**, 55331-55341, doi:10.1021/acsami.0c14810 (2020).

152 Mao, H. *et al.* Control of resistive switching voltage by nanoparticle-decorated wrinkle interface. *Adv. Electron. Mater.* **5**, 1800503, doi:10.1002/aelm.201800503 (2018).

153 Zhang, F. *et al.* Effect of defect content on the unipolar resistive switching characteristics of ZnO thin film memory devices. *Solid State Commun.* **152**, 1630-1634, doi:10.1016/j.ssc.2012.04.073 (2012).

154 Lanza, M. *et al.* Grain boundaries as preferential sites for resistive switching in the HfO2 resistive random access memory structures. *Appl. Phys. Lett.* **100**, doi:10.1063/1.3697648 (2012).

155 Bersuker, G. *et al.* Grain boundary-driven leakage path formation in HfO_2 dielectrics. *Solid-State Electron.* **65-66**, 146-150, doi:10.1016/j.sse.2011.06.031 (2011).

156 You, B. K. *et al.* Reliable Control of Filament Formation in Resistive Memories by Self-Assembled Nanoinsulators Derived from a Block Copolymer. *ACS Nano* **8**, 9492-9502, doi:https://doi.org/10.1021/nn503713f (2014).

157 Ambrogio, S. *et al.* Statistical Fluctuations in HfO Resistive-Switching Memory: Part I - Set/Reset Variability. *IEEE Trans, Electron Devices* **61**, 2912-2919, doi:10.1109/ted.2014.2330200 (2014).

158 Yu, S. *et al.* A low energy oxide-based electronic synaptic device for neuromorphic visual systems with tolerance to device variation. *Adv. Mater.* **25**, 1774-1779, doi:10.1002/adma.201203680 (2013).

159 Kim, G. S. *et al.* Defect-Engineered Electroforming-Free Analog HfOx Memristor and Its Application to the Neural Network. *ACS Appl. Mater. Interfaces* **11**, 47063-47072, doi:10.1021/acsami.9b16499 (2019).

160 Kondo, T. *et al.* A Nonvolatile Organic Memory Device Using ITO Surfaces Modified by Ag-Nanodots. *Adv. Funct. Mater.* **18**, 1112-1118, doi:10.1002/adfm.200700567 (2008).

161 Shin, M. *et al.* Modulation of Growth Kinetics of Vacuum-Deposited CsPbBr3 Films for Efficient Light-Emitting Diodes. *ACS Appl. Mater. Interfaces* **12**, 1944-1952, doi:10.1021/acsami.9b20094 (2020).

162 Kim, H. J. *et al.* Fabrication of a Cu-Cone-Shaped Cation Source Inserted Conductive Bridge Random Access Memory and Its Improved Switching Reliability. *Adv. Funct. Mater.* **29**, 1806278, doi:10.1002/adfm.201806278 (2019).

163 Chen, Q. *et al.* Controlled Construction of Atomic Point Contact with 16 Quantized Conductance States in Oxide Resistive Switching Memory. *Appl. Electron. Mater.* **1**, 789-798, doi:10.1021/acsaelm.9b00191 (2019).

164 Yoon, J. H. *et al.* Truly Electroforming-Free and Low-Energy Memristors with Preconditioned Conductive Tunneling Paths. *Adv. Funct. Mater.* **27**, 1702010, doi:10.1002/adfm.201702010 (2017).

165 Liu, Q. *et al.* Resistive switching memory effect of ZrO[sub 2] films with Zr[sup +] implanted. *Appl. Phys. Lett.* **92**, 012117, doi:10.1063/1.2832660 (2008).

166 Yoon, J. H. *et al.* Highly improved uniformity in the resistive switching parameters of TiO2 thin films by inserting Ru nanodots. *Adv. Mater.* **25**, 1987-1992, doi:10.1002/adma.201204572 (2013).

167 Xu, Z. *et al.* Co nanoparticles induced resistive switching and magnetism for the electrochemically deposited polypyrrole composite films. *ACS Appl. Mater. Interfaces* **6**, 17823-17830, doi:10.1021/am5044399 (2014).

168 Yoon, J. H. *et al.* Role of Ru nano-dots embedded in TiO2 thin films for improving the resistive switching behavior. *Appl. Phys. Lett.* **97**, 232904, doi:10.1063/1.3525801 (2010).

169 Shin, K.-Y. *et al.* Controllable Formation of Nanofilaments in Resistive Memories via Tip-Enhanced Electric Fields. *Adv. Electron. Mater.* **2**, 1600233, doi:10.1002/aelm.201600233 (2016).

170 Kim, Y. *et al.* Reliable Multistate Data Storage with Low Power Consumption by Selective Oxidation of Pyramid-Structured Resistive Memory. *ACS Appl. Mater. Interfaces* **9**, 38643-38650, doi:10.1021/acsami.7b10188 (2017).

171 Kim, H. D., Yun, M. J., Hong, S. M. & Kim, T. G. Effect of nanopyramid bottom electrodes on bipolar resistive switching phenomena in nickel nitride films-based crossbar arrays. *Nanotechnology* **25**, 125201, doi:10.1088/0957-4484/25/12/125201 (2014).

172 Lee, C., Kim, I., Shin, H., Kim, S. & Cho, J. Nonvolatile memory properties of Pt nanoparticle-embedded TiO(2) nanocomposite multilayers via electrostatic layer-by-layer assembly. *Nanotechnology* **21**, 185704, doi:10.1088/0957-4484/21/18/185704 (2010).

173 Wang, J., Li, L., Huyan, H., Pan, X. & Nonnenmann, S. S. Highly Uniform Resistive Switching in HfO_2 Films Embedded with Ordered Metal Nanoisland Arrays. *Adv. Funct. Mater.* **29**, 1808430, doi:10.1002/adfm.201808430 (2019).

174 Kim, S. *et al.* Physical electro-thermal model of resistive switching in bi-layered resistance-change memory. *Sci Rep-Uk* **3**, 1680, doi:10.1038/Srep01680 (2013).

175 Song, H., Kim, Y. S., Park, J. & Kim, K. M. Designed memristor circuit for self-limited analog switching and its application to a memristive neural network. *Adv. Electron. Mater.* **5**, 1800740, doi:10.1002/aelm.201800740 (2019).

176 Sulzbach, M. C. *et al.* Blocking of Conducting Channels Widens Window for Ferroelectric Resistive Switching in Interface-Engineered $Hf_{0.5}Zr_{0.5}O_2$Tunnel Devices. *Adv Funct Mater* **30**, doi:10.1002/adfm.202002638 (2020).

177 McKenna, K. & Shluger, A. The interaction of oxygen vacancies with grain boundaries in monoclinic HfO2. *Applied Physics Letters* **95**, doi:10.1063/1.3271184 (2009).

178 McKenna, K. *et al.* Grain boundary mediated leakage current in polycrystalline HfO2 films. *Microelectronic Engineering* **88**, 1272-1275, doi:10.1016/j.mee.2011.03.024 (2011).

179 Lanza, M. *et al.* Resistive switching in hafnium dioxide layers: Local phenomenon at grain boundaries. *Applied Physics Letters* **101**, doi:10.1063/1.4765342 (2012).

180 Zhang, K. *et al.* High-throughput phase-field simulations and machine learning of resistive switching in resistive random-access memory. *npj Computational Materials* **6**, 198, doi:10.1038/s41524-020-00455-8 (2020).

181 E. Abbaspour, S. Menzel & Jungemann, C. KMC simulation of the electroforming, set and reset processes in redox-based resistive switching devices. *2016 International Conference on Simulation of Semiconductor Processes and Devices (SISPAD)*, 141-144, doi:10.1109/SISPAD.2016.7605167 (2016).

182 McPherson, J., Kim, J., Shanware, A. & Mogul, H. Thermochemical description of dielectric breakdown in high dielectric constant materials. *Applied Physics Letters* **82**, 2121-2123, doi:10.1063/1.1565180 (2003).

BIOGRAPHICAL INFORMATION

Kena Zhang received her B.E and M.E. in Materials Science and Engineering from Fuzhou University and Northwestern Polytechnical University in China in 2015 and 2018, respectively. She was enrolled in the Ph.D. program in the Department of Materials Science and Engineering at University of Texas at Arlington in 2018. Kena Zhang's research mainly focuses on mesoscale phase-field simulations on the ionic/electronic transport dynamics and resistive switching in dielectric oxide, domain structure in ferroelectric oxide thin films.

LIST OF PUBLICATIONS DURING PH.D.

1. **K. Zhang**, J.J. Wang, Y.H. Huang, L.Q. Chen, P. Ganesh, Y. Cao, "High-throughput phase-field simulations and machine learning of resistive switching in resistive random-access memory", ***npj Computational Materials*** **6**, 198, (2020), doi.org/10.1038/s41524-020-00455-8.

2. **K. Zhang**, Y. Ren, P. Ganesh, Y. Cao, "Effect of electrode and oxide properties on the filament kinetics during electroforming in metal-oxide-based memories", ***npj Computational Materials*** **8**, 76, (2022), doi.org/10.1038/s41524-022-00770-2.

3. **K. Zhang**, Y. Ren, Y. Cao, "Mechanically tunable elastic modulus of freestanding $Ba_{1-x}Sr_xTiO_3$ membranes via phase-field simulation", ***Applied Physical Letter***, 121, 152902 (2022), doi.org/10.1063/5.0099772.

4. Y. Ren, **K. Zhang,** Y. Zhou. Y. Cao, "Phase-field simulation and machine learning study of the effects of elastic and plastic properties of electrodes and solid polymer electrolytes on the suppression of Li dendrite growth", ***ACS Applied Materials & Interfaces,*** 14, 30658, (2022), doi.org/10.1021/acsami.2c03000.

Under Review

5. **K. Zhang**, Y. Cao. "Deterministic conductive filament formation and evolution for improved switching uniformity in embedded metal-oxide based memristor - a phase field study," (to be submitted).
6. **K. Zhang,** A. Dhakane, Ye. Cao, P. Ganesh, "Effect of oxygen vacancy defects on the thermal transport of monoclinic HfO_{2-x} by molecular dynamics simulation", (in preparation).